~ Master thesis ~

Application of microwave techniques to antiprotonic helium spectroscopy

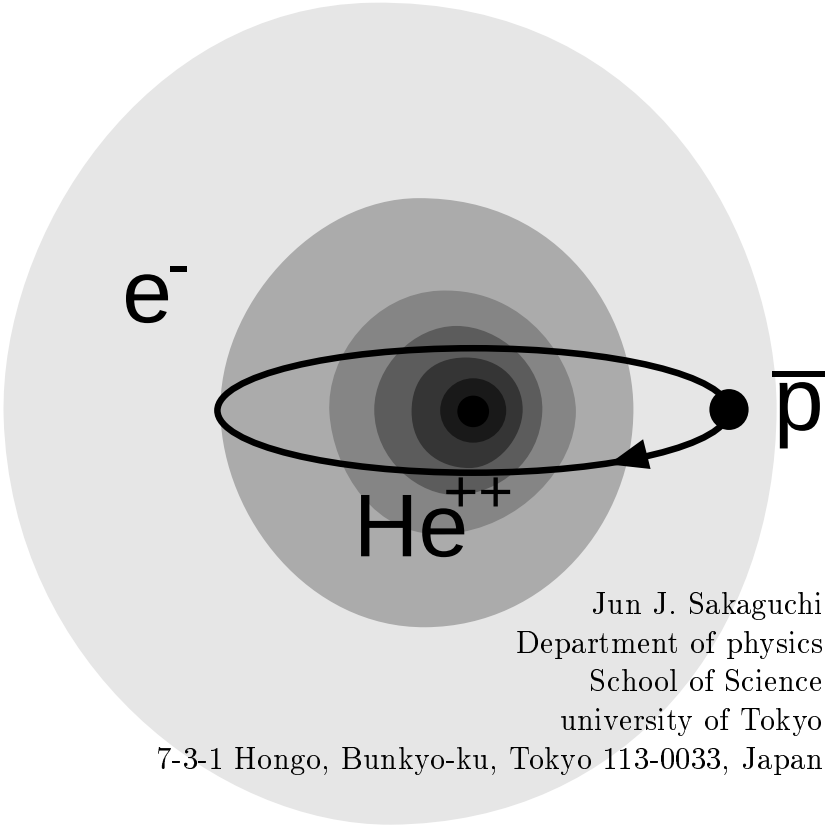

Jun J. Sakaguchi
Department of physics
School of Science
university of Tokyo
7-3-1 Hongo, Bunkyo-ku, Tokyo 113-0033, Japan

January 2000

Abstract

The antiprotonic helium ($\overline{p}$-He^+), a three-body system which consists of one electron, one helium nucleus and the antiproton ($\overline{p}$), is the only known exotic atom which keeps the antiproton as long as a few microseconds. Since the first discovery of this longevity in 1991, many experiments have been performed. Then it turned out that this metastable system provides us an excellent way of studying antiproton properties, which can be a key to the test of CPT invariance.

The antiproton charge and mass were precisely determined by former laser spectroscopy of the $\overline{p}$-He^+, and now we are also interested in the magnetic feature of the antiproton, especially its magnetic moment. By a combinational use of the laser and the microwave, we intend to perform microwave spectroscopy to observe the hyperfine structure (HFS) and superhyperfine structure (SHFS) of the $\overline{p}$-He^+.

This laser-microwave triple resonance experiment is to be performed from 2000 in CERN, using Antiproton Decelerator (AD). The setup of the $\overline{p}$-He^+ spectroscopy experiment was almost successfully developed to produce various powers and frequencies of microwave field at the helium target region. By using a cylindrical microwave cavity and a triple stub tuner, we made a tunable high-Q microwave resonator which can be operated in a cryogenic condition. Microwave detection system was also constructed using I/Q mixers, and we verified that microwave field actually resonated inside the cavity.

For the search of the resonances we must determine the optimum experimental conditions in advance. We simulated the laser-microwave transition process of the $\overline{p}$-He^+, and found that the laser intensity of $2.0 mJ/cm^2$ is best to cause the maximum population asymmetry. The microwave input power should be the maximum power of 3kW when we search the HFS resonance, and when we search the SHFS the estimated optimum microwave power is 1.5W.

Using the numerical and experimental results, the signal-to-noise ratio of the transition signal is estimated. It is concluded that we will need hundred AD shots for each microwave frequency to observe the microwave transition, which indicates the feasibility of our experiment.

Contents

Chapter 1

Introduction

The antiproton was named so because it was expected to have same mass and opposite charge compared to those of proton[*)]. The precedent discovery of positron and success of the Dirac equation were convincing enough for that moment. Yet nobody could ever prove, nor disprove, that it is really antiproton in the sense above. Only recently can we discuss the equality of the properties between them.

In the system of modern physics, there is one fundamental proposition which predicts symmetrical nature of every particle/antiparticle pair. That is the CPT invariance theorem in the quantum field theory. Here C stands for the charge conjugation, P for the space reflection, T for the time reversal, and CPT is a combination of these three transformations. The theorem demands physical laws in all the local field theories with Lorentz invariant Lagrangian to be invariant under CPT transformation. Though invariances for these transformations were once believed, studies on the weak interaction revealed P[2] and CP[3] violations. Thus the CPT invariance also comes to be experimentally tested with high accuracy. The invariance against CPT transformation requires a particle/antiparticle pair to have same values of mass, lifetime, and charge and magnetic moment in opposite signs. Therefore the most straightforward test of CPT invariance is to compare the properties of a particle and its antiparticle, like proton and antiproton (see **Table 1.1**). That is the reason why many scientists pay close attention to the antiproton.

In 1991 our former group[†)] discovered that antiproton survives for an anomalously long period in helium media[4–9] (see **Figure 1.1**). Both theoretical and

[*)] At the moment of its discovery, the only knowledge about $\overline{p}$ property was that it had a negative charge, momenta of $p = 1.19\mathrm{GeV/c}$ and velocities of $0.75 < \beta < 0.78$ [1].

[†)] KEK E215

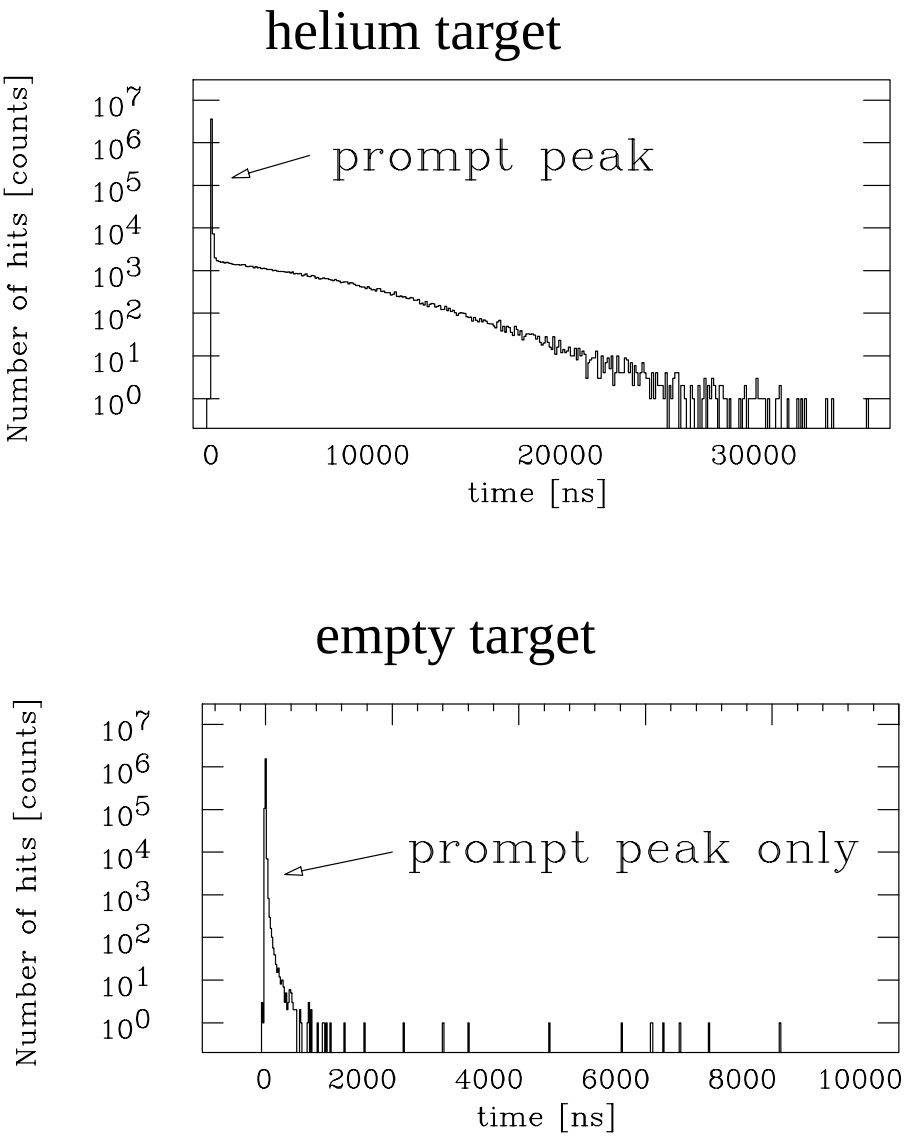

Figure 1.1: Antiproton (delayed) annihilation time spectrum (DATS) for ^{4}He target. (Figures are selectively taken from [22] and not from the first observation.) While 97% of the $\overline{p}$ annihilated almost instantly and formed sharp peak at $t = 0$, there existed long life component which had a lifetime of 4μs. Background is already removed by coincidence logics. Without helium target we cannot observe such delayed annihilation.

experimental efforts were dedicated to this phenomenon and established a notion of $\overline{p}$-He^+ atomcule[‡]. The subsequent laser spectroscopy[10–21] of $\overline{p}$-He^+ successfully revealed its structure and became a powerful tool to determine the antiproton properties, especially antiproton Rydberg constant, $\frac{1}{2}m_{\bar{p}}e^2q_{\bar{p}}^2$ [20]. The resolution of the laser spectroscopy was so good that it resolved[16] a hyperfine structure (HFS) in (n,l)[§] $= (37,35)$ level and also in $(38,34)$. In this case HFS comes from the interaction of the $\overline{p}$ orbital motion with the electron spin magnetic moment, and is supposed to split the initial as well as the final state into two states separated by about 50μeV. The previous laser spectroscopy observed those HFS in an indirect and less informative way. We must make transitions within the hyperfine levels to determine the amount of splitting, which falls into a microwave region. This is what we aim to do in a next generation experiment[23, 24]. The determination of HFS leads us to further understanding of the orbital magnetic moment of antiproton in the framework of three-body system. Also an observation of a finer structure called superhyperfine structure (SHFS) is in scope of the study. Possibly we could determine the magnetic moment of antiproton more precisely than the best known accuracy of 10^{-3} (see **Table 1.1**).

In order to carry out the microwave measurement we have developed a laser and microwave apparatus for experiment at CERN[¶]. Former experiments were performed at LEAR, Low Energy Antiproton Ring, until 1996. For the next phase experiments a new facility AD[25], Antiproton Decelerator, is constructed and provides us 5MeV energy pulsed $\overline{p}$ beams. One purpose of this report is to describe the detail of this experiment, especially in terms of microwave. The setup of the experimental devices and result of test measurement will be found in **Chapter 3**. Another purpose is to give a quantitative understanding of the physical processes involved and provide with a guideline to the real experiment. In **Chapter 4** calculations and computer simulations are performed to determine the optimum conditions of the laser and microwave operation.

Table 1.1: The present status of proton/antiproton CPT test[20, 26, 27].

charge-mass ratio	$(\lvert\frac{q_{\overline{p}}}{m_{\overline{p}}}\rvert - \frac{q_p}{m_p})/\frac{q}{m}_{\text{Average}}$	$(-9 \pm 9) \times 10^{-11}$
charge	$\lvert q_p + q_{\overline{p}}\rvert/e$	$< 5 \times 10^{-7}$
mass	$\lvert m_p + m_{\overline{p}}\rvert/m_p$	$< 5 \times 10^{-7}$
magnetic moment	$(\mu_p + \mu_{\overline{p}})/\lvert\mu_{\text{Average}}\rvert$	$(-2.6 \pm 2.9) \times 10^{-3}$

[‡] To describe this system a word "atomcule" was thought out from atom and molecule, in view of its molecular-like aspect. In fact the first (and some follow-on) substantial calculation of its energy levels[37] was based on molecular picture.

[§] Here n denotes principal quantum number of the $\overline{p}$ and l is orbital angular momentum number.

[¶] CERN:European Laboratory for Particle Physics, Geneva, Switzerland.

Chapter 2

Principle of the microwave spectroscopy experiment

2.1 Formation of the metastable antiprotonic helium

Though CPT symmetry (and experimental proton lifetime*)) predicts quite long lifetime of an antiproton, usually it cannot survive long when it stops in matter. The process of its annihilation is understood as follows: An antiproton, alike other charged particles, ionizes the molecules along its path losing its energy, as long as the energy is large enough to remove the electrons from the molecules. After being decelerated below the ionization energy of the target atom, it will be caught by and bound to Coulomb potential of the atom, replacing one of the bound electrons, probably the peripheral one. This is common for all negatively charged heavy particles. Due to the heavy mass, the Bohr radius for the $\overline{p}$ is almost $\frac{m_{\overline{p}}}{m_e} \approx 1800$ times smaller compared to the electron Bohr radius. Then it has $\sqrt{1800} \approx 40$ times larger principal number n†) than the replaced electron which was located at the same distance from the nucleus. It has a wider range for the angular momentum l‡). When it is caught in a low l state as s or p, the overlap with the nucleus gets large and

*) It is longer than 5×10^{32} year[28].

†) The number forty comes from square root of the ratio of the reduced masses for antiproton and electron. For ^{4}He nucleus n is 38 and for ^{3}He nucleus n is 37.

‡) Strictly speaking, the system should be treated as a compound of a $\overline{p}$ and an electron, and l is not the angular momentum of the $\overline{p}$ alone. For description of the metastability this is not problem-

induces a nuclear absorption. It is immediately absorbed by the nucleus through strong interactions, and together with one of the nucleons it gets converted into some mesons, typically $3 \sim 5$ pions. A $\overline{p}$ with large l, which is localized away from the nucleus, follows some extra steps before absorption. It kicks the other remaining electrons out of the atom, through internal Auger transitions. After the last electron leaves, the rest forms a two-body Coulomb interaction system, and states with different l but same n become degenerate. In absence of level gaps l will be frequently perturbed by thermal collisions with surrounding molecules. This process is known as Stark mixing[§)]. It loses its angular momentum and then gets absorbed by the nucleus as mentioned above. Though the Stark mixing rate depends on the target density, generally it takes at most picoseconds to annihilate. That is a too short period for our laser system which has nanosecond timescale.

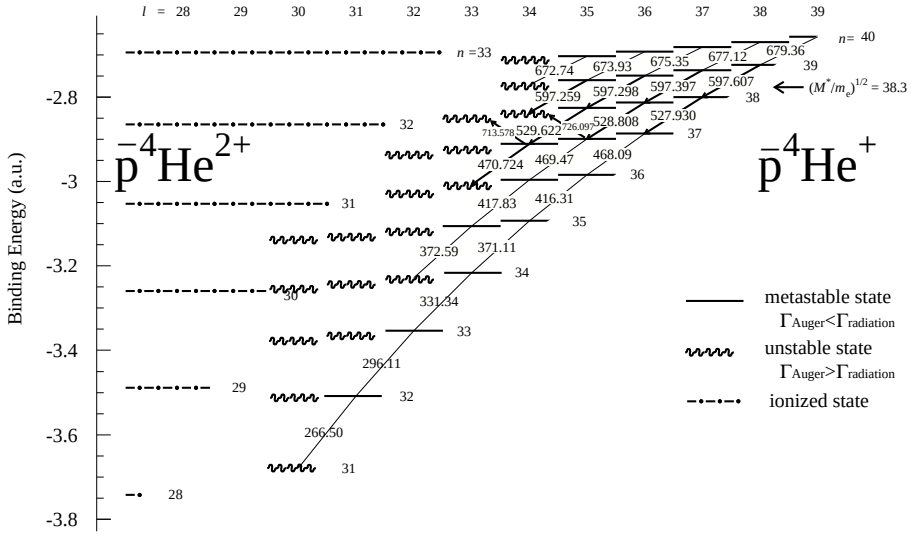

Figure 2.1: The level diagram of $\overline{p}$-He^+ and $\overline{p}$-He^{2+}. The transition energies are shown in wavelength (nm), with six digits for observed ones and five digits for calculated ones. The binding energy (in atomic unit) is not the energy of the $\overline{p}$ only but includes the electron energy for $\overline{p}$-He^+ levels. The states drawn by wavy lines have lower $\overline{p}$-He^{2+} states within $\Delta l \leq 3$, so they have large Auger transition rates and are short-lived.

atic because most fraction of the electron remains in $1s$ orbital and has no angular momentum. The difference is only perturbational. In calculation of electric transition dipole moments, however, a compensational electron movement associated with an "atomic core polarization" has a significant effect[29, 30].

§)Stark mixing doesn't change n, while there is also a process which reduces n, known as an external Auger transition.

However, in case of helium target, about 3% of the trapped $\overline{p}$ show longer lifetimes of $3 \sim 4\mu$s, depending on the target conditions. A $\overline{p}$ in a state of small vibrational quantum number $v(\equiv n-l-1)$, which is called a "circular state", lives long because the internal Auger transition rate in such a state is quite small, even less than the radiative transition rate. The reason of this prohibition is relatively large ionization potential of $\overline{p}$-He^+. In order to ionize, $\overline{p}$-He^+ has to compensate the electron binding energy with further binding of the $\overline{p}$. In other words, large reduction of n is required. For circular states it inevitably means large l reduction. From the law of internal Auger transition[32], however, transitions with small Δl are preferred. Calculation shows that the rates of $\Delta l > 3$ transition is smaller than the typical radiative transition rates of megahertz order for states $n \sim 38$. Energetically $\Delta n \geq 6$ is required as we find in **Figure 2.1**, then lifetime of $v = 0, 1, 2$ states is dominated by radiative transition and concluded to be metastable. Conventionally the term $\overline{p}$-He^+ refers to these metastable compounds only.

The delayed annihilation of the $\overline{p}$ which was shown in **Figure 1.1** is explained by the following decay process. Because of the small Auger transition rate, $\overline{p}$-He^+ in the metastable state only follows spontaneous radiative transitions. Calculations of the E1 transition moments[29, 30] indicate that what we call the "favoured" transition of $\Delta n = \Delta l = -1$ (or $\Delta v = 0$) has the largest moment and dominates over all the branches. According to this propensity rule, it repeats $\Delta v = 0$ favoured transitions and cascades down to the lower metastable states in the same v series, without annihilation. There is, however, an Auger-dominant state which terminates the cascade series, as $(n, l) = (36, 33)$ (for $v = 2$) or $(38, 34)$ (for $v = 3$) (see **Figure 2.1**), and right after the last radiative transition it annihilates through Auger transition. Thus the delayed annihilation of $\overline{p}$ is invoked by these radiative transitions between adjacent pairs of metastable states and short-lived states, a few microseconds after the $\overline{p}$-He^+ formation.

2.2 Metastable states and laser transition

The longevity of $\overline{p}$-He^+ lifetime was elaborately studied through the early work of group PS205[4–8]. Yet conclusive experimental grounds were essential in order to hold the picture above instead of many other hypotheses. So laser spectroscopy experiments were carried out by the PS205 collaboration to confirm it, from 1993 till the end of LEAR operation[10–21].

The principle of the longevity is, in short, the existence of the metastable circular states, and there are some adjacent pairs of metastable states and short-lived states as mentioned above. If we induce a $\overline{p}$ transition from a populated metastable state to an adjacent short-lived state[¶], whether it is favoured or not, additional $\overline{p}$ annihilations will take place and a sharp spike will appear in the delayed annihilation

[¶] Also some transitions between two metastable states could be observed using the double-resonance method[14] or the hydrogen-assisted inverse resonance method[18].

time spectrum (DATS). This spike serves as a sign of the transition.

For this purpose short laser pulses were applied in the former experiment, and actually the spikes are found as shown in **Figure 2.2**. The amount of the induced spike changes with the wavelength of the laser, and formed a Lorentzian-like resonance curve in accordance with the transition efficiency. **Figure 2.3** illustrates

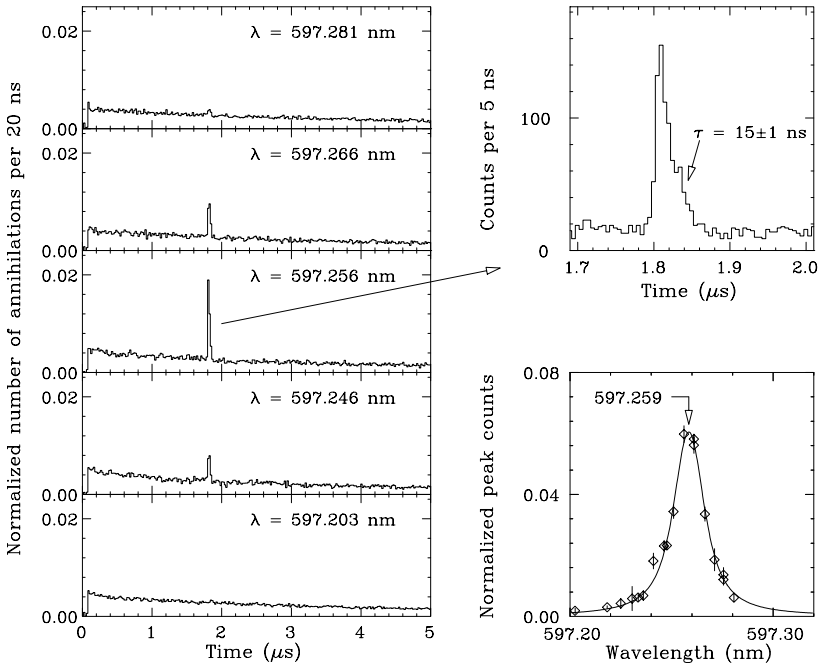

Figure 2.2: The first observation of the laser resonance of the $(n, l) = (39, 35) \rightarrow (38, 34)$ favoured transition, cited from [10]. With irradiation of a laser pulse with $\lambda \sim 597.259$nm, a sharp annihilation spike appears in the DATS. The $\overline{p}$ annihilation plot against the laser wavelength shows a resonance profile.

how we perform the laser spectroscopy. Bunches of $\overline{p}$ get stopped inside the target region filled with the helium gas, and laser beam is irradiated from the other side. Then the induced annihilations are observed by the Cherenkov counters with photomultipliers, and a digital oscilloscope records their output voltage as time spectra. This is the setup for what we call an analog method, and is different from that used in most of the former experiment. The difference of the two methods will be explained in **section 3.2**. The typical time spectrum taken in analog method can be found in **section 3.1**.

So far ten transitions[10–12, 14–16, 18] were identified for ^{4}He target[‖], and the measured transition wavelengths show good agreements with theoretical predic-

[‖] Also three transitions[13] for ^{3}He were discovered.

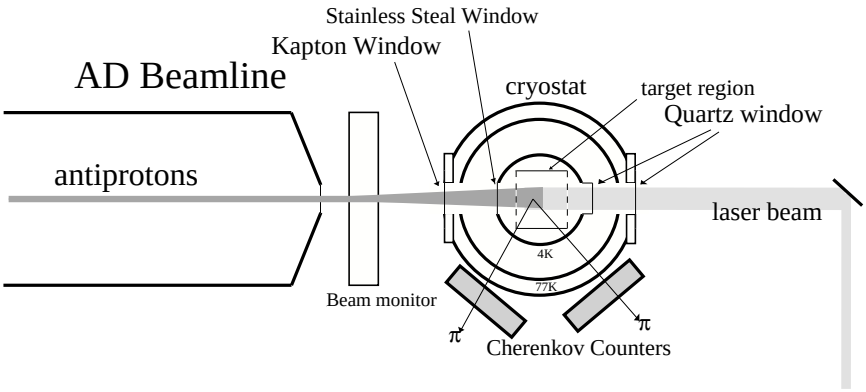

Figure 2.3: Setup of the laser spectroscopy in the analog method.

tions[38, 40–42]. The finest three-body QED calculation[42] of the transition wavelength at the moment includes relativistic correction and Lamb shift and higher order correction, and is claimed to have relative accuracy of 20ppb (or absolute accuracy of 10MHz). The typical precision of the former spectroscopy was several ppm, and for a transition $(n, l) = (39, 35) \rightarrow (38, 34)$ the highest precision of 0.5ppm (or 250MHz) is acquired after density shift correction[20]. With this precision it is concluded that the charge and mass of antiproton agree with those of proton with at least 0.5ppm accuracy[20].

2.3 Hyperfine and superhyperfine structure of the metastable states

The antiprotonic helium is a bound state of the three charged particles interacting through Coulomb forces, together with small magnetic interactions. Theories[38, 40–42] based on the Coulomb interaction successfully calculated the transition energies, but our knowledge of consequences of the magnetic interactions is rather poor.

The largest magnetic effect associated with the antiproton is a hyperfine interaction of the $\overline{p}$ orbital motion $\vec{l}$ and the electron spin magnetic moment $\vec{s_e}$[**)]. When an interaction of a form[††)]

$$\mathcal{H}_1(\vec{l} \cdot \vec{s_e}) \sim \frac{1}{4\pi\epsilon_0} \frac{q_{\overline{p}} \hbar |\mu_e|}{m_{\overline{p}} c^2} \frac{1}{r_{\overline{p}}{}^3} (\vec{l} \cdot \vec{s_e}) \tag{2.1}$$

exists, neither $\vec{l}$ nor $\vec{s_e}$ is conserved in its direction. Then eigenstates are classified by l, s_e, and the combined angular momentum $\vec{F} \equiv \vec{l} + \vec{s_e}$. Because of the hyperfine interaction, states with different F have different energy levels. On a state $F^+ =$

[**)]Note that for a normal atom hyperfine structure comes from the nuclear magnetic moment and the electron spin magnetic moment.

[††)]Stringent form of the magnetic interaction Hamiltonian is found in [36].

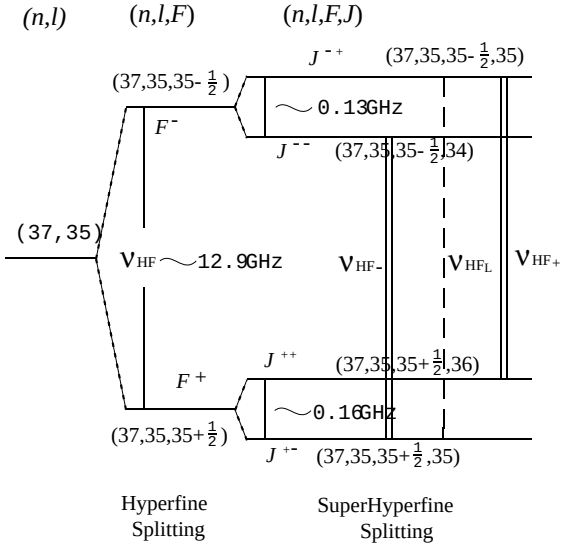

$$\left(\begin{array}{l} \nu_{\mathrm{HF}_+} = 12.8958[\mathrm{GHz}] \\ \nu_{\mathrm{HF}_-} = 12.9239[\mathrm{GHz}] \\ \Delta\nu_{\mathrm{HF}\pm} = \nu_{\mathrm{HF}_-} - \nu_{\mathrm{HF}_+} = 27.967[\mathrm{MHz}] \\ \nu_{\mathrm{HF}_\mathrm{L}} = 13.0569[\mathrm{GHz}] \end{array}\right)$$

Figure 2.4: Upper: The hyperfine and superhyperfine splittings of the $(37, 35)$ level. The values are based on [35]. Lower: the contributions of the each term to the superhyperfine splitting. The third term and the forth term acts in the opposite way and so they almost cancel each other.

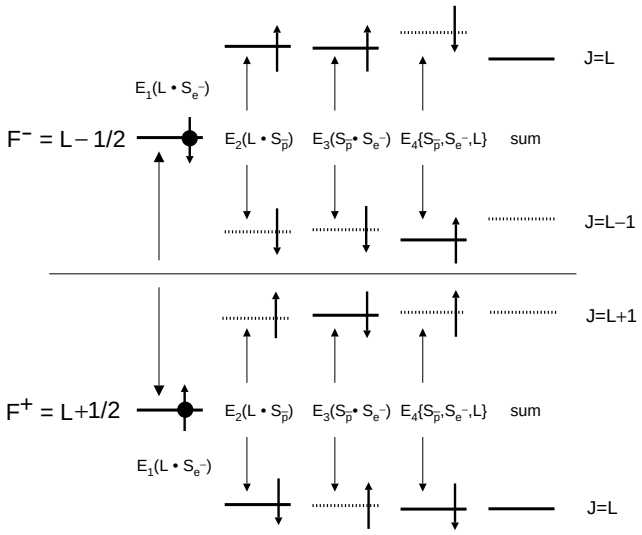

$l + \frac{1}{2}$, the term $\mathcal{H}_1(\vec{l} \cdot \vec{s_{\rm e}})$ acts in a positive way, and vice versa on $F^- = l - \frac{1}{2}$. However, the negative charge of $\overline{p}$ causes negative $\mathcal{H}_1$, so F^+ lies lower than F^-. For some pairs of HFS levels around $n \sim 38$ the amounts of the splittings $\nu_{\rm HF}$ are calculated to be $12 \sim 13$GHz[36].

The other magnetic interactions cause also a superhyperfine structure. The main splitting is introduced by the interaction of the antiproton spin $\vec{s_{\overline{p}}}$ and $\vec{l}$, which corresponds to fine structure effect in a normal atom.

$$\mathcal{H}_2(\vec{l} \cdot \vec{s_{\overline{p}}}) \sim \frac{1}{4\pi\epsilon_0} \frac{e\hbar}{m_{\overline{p}}c^2} \left| \mu_{\overline{p}} - \frac{q_{\overline{p}}\hbar}{2m_{\overline{p}}} \right| \frac{1}{{r_{\overline{p}}}^3} (\vec{l} \cdot \vec{s_{\overline{p}}}) \tag{2.2}$$

Also $\vec{s_{\overline{p}}}$ interacts with the electron spin $\vec{s_{\rm e}}$. This interaction is split into two different components. One is Fermi's contact interaction which comes from an overlapping region of the two particles and has a form of

$$\mathcal{H}_3(\vec{s_{\overline{p}}} \cdot \vec{s_{\rm e}}) \sim -\frac{1}{4\pi\epsilon_0} \frac{8\pi}{3} \frac{\mu_{\overline{p}}\mu_{\rm e}}{c^2} \delta^{(3)}(\vec{r_{\overline{p}}} - \vec{r_{\rm e}})(\vec{s_{\overline{p}}} \cdot \vec{s_{\rm e}}). \tag{2.3}$$

Another is a long distance interdipole interaction which gives a tensorial term as

$$\mathcal{H}_4\{(\vec{s_{\rm e}} \cdot \vec{s_{\overline{p}}}) - 3(\vec{n} \cdot \vec{s_{\rm e}})(\vec{n} \cdot \vec{s_{\overline{p}}})\} \sim \frac{1}{4\pi\epsilon_0} \frac{\mu_{\overline{p}}\mu_{\rm e}}{c^2} \frac{1}{{r_{\overline{p}}}^3} \{(\vec{s_{\rm e}} \cdot \vec{s_{\overline{p}}}) - 3(\vec{n} \cdot \vec{s_{\rm e}})(\vec{n} \cdot \vec{s_{\overline{p}}})\}, \tag{2.4}$$

where $\vec{n}$ means a unit vector $\frac{\vec{r_{\overline{p}}}}{r_{\overline{p}}}$. Then not $\vec{F}$ but $\vec{J} \equiv \vec{F} + \vec{s_{\overline{p}}}$ is the conserved angular momentum, and eigenstates are classified by quantum numbers l, F, J, and J_z (or any component of the vector J). The total perturbation energy[39] is written as

$$E_1(\vec{l} \cdot \vec{s_{\rm e}}) + E_2(\vec{l} \cdot \vec{s_{\overline{p}}}) + E_3(\vec{s_{\overline{p}}} \cdot \vec{s_{\rm e}}) + E_4\{2l(l+1)(\vec{s_{\rm e}} \cdot \vec{s_{\overline{p}}}) - 6(\vec{l} \cdot \vec{s_{\rm e}})(\vec{l} \cdot \vec{s_{\overline{p}}})\}. \tag{2.5}$$

As mentioned above, the large hyperfine splitting $\nu_{\rm HF}$ between F^- and F^+ is caused by the first term. The third term and the forth term act in opposite way, so the superhyperfine splitting is mainly determined by the second term which is positive when $\vec{l}$ and $\vec{s_{\overline{p}}}$ are in the same direction. Therefore the SHFS levels of $J = F - \frac{1}{2}$ are slightly lower than $J = F + \frac{1}{2}$. Actual knowledge of $\nu_{\rm HF}$ gives us insights on the orbital g-factor of antiproton, or QED treatment of antiproton in a three-body system. The superhyperfine splitting is related to the antiproton magnetic moment and we can measure it by the observation of SHFS. Thus we intend to resolve them by microwave spectroscopy.

2.4 Laser transition and microwave transition

This section is devoted to an illustration of the transition mechanism with a practical example of metastable states $(n, l) = (37, 35)$ and short-lived states $(38, 34)$. The former (as well as latter) consist of many states, and due to the hyperfine interaction they are grouped into two sublevels, F^+ (where $(n, l, F) = (37, 35, 35+\frac{1}{2})$) and F^- $((37, 35, 35-\frac{1}{2}))$ (see **Figure 2.4** and **Figure 2.6**). The calculated energy splitting between F^+ and F^- is 12.906GHz and that between F'^+ $((38, 34, 34+\frac{1}{2}))$ and F'^- $((38, 34, 34-\frac{1}{2}))$ is 11.138GHz. Thus 1.767GHz difference occurs between the laser resonance frequency f^+ for the $(F^+ \to F'^+)$ transition and f^- for the $(F^- \to F'^-)$ transition[‡‡]. This difference is large, and we already resolved in our former laser spectroscopy (see **Figure 2.5**). This is the reason why we chose these levels.

In addition to the level shift by the hyperfine interaction, the each group contains a superhyperfine structure. The level F^+ is divided into two, J^{++} (where $(n, l, F, J) = (37, 35, 35+\frac{1}{2}, 36)$) and J^{+-} $((37, 35, 35-\frac{1}{2}, 35))$, and so on for the other. Each of the levels consists of $2J+1$ degenerate[*)] states of different J_z, ranging from $-J$ to J.

Suppose a linearly polarized laser beam incidents on the ensemble of $\overline{p}$-He^+. Here we choose the axis z parallel to the electric field of the laser. The interaction Hamiltonian between $\overline{p}$-He^+ and the laser field is $\hat{\mathcal{H}}_{\rm int}(t) = -\vec{\mu} \cdot \vec{E}(t) = -\mu_z E_z(t)$, where $\vec{\mu} = q_{\overline{p}}\vec{r_{\overline{p}}} - e\vec{r_{\rm e}} + 2e\vec{r}_{\rm He}$ is an electric dipole moment operator. According to the transition dipole moments $\mu_m \equiv \langle n', l', F', J', J'_z \mid \mu_z \mid n, l, F, J, J_z \rangle$, $\overline{p}$-He^+ in some states start transitions to the other states during the laser period.

For a particular initial state, the corresponding principal final state is determined by the laser frequency and selection rules. First of all, J'_z should be equal to J_z from the angular momentum conservation. The electric dipole moment $\vec{\mu}$ is a polar vector operator and has a parity -1, so $\Delta l = \pm 1$ is necessary to conserve the system parities before and after transitions, which are determined by l and l' respectively. Because the electric field does not couple with spin magnetic moment, the particle spins $s_{\rm e}$ and $s_{\overline{p}}$ tend to be conserved. Roughly speaking, $\Delta l \simeq \Delta F \simeq \Delta J$ is most probable in this case. These restrictions are quantitatively argued in **Section 4.2**. In the case of spontaneous emission a propensity rule "$\Delta v = \Delta(n - l - 1) = 0$" exists as mentioned in **section 2.2**, but in the case of excitation n' and l' are determined by the laser frequency. The consequence is that a laser beam with a frequency $f \approx f^+$ transports $\overline{p}$-He^+ in J^{++} to J'^{++} and $\overline{p}$-He^+ in J^{+-} to J'^{+-}, with J_z conserved. Likewise a beam with a frequency $f \approx f^-$ transports J^{-+} to J'^{-+} and J^{--} to J'^{--}.

[‡‡)] A laser transition between F^- and F'^+ is suppressed, because it is mainly attributed to a $\overline{p}$ spin flipping process. A transition between F^+ and F'^- requires $\Delta F = 2$, and is impossible by an E1 transition. Quantitative argument will be given in **Section 4.2**.

[*)] If there exists external static magnetic field, the energy levels become unisotropic (i.e. different energies for different J_z) through Zeeman effect. We assume no static field throughout this thesis. If it is found, we must compensate it with a supplemental solenoid.

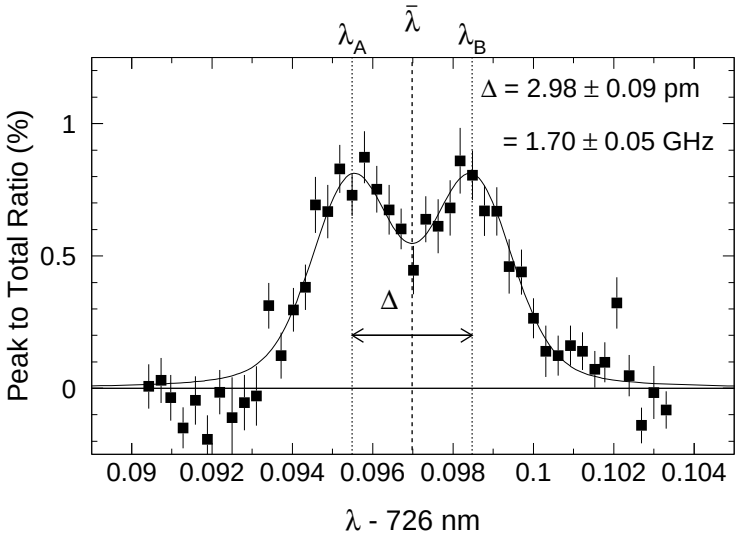

Figure 2.5: Hyperfine splitting resolved by former laser spectroscopy, cited from [16]. The wavelength $\lambda_{\mathrm{A}} = 726.0955$nm corresponds to the $(n, l, F) = (37, 35, 35+\frac{1}{2}) \rightarrow (38, 34, 34+\frac{1}{2})$ transition, and $\lambda_{\mathrm{B}} = 726.0985$nm is for $(37, 35, 35-\frac{1}{2}) \rightarrow (38, 34, 34-\frac{1}{2})$. The difference of the two peak wavelength reflects the different HF splittings of $(37, 35)$ and $(38, 34)$. The bandwidth of the laser we used was 1.2GHz.

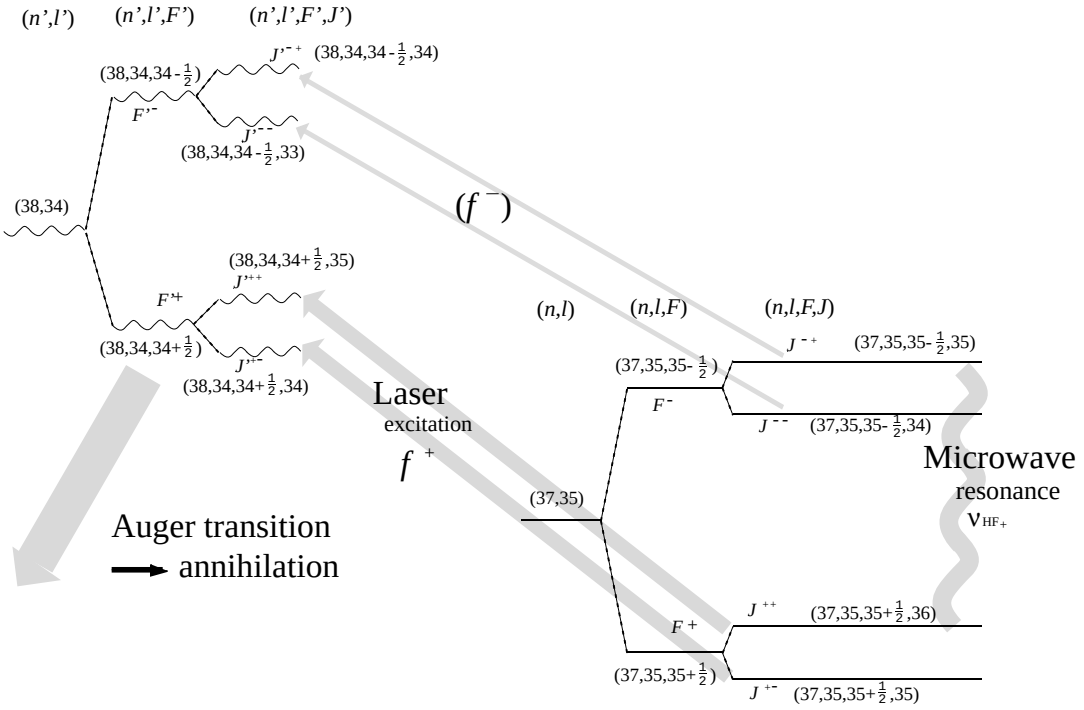

Figure 2.6: Diagram of the $(n, l) = (37, 35)$ and $(38, 34)$ levels, and laser and microwave transitions between the levels.

Then they will annihilate through Auger transitions to $(n, l) = (32, 31)$ and emit pions, and Cherenkov counters detect them (see **Figure 2.3**). As seen in **Figure 2.5**, the frequency splitting $f^+ - f^- = 1.7$GHz is not large enough against laser bandwidth. Thus a laser beam tuned to f^+ also excites $\overline{p}$-He$^+$ in F^- level to some extent, depending on the bandwidth we can achieve.

At the moment of $\overline{p}$-He$^+$ production the number of $\overline{p}$-He$^+$ in all the $J^{\pm\pm}$ states are almost equal. If we irradiate a first laser beam of a frequency f^+, some $\overline{p}$ in J^{++} or J^{+-} level are transfered to states in J'^{++} or J'^{+-} and forced to annihilate. Antiprotons in F^- are less excited because of the different resonance frequency f^-. Thus population inequality or asymmetry arises (see **Figure 4.13**). Application of a second laser pulse will cause smaller annihilation spike compared to the initial one, because the number of $\overline{p}$-He$^+$ in F^+ have been already expended. An important fact is that the amount of the second annihilation serves as a probe of F^+ population at the moment. This is the key to the microwave spectroscopy.

If we are able to make an M1 transition between F^- and F^+ before the second laser, we can feed $\overline{p}$-He$^+$ to the exhausted states and we can expect an increase of second induced annihilation (see **Figure 4.12**, simulated result of these processes). Thus we introduce a microwave magnetic field $H_z(t)$, to de-excite or excite the $\overline{p}$-He$^+$ according to the interaction Hamiltonian $\hat{\mathcal{H}}_{\mathrm{Mint}}(t) = -\overrightarrow{\mu_{\mathrm{M}}} \cdot \vec{H}(t) = -(\mu_{\mathrm{M}})_z H_z(t)$. The electric part of the microwave has no significance in this M1 transition process and so it is ignored here. Here $\overrightarrow{\mu_{\mathrm{M}}}$ means a magnetic dipole moment operator. In this case we can assume $\overrightarrow{\mu_{\mathrm{M}}} \simeq g_{(\mathrm{e})\mathrm{s}} \mu_{\mathrm{B}} \vec{s}_{\mathrm{e}}$[†)] due to the large magnetic moment of the electron. Then transitions are induced as to conserve l and $\vec{s}_{\overline{p}}$, and invert $\vec{s}_{\mathrm{e}}$. This is roughly equivalent to $\Delta l = 0$, $\Delta F = \Delta J = \pm 1$, though $\Delta J = 0$ transitions are also allowed with smaller amplitudes. Needless to mention that J_z is conserved. There will be three types of microwave transitions, $\tau_{+\ (J^{-+} \leftrightarrow J^{++})}$, $\tau_{-\ (J^{--} \leftrightarrow J^{+-})}$ and $\tau_{L\ (J^{-+} \leftrightarrow J^{+-})}$ around 13GHz (see **Figure 2.4**). If the microwave frequency ω_{M} is close to ω_{HF_+} for example, populations of the J^{-+} and J^{++} will be mixed to become equal, and the signal of the second laser-induced annihilation will increase. Then we are able to find the resonance. The second annihilation spectrum against ω_{M} (as **Figure 4.17**) may form peaks at ω_{HF_+}, ω_{HF_-}, and also ω_{HF_L} if we manage to make the microwave field strong enough.

[†)] $g_{(\mathrm{e})\mathrm{s}}$: spin g-factor of electron, 2.002319304386(20)[28].

Chapter 3

Experimental setup

3.1 Overview

The experiment is to be performed with AD in CERN, unique source of slow antiprotons in the world. We have constructed our helium target, laser hut and counting room inside the AD hall (see **Figure 3.2**). A bunch of 1.2×10^7 slow $\overline{p}$ comes from AD in every 70 seconds, and it is degraded to stop inside our microwave cavity. Then about 3% of the $\overline{p}$ form metastable $\overline{p}$-He^+ and decay with lifetimes of about 4 μs. A short laser pulse of around 726.10nm wavelength, which is tuned to the resonance between the metastable state $F^+((n,l,F) = (37,35,35+\frac{1}{2}))$ and unstable state $F'^+((38,34,34+\frac{1}{2}))$, is fired to the target region in response to the trigger signal which comes from the AD control 380μs before the $\overline{p}$ extraction. We chose this transition for its large difference in the two HFS resonance frequencies, f^+ for $F^+ \rightarrow F'^+$ and f^- for $F^- \rightarrow F'^-$. (Here F^- is $((n,l,F) = (37,35,35-\frac{1}{2}))$ and F'^- is $((38,34,34+\frac{1}{2}))$.) The laser depopulates the state F^+ selectively and makes population asymmetry against F^-. With some delay the microwave system begins to send microwave, and resonant microwave field occurs inside the cavity. Then we expect a microwave resonant transition between F^- and F^+. A second laser pulse of the same frequency is fired after that, and forces the $\overline{p}$-He^+ in F^+ to annihilate. The $\overline{p}$-He^+ annihilation is measured as an output of Cherenkov counter, and digital storage oscilloscope records its time spectrum. By scanning the microwave frequency and checking the second laser-induced annihilation we survey the microwave resonance. Each experimental device is controlled remotely by distributed Linux PCs via GPIB or RS232 interfaces, using Labview. A Digital Unix computer integrates them in the framework of Labview and acquires all the measurement data via ethernet.

On the last few days in 1999 AD was actually operated. The beam condition was really bad, nonetheless we managed to re-observe the favoured transition $(n, l) = (39, 35) \rightarrow (38, 34)$ as **Figure 3.1**.

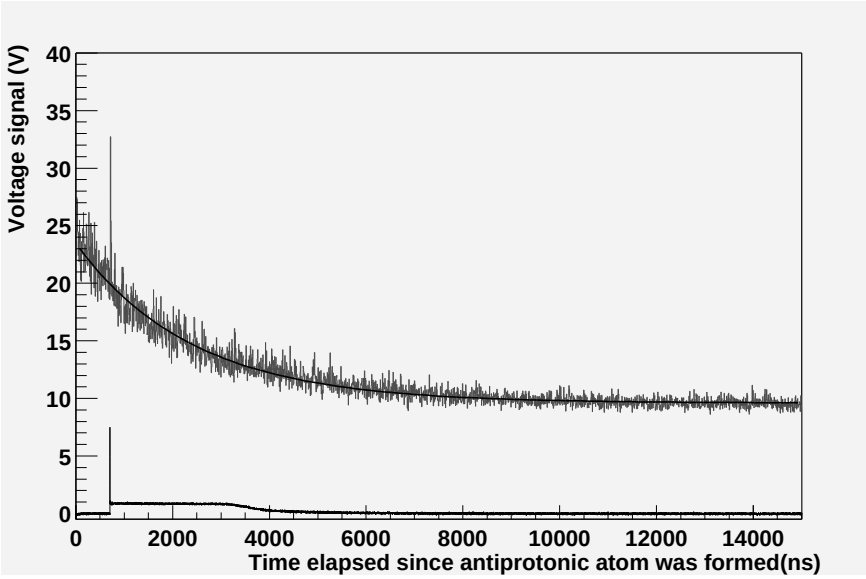

Figure 3.1: The first result of AD, re-observed laser transition of $(n, l) = (39, 35) \rightarrow (38, 34)$. The upper spectrum is a Cherenkov counter output voltage read by the digital oscilloscope, summed over 56 shots of the AD pulse. The solid line is a result of exponential fit. The lower shows output voltage of a *p-i-n* photodiode which was placed near the target to know the laser beam arrival time. The counter signal indicates the long-lived $\overline{p}$-He^+ annihilations (together with the background count from $\pi \rightarrow \mu \rightarrow$e decay of the pions formed by the $\overline{p}$ prompt annihilation), and the laser beams of $\lambda = 597.259$nm induced a sharp annihilation spike.

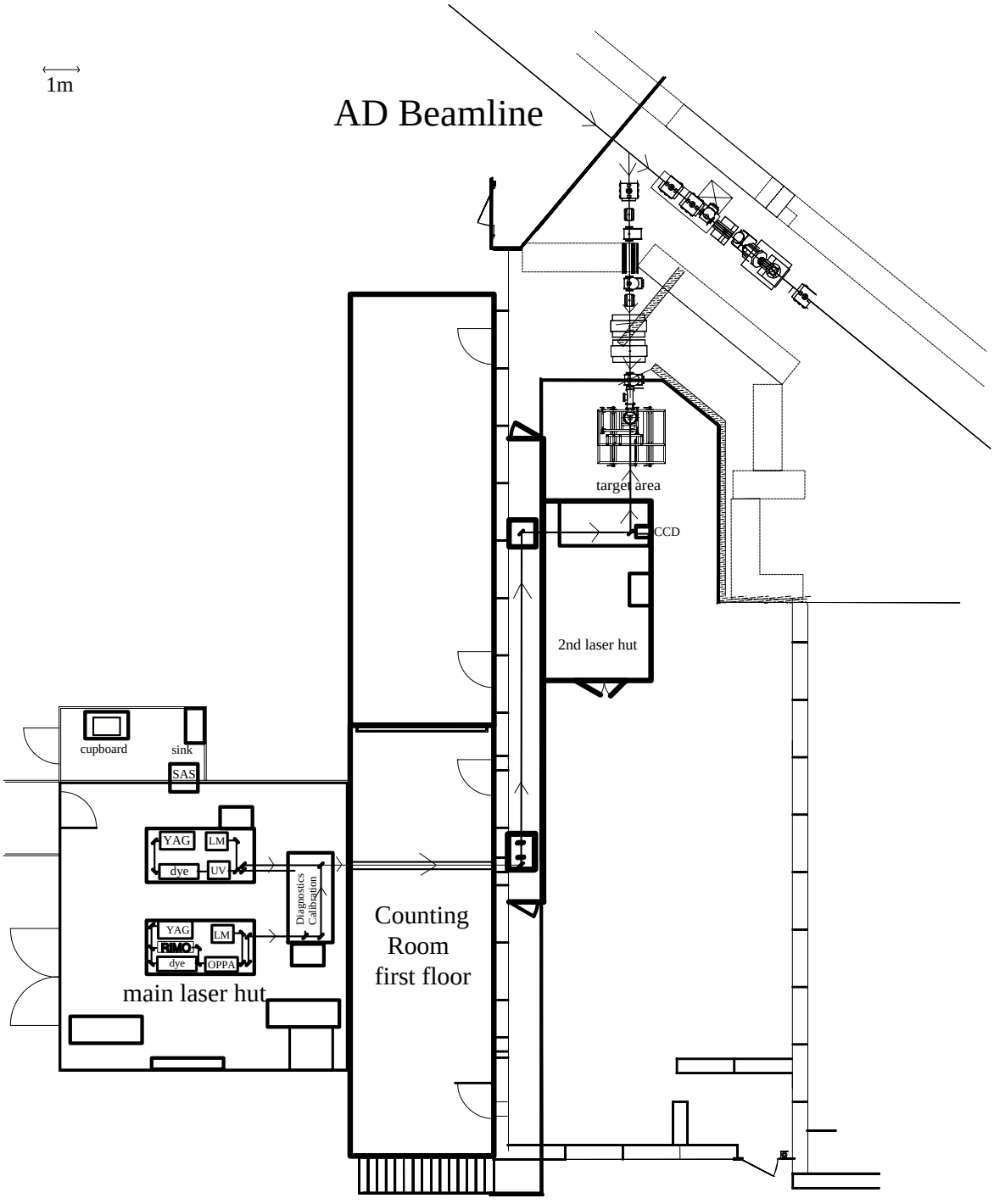

Figure 3.2: Our experimental area in the AD hall.

3.2 AD

The $\overline{p}$ deceleration scheme used in the era of LEAR was a complex one including four accelerators, namely, Proton Synchrotron(PS), Antiproton Collector(AC), Antiproton Accumulator(AA), and LEAR. On the contrary AD is designed[25] to have an integrated function of the former deceleration system, and enables us more economical operations.

The first process is a $\overline{p}$ production. A bunch of 1.5×10^{13} protons is accelerated to 26GeV/c in PS, then extracted and focused onto an iridium target outside. At this proton beam energy, the $\overline{p}$ yield per one proton amounts to 3.5×10^{-6}. The emerging $\overline{p}$ have a restricted momentum distribution around 3.5Gev/c maximum, and collected by magnetic horns they flow into AD as a bunch of 5×10^7 antiprotons together with many background particles as pions.

The next step in AD is a precooling of $\overline{p}$, which was formerly the work of AC. The beam emittance and the momentum dispersion are reduced via stochastic cooling. Then AD decelerates the $\overline{p}$ momentum down to an intermediate momentum of 2.0GeV/c and cools again in order to compensate the adiabatic increase of the emittance and momentum spread. Similarly electron cooling is applied to the beam at 300MeV/c and 100MeV/c during the deceleration cycle. The final product is planned to be a pulse of 1.2×10^7 $\overline{p}$ beam, with 5MeV energy and hundreds nanosecond length, an emittance of 1π mm mrad and 0.1% momentum spread, although in 1999 AD created only 10^5 order $\overline{p}$ of far low quality because of an electron cooling failure.

There is one remarkable change in the experimental strategy, though it is not due to the difference of AD and LEAR. At the beginning of the LEAR experiment the intensity of the $\overline{p}$ beam was only $10^4 s^{-1}$, and it is possible to count each $\overline{p}$ annihilation event one by one. Each $\overline{p}$-He^+ formation was identified, and then laser pulses are fired against it. This method is called a digital counting. While this method was excellent in background elimination, it required enormous number of laser shots and frequent maintenance of the lasers. Another defect of the system was that took time to trigger the laser after $\overline{p}$-He^+ formation, because we could not know when a $\overline{p}$-He^+ emerges beforehand. That is not desirable because we lose more $\overline{p}$-He^+ and get smaller signal as more time we lose. On the other hand, from AD we will get a pulse of 10^7 $\overline{p}$ once in 70 seconds and the peak intensity will amount to $10^{14\sim15} s^{-1}$. Now it is impossible to analyze all the $\overline{p}$ annihilation individually, and all the annihilations are acquired as a time spectrum of the counter output voltage (see **Figure 3.1**). So large background is unavoidable. In this method, however, we can apply laser or microwave to many $\overline{p}$-He^+ at any moment. So this is more efficient than the digital method. This method is called analog method. To acquire accurate results with this method, an intense and stable $\overline{p}$ beam is essential. So the development of AD is the principal factor to the successful experiment.

3.3 Microwave system overview

The helium target region is enclosed by a cylindrical microwave cavity made of stainless steel. With this cavity we aim to produce the microwave magnetic field. The design principle of the microwave system is that it is capable to resonate magnetic field around the $\overline{p}$ stopping region of about one cubic centimeter volume, with a resonance frequency of $\nu_{\mathrm{HF}} = 12.91\mathrm{GHz}$, resonance frequency tunability of about 150MHz, and field strength of $30 \sim 40$gauss which is required for fast microwave transitions (see **section 4.4**). Generally tuning of the resonance frequency can be attained either by mechanical tuning of the cavity dimensions or by the use of stub tuners outside the cavity. However, in our experiment we must keep the cavity at cryogenic condition for many reasons discussed in **Section 3.5**, and mechanical tuning of the cavity will be troublesome. So we use a rigid cavity, and frequency tuning

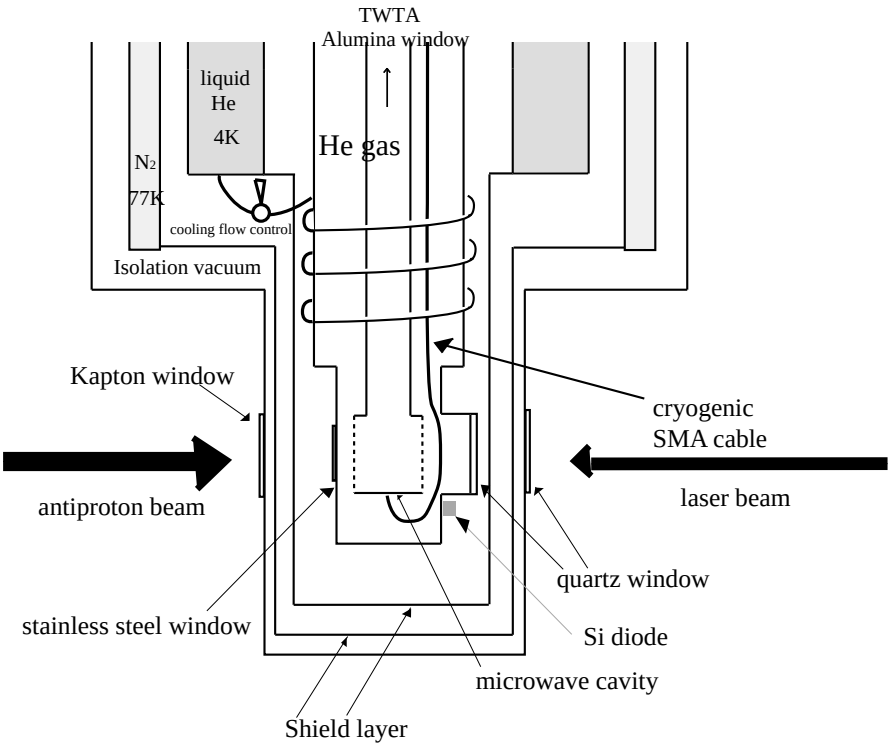

Figure 3.3: The microwave cavity and helium target region inside the cryostat. The target region is cooled by liquid helium flow in the winding tube. The cooling power can be controlled by the control valve. A silicon diode is put inside the cryostat to measure the temperature of the target, thus we can maintain constant temperature as long as liquid helium is reserved.

is attained by a triple stub tuner which is described later. The size of the cavity is

28.3mm in its diameter and 24.6mm in its longitudinal length, and arranged along the $\overline{p}$ beam path and laser path. With these dimensions it has only one resonance mode TM_{110} around $\nu_{TM_{110}} = 12.92$GHz (see **Appendix A.2**). The front face and the back face of the cavity are not walled off completely but are formed of thin mesh*), so that they allow easy entrances of the laser and $\overline{p}$ pulses. The cavity has an iris window which leads to a rectangular microwave waveguide, and through the waveguide we feed max 3kW microwave field into the cavity using a travelling wave tube amplifier (TWTA)†). The unloaded Q value of the cavity is 2700, and with this Q and the microwave power we expect maximum field strength of 70 gauss, which is well over the requirement above (see **section 4.1**). The cavity has also a small probe antenna to pick up the inner field for a diagnosis purpose. The whole cavity, part of the waveguide, and the SMA cable for the pick up signal are put inside the bath-type cryostat as shown in **Figure 3.3**. Because of the stainless steel wall of the cavity, the unloaded Q value does not increase so much at low temperature. The waveguide is also made of stainless steel in order to reduce the heat load, but inner surface of the waveguide is covered by a 10μm copper layer to avoid large losses of the microwave power. The junction to the room temperature and the atmospheric pressure is made of an alumina window which has more than 97% microwave transmittance and stands 10bar pressure without leakage. The cryogenic SMA cable is also made of stainless steel and copper, and leads to the outside via a cryogenic feedthrough.

Another important device is the triple stub tuner (TST). It is a waveguide component with three sidepockets, and the lengths of the every sidepockets are adjustable by stepping motors within a range of $0 \sim 25$mm. Use of the TST and low (loaded) Q cavity provides the most effective way to implement the resonance frequency tunability under the cryogenic condition. ‡) The loaded Q value of the cavity determines the characteristics of the cavity resonance in the framework of the circuit[44], and low $Q_{\rm load}$ means wide width of the cavity resonance. The proper choice of the three pockets imposes extra resonance conditions on the microwave system including the cavity, and makes the system resonance sharper and tunable. Microwave circuit theory[44] accounts for the requirement of three tuners. At least two tuners are indispensable for independent tuning of the resonance frequency and the coupling to the outer system (i.e. impedance of the circuit at the resonance frequency), and the third is to expand the free tuning range. We can make an impedance matching condition, or "critical coupling" and excite the cavity at any frequency within the tuning range of the cavity. The loaded Q value gives the FWHM of the cavity excitation as $\frac{\nu_{\rm cav}}{Q_{\rm load}}$. We can also tune the resonance frequency outside this range, provided that the excited field can be weak. In consequence the frequency tunability requires the cavity $Q_{\rm load}$ of at most 100.

*) The thickness of the mesh is 0.3mm, longer than the skin depth. The width of the mesh wires is 60 μm and the wire-to-wire distance is 0.744mm.

†) Thorn Microwave Device PTC6358

‡) The role of TST is similar to that of an intracavity etalon in a laser system.

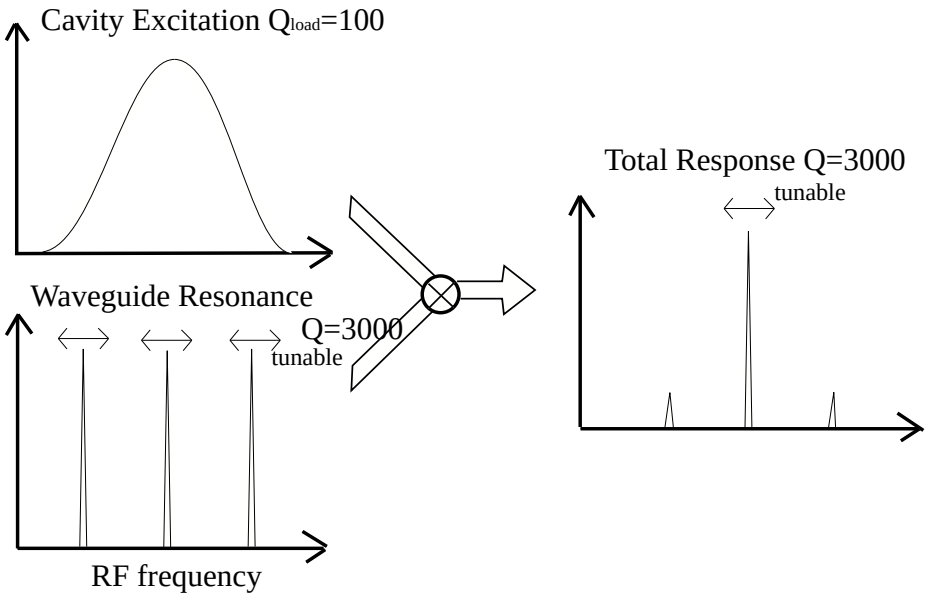

Figure 3.4 illustrates the microwave system overview. Our microwave system is operated in two different modes, changed by remote-controlled waveguide switch[§)]. One is a diagnosis mode in which we measure frequency response of the cavity system, and another is an operation mode which is alloted to the microwave feeding.

Upper part of **Figure 3.5** illustrates the scheme of the diagnosis mode. The vector network analyzer (VNA)[¶)] is a widely used device for a microwave circuit analysis. With that VNA we can measure the reflection coefficient and transmission coefficient of the circuit for the frequency range from 40MHz to 13.5GHz with 1kHz resolution. The each TST tuner position for desired resonance frequency should be defined by a preexperiment, and during the real run the VNA checks the reflection and the pickup signal from the cavity and verifies the resonance status. The result of the test measurement and an example spectrum will be shown in **section 3.6.1**.

As soon as the VNA finishes diagnosis, the system changes into the operation mode and waits for a trigger signal sent from AD control. Lower part of **Figure 3.5** gives the full description of the circuits involved. In this mode the VNA acts as a narrowband microwave source for the TWTA. Continuous microwave comes from the VNA and (after some power adjustment by preamplification and attenuation) goes into the TWTA input. When the arrival of $\overline{p}$, hence the production of $\overline{p}$-He^+, is announced by the AD trigger, the programmable pulse generator[‖)] sends a gate signal to the TWTA, and the TWTA amplifies its input microwave up to 3kW and feeds them into the cavity during the gate signal period. Power of the

[§)] Nihon Koshuha WGSA-1285
[¶)] Anritsu 37225B
[‖)] LeCroy 9210

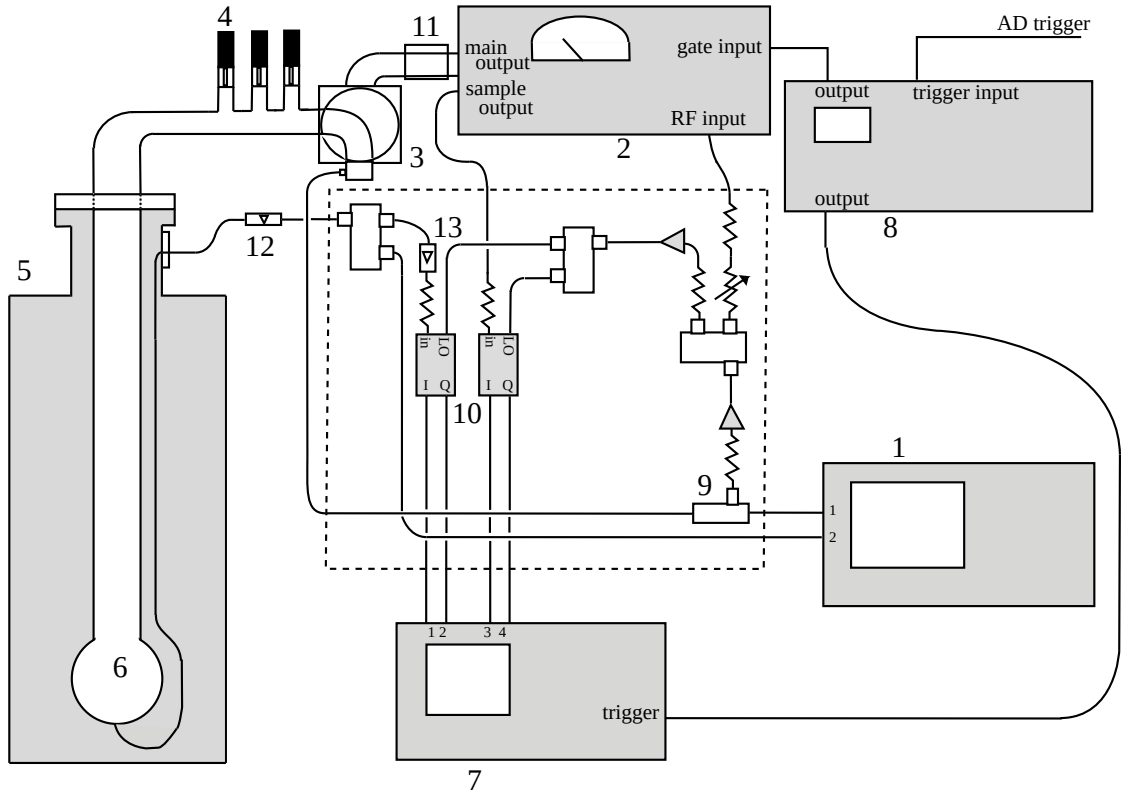

1:Vector Network Analyzer
2:Travelling Wave Tube Amplifier
3:Motorized Waveguide Switch
4:Tripple Stub Tuner
5:Cryostat
6:Microwave Cavity
7:Digital Oscilloscope
8:Pulse Generator
9:Directional Coupler
10:I/Q Mixer
11:Isolator
12:Limiter
13:Isolator

:Attenuator
:Amplifier
:Voltage Controlled Attenuator
:Hybrid

Figure 3.4: The schematic drawing of our microwave circuit.

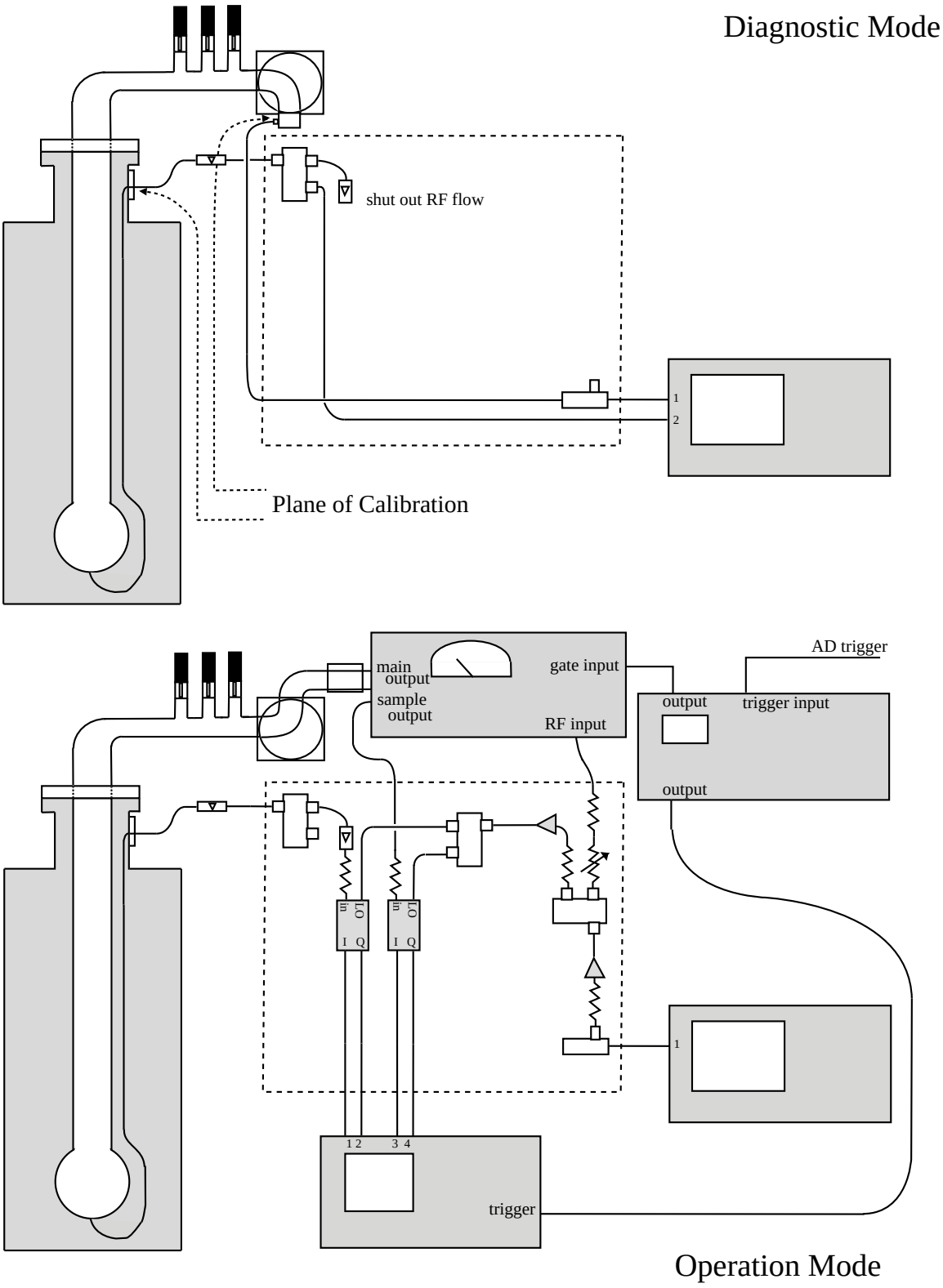

Figure 3.5: Two modes of the operation of our microwave circuit. Some inessential parts are omitted.

output microwave is controllable using a voltage controlled variable attenuator[**)] which diminishes the microwave power exponentially according to a control voltage (see **3.6.2**).

The resultant microwave oscillates with 12.9GHz frequency, and the oscilloscope is not a feasible device to measure such a fast signal. On the other hand the VNA is a rather static device which measures a signal frequency accurately in a long span and not suited for a short signal analysis. In order to see whether the cavity is successfully filled with the microwave or not, we use microwave I/Q mixers[††)]. I/Q mixer is a circuit of nonlinear devices which mixes an RF input signal with a reference RF signal called local oscillator (LO), and outputs DC signals proportional to the in-phase (I) and quadrature (Q) component of the input signal against LO (see **section 3.6.3**). We use two mixers, one for a sample output of the TWTA and one for the pickup signal from the cavity. The LO inputs are supplied by a branch of the VNA output signal. Some attenuations and amplifications are taken for proper power requirements of the devices.

This is the overview of the microwave system, though some components are still left unmentioned. A microwave isolator[‡‡)] is used to make a one-way microwave transmission just after the TWTA output and prevent its breakdown by a reflected wave. It has a forward transmission of 90% and backward transmission of -50dB. Also a microwave limiter[*)] is inserted in the pickup signal transmission line. Its output is limited under 10dBm and it protects the VNA and I/Q mixers from too strong pickup signal in case of misoperation. Finally, one more isolator is put before the pickup I/Q mixer, otherwise the VNA fails to get correct transmission spectrum because of an I/Q mixer noise. Between the main output of the TWTA and the cavity, where high power field travels, a rectangular waveguide is used, while the other block is composed of SMA standard transmission lines[†)] and semi-rigid cables.

3.4 Laser design

We irradiate the metastable atoms formed inside the cavity, with a laser light pulse which comes from the opposite way to the $\overline{p}$ beam path. A Monte Carlo simulation showed that the stopping region of the $\overline{p}$ was 1cm in its diameter for a successfully refined beam, so we have to expand the laser beam to the same size to increase their overlap. It is also predicted from theories and the former experiments that the "unfavoured" transitions like $(n, l) = (37, 35) \rightarrow (38, 34)$, which change vibrational quantum number $v = n - l - 1$, have only one tenth of transition moments than "favoured" transitions in which $\Delta v = 0$ and requires

[**)] G.T.Microwave,Inc. A6L-78N-7
[††)] MITEQ IR0618LC2Q
[‡‡)] RYT industries 401328
[*)] Hewlett Packard 11693A
[†)] SHUNER Sucoflex 104

a hundred times larger laser power. For that reason we need a millijoule order laser energy per 1 cm^2 for every shot. Since our experiments are involved in time spectrum analysis, timing jitter should be as small as nanosecond. Stable temporal and spatial profiles are desirable, less power fluctuation is preferable, and most of all a wavelength of $\lambda = 726$nm with as narrow bandwidth as possible is required.

We chose a commercial dye laser[‡)] as a solution, which is pumped by a Nd:YAG laser[§)]. The YAG laser fires a 300mJ laser pulse of 532nm wavelength triggered by an AD signal which precedes 380μs earlier than $\overline{p}$ extraction. The dye laser output energy can be as large as 10mJ per 3ns pulse, thus the intensity requirement is satisfied. We use Styryl 6 as a laser dye, which has a 13nm scan range around 721nm wavelength. We have two identical but independent sets of the laser system in order to fire two successive laser pulses, one before the microwave transition and the other after that. The wavelengths are measured shot by shot by a commercial interferometer[¶)]. The best achievable resolution is 600 $\sim$ 800MHz. Laser power can be measured by a pyroelectric detector. The power fluctuation is about 10% at random trigger rate of 1shot/minute.

3.5 Cryogenics

It is also essential to keep the target helium gas as cold as about 5K during the spectroscopy for many reasons. First of all we must get rid of impurity gases as hydrogen, oxygen, nitrogen and water. Even a few ppm contaminations of these gases quench $\overline{p}$-He^+ and distort the annihilation spectrum[9, 17]. The next reason is that we should attain high target density so as to stop $\overline{p}$ in as small target region as possible. At our typical operation condition of temperature $T = 5.8$K and pressure $P = 500$mbar the gas density is $\rho = 4.5g/l$. Finally, it is required to repress the helium atom thermal agitations and reduce the Doppler broadening of the laser transition. At a temperature of T the helium atom velocity (and so the $\overline{p}$-He^+ velocity) v distributes according to the Maxwell-Boltzmann distribution

$$f(v_x)dv_x = \left(\frac{M}{2\pi kT}\right)^{\frac{3}{2}} \exp\left\{-\frac{Mv_x^2}{2kT}\right\} dv_x \tag{3.1}$$

where M is the mass of the $\overline{p}$-He^+ and x is the direction of the laser path. Since the Doppler shift of a frequency ν is given by $\Delta\nu = \nu v_x/c$, the observed laser resonance shape subjects to Gaussian type broadening with a full width at half maximum of $\Delta\nu_D = 2\sqrt{2\ln 2}\,\nu\sqrt{\frac{kT}{Mc^2}}$. Even for $T = 5.8$K, it brings 320MHz broadening into the transition wavelength $\lambda = 726$nm. Also density shift[‖)] of the resonance frequency

[‡)] Lambda Physik Scanmate2E

[§)] Coherent Infinity 15-30

[¶)] ATOS Lambdameter LM-007

[‖)] The density shift and broadening, which changes the resonance frequency and its width according to the density, was systematically studied in the former experiments. See [20].

should be regulated as constant.

Therefore all the process should be in a cryogenic condition, and we put the cavity and part of the waveguide inside a cryostat. The schematic drawing was already shown in **Figure 3.3**. The target region including the microwave cavity is cooled by the controlled flow of liquid helium which is reserved in the cryostat. The target temperature is acquired by the silicon diode, and together with a heating coil in the target it enable us to do PID control of the target temperature.

3.6 Results of the test measurements on the microwave system

3.6.1 Measurement of the microwave circuit response

To fill the cavity with microwave field of a desired frequency, we must make a resonance condition with the help of TST. So we investigated the circuit resonance and TST tuning at the experimental condition (i.e. $T \sim 5.8$K, $p = 550 \sim 650$mbar). **Figure 3.6** shows an well-tuned example spectrum of the S parameters of the circuit[**)] against the input RF frequency. S parameter stands for the transmitted

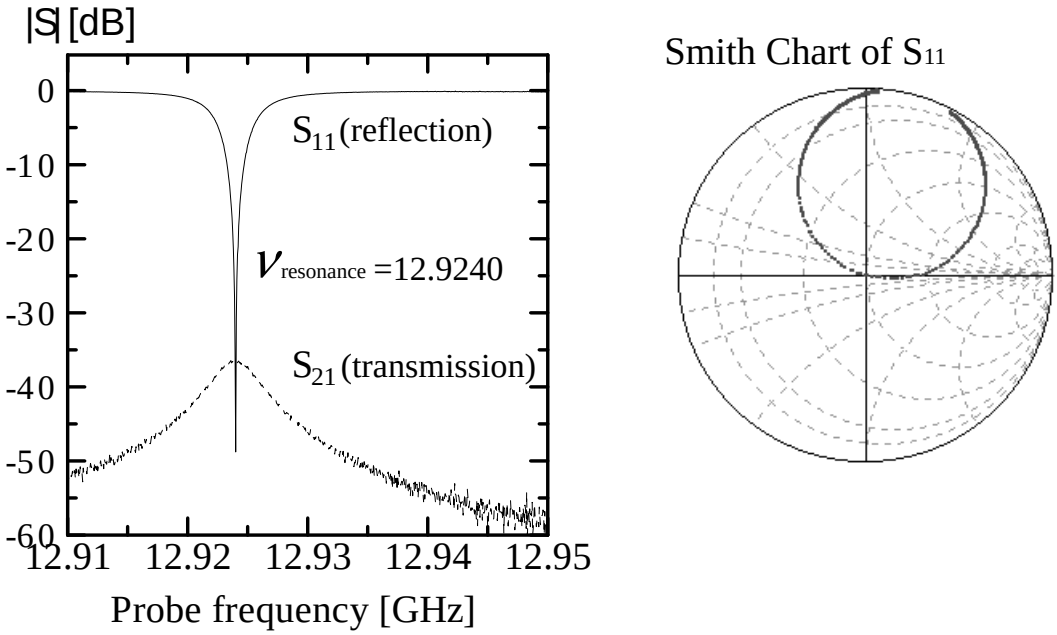

Figure 3.6: Left: The spectrum of the circuit response. We find a sharp ($Q = 3000$) resonance both in the reflection and the transmission. The centre of the resonance is tuned to $\nu_{\mathrm{HF\_}}$. The target temperature was 5.80K and the target pressure was 607mbar. Right: Smith chart display of the S_{11}. The circuit reflection indices are plotted in a complex plane. The circular trajectory indicates that the circuit is well resonant.

("S_{21}") or reflected ("S_{11}") complex field amplitude. The probe microwave travels in the waveguide with little resistive loss, and that of nonresonant frequency is completely reflected from the circuit. On the other hand microwave which satisfies the resonance condition of the circuit will be resonated inside the circuit including the cavity, hence reflection becomes small. The field inside the cavity is probed by

[**)]Here "circuit" means the part between the planes of calibration in **Figure 3.5**.

the pickup antenna and observed as the transmission. From the spectrum and the Smith chart, a reflection index plot in complex plane, we find that the circuit is tuned to form a resonance. We require critical coupling of the circuit (or no reflection) to supply maximum microwave power. The center of the circuit resonance frequency can be tuned at will by changing the TST positions. The loaded Q value of the cavity was measured to be $Q_{\rm load} = 96.5$ at room temperature, so the cavity will be excitable within a range of $\pm\frac{1}{Q_{\rm load}}\nu_{\rm TM_{110}} \pm 130$MHz around the characteristic resonance frequency of $\nu_{\rm TM_{110}} = 12.92$GHz (see **section 3.3**). The HFS transition frequency $\nu_{\rm HF_+}$ and $\nu_{\rm HF\_}$ will be well covered, while $\nu_{\rm HF_L}$ is somewhat out of the resonance.

Figure 3.7 shows the scanning profile of the TST actuator positions. The actuators[††)] can set the position of the tuner terminals with 0.25μm precision. Since we have to control the resonance centre frequency and the coupling, we manipulated two actuators. The third one is fixed to some position. This is only a test measurement and we will make a complete mapping table just before the real experiment in order to be as accurate as possible.

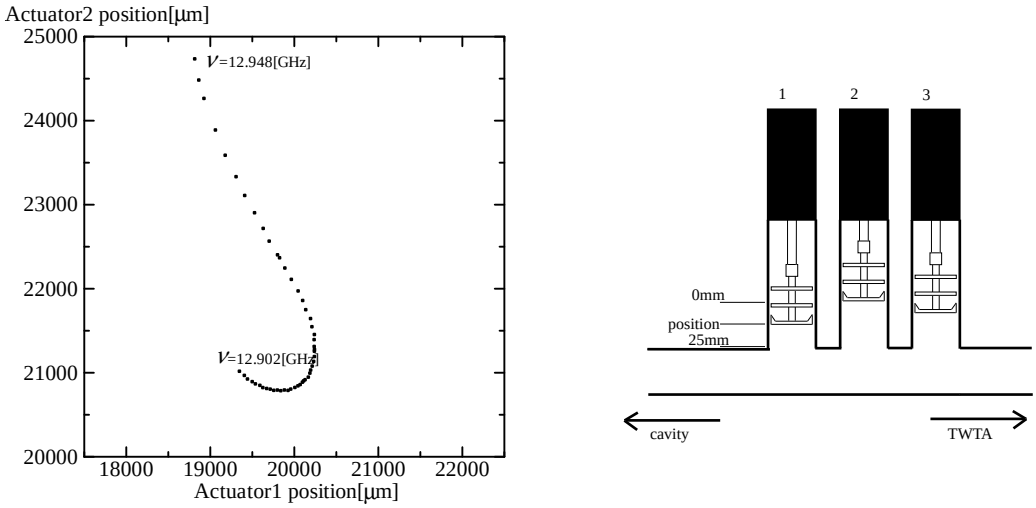

Figure 3.7: Result of the test scan of the TST tuners. Actuator 1 and 2 were adjusted step by step while actuator 3 was fixed to 18.675mm. The scan step was 1MHz. One step took about $5 \sim 10$ minutes. The target temperature was kept within 5.80 ± 0.02K. The pressure decreased in time from 677mbar to 567mbar. During the scan the circuit impedance was tuned to match with the input at each resonance frequency, and the circuit Q values were $2700 \sim 3000$.

††)Sigma Kouki DMY25

3.6.2 Microwave power control by the voltage controlled variable attenuator

Since the TWTA has only a fixed gain of about 75dB, we must control the microwave power by changing the input power level of the TWTA. For this purpose a voltage-controlled variable attenuator is inserted before the input. It has a port which accepts DC voltage from zero to ten volt, and accordingly attenuates the microwave power. The relation between the control voltage and the output power at the port of the TWTA input was measured with the VNA as shown below. Thus

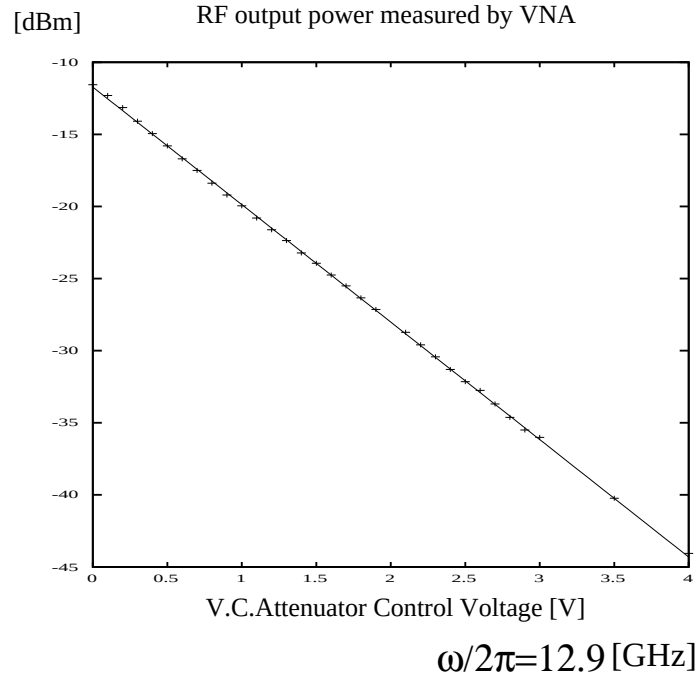

Figure 3.8: The output power at the input port of the TWTA, controlled by the voltage of the variable attenuator. Within this range the TWTA input power is controlled linearly by the attenuator voltage. The fit function is $Y/[\mathrm{dBm}] = -11.72 - 8.14\ X/[\mathrm{V}]$. The input level at no control voltage is adjusted a little bit higher than -15dBm, the saturation level of the TWTA.

the microwave power control is achieved. Although a small shift of the phase was observed[‡‡)], which is not important for our experiment. With voltage higher than five volt the exponentiality of the observed output power became a bit worse. From seven volt the output power level reaches the noise level and cannot be attenuated any more.

[‡‡)]It is shown in the lower-right part of **Figure 3.9**, the I/Q mixer test.

3.6.3 Microwave power survey with I/Q mixers

I/Q mixer is a device which outputs DC voltage signals according to the powers and the relative phase of the input signal and Local Oscillator (LO) signal.

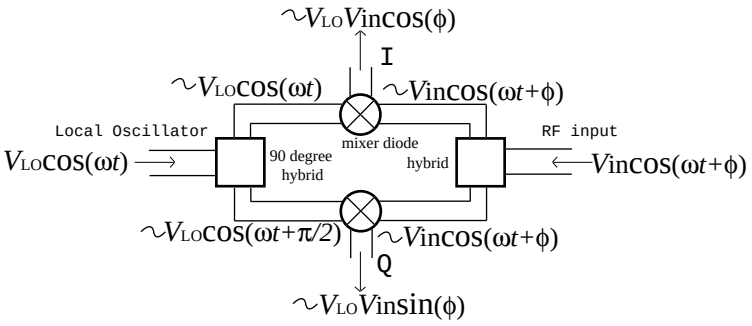

Suppose the input RF signal oscillates with the same frequency ω as that of the LO signal, but with a different phase ϕ.

$$V_{\mathrm{LO}}(t) = V_{\mathrm{LO}}\cos(\omega t)$$
$$V_{\mathrm{in}}(t) = V_{\mathrm{in}}\cos(\omega t+\phi) = V_{\mathrm{in}}(\cos(\phi)\cos(\omega t) - \sin(\phi)\sin(\omega t))$$

Using a nonlinear mixer we can get a multiplied output of the two input voltages, and because $\cos(\omega t)\cos(\omega t+\phi) = \frac{1}{2}(\cos(\phi)+\cos(2\omega t+\phi))$, there appears a DC output which is proportional to $V_{\mathrm{LO}}V_{\mathrm{in}}\cos(\phi)$. Thus we can get the in-phase component of the RF input, as

$$V_{\mathrm{I}} \propto V_{\mathrm{LO}}V_{\mathrm{in}}\cos(\phi). \tag{3.2}$$

Changing the LO phase by 90 degree, we can also get the orthogonal component as

$$V_{\mathrm{Q}} \propto V_{\mathrm{LO}}V_{\mathrm{in}}\sin(\phi). \tag{3.3}$$

The I/Q mixer contains all these functions in one and makes it possible to observe the amplitude and phase of the microwave signal. In the experiment we are not so concerned about the phase information. When the output ports are terminated with impedance Z_{out}, sum of the output power is $P_{\mathrm{out}} = \frac{V_{\mathrm{I}}^2}{Z_{\mathrm{out}}} + \frac{V_{\mathrm{Q}}^2}{Z_{\mathrm{out}}}$. The input RF power of the I/Q mixer is written as $P_{\mathrm{in}} = \frac{V_{\mathrm{LO}}^2}{Z_{\mathrm{in}}}$ when it has the input impedance Z_{in}, and we find a linear relation between the output power and the RF input power.

$$P_{\mathrm{out}} \propto P_{\mathrm{LO}}P_{\mathrm{in}} \tag{3.4}$$

For the LO ports constant powers of $P_{\mathrm{LO}} = 14\mathrm{dBm}$ are supplied from the VNA through amplifiers. Against various input powers made with the variable attenuator the output signals and powers were measured by the digital oscilloscope, and plotted in **Figure 3.9**. As expected, the mixer output powers are proportional to the RF

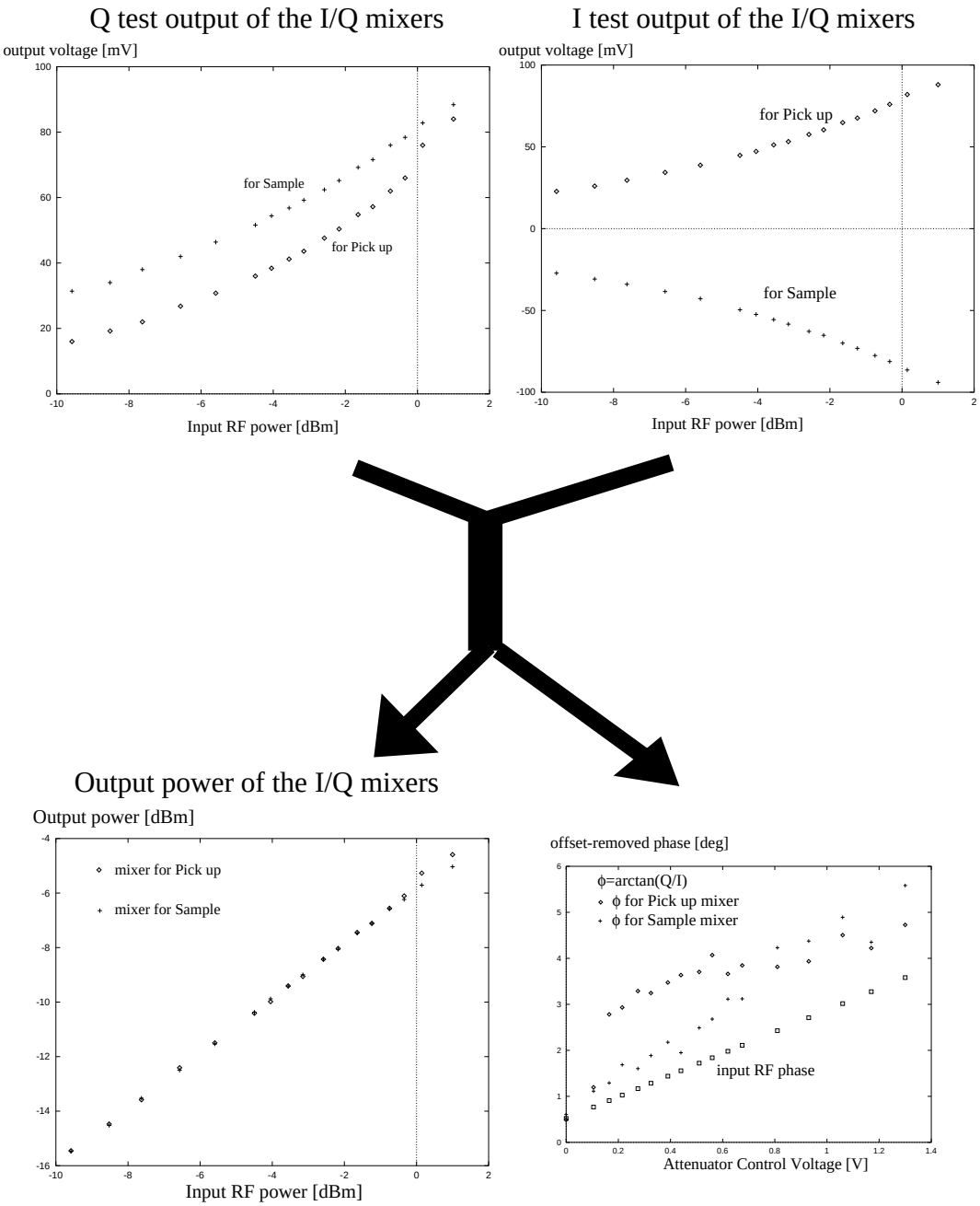

Figure 3.9: Test results of the I/Q mixer power response. The input power tuning was achieved by using the voltage controlled variable attenuator. The I/Q responses were different for the two I/Q mixers, probably because of the different LO phases. The output power was calculated as $\frac{(V_{\mathrm{I}}-V_{\mathrm{Ioffset}})^2+(V_{\mathrm{Q}}-V_{\mathrm{Qoffset}})^2}{50[\Omega]}$, and linearly related to the RF input power. On the other hand the phase data contain large errors.

input power. So we can use them as a means to check the RF power. **Figure 3.10** is an example of the TWTA output observation through the cavity. The TWTA produced a two microsecond pulse of amplified microwave into the cavity. The circuit was tuned to be resonant at a frequency $\nu = 12.8853$GHz with a peak transmission of $S_{21} = -36.3$dB. The observed voltage pulse power of the mixer output was about -8dBm, which means -2dBm RF input power. So the TWTA output power is estimated to be 34dBm*). At the moment the TWTA input power was about -22dBm, thus it means that the amplification gain was 56dB. Because the TWTA went out of order after the observation, we could not perform systematic study of the TWTA amplification.

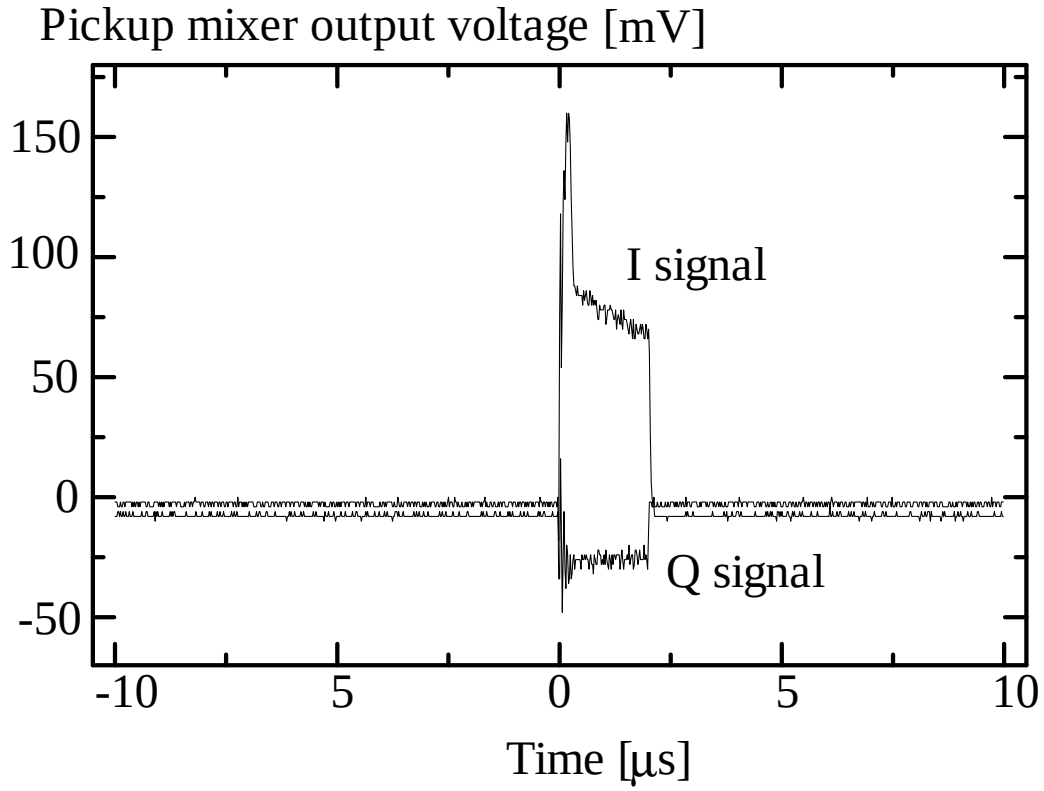

Figure 3.10: The pickup mixer output voltage at the moment of the TWTA amplification, measured by the digital oscilloscope.

*) At that time no attenuator was inserted before the I/Q mixers.

Chapter 4

Simulation of the laser-microwave experiment

4.1 The laser pulse and the microwave

In this section we discuss about the electromagnetic field of our laser and microwave. Let us define coordinates so that the laser beam travels along x axis and is linearly polarized to z axis. The temporal change of laser power at a target position ideally centred is well described by a single component Gauss function,

$$P(x,y,z,t) = P_0(x,y,z)e^{-(\ln 2)\ \frac{t-t_0-x/c}{\delta t/2}\ ^2} \tag{4.1}$$

as shown in the lower part of **Figure 4.2**, while the excimer-pumped dye laser used in the former experiments had two peaks. The full width at half maximum of the laser power δt is about 3ns. The relation between the intensity $I(x,y,z)$ and the peak power P_0 is determined by an integration with respect to t, as

$$I = \sqrt{\frac{\pi}{4\ln 2}} P_0 \delta t = 1.064 P_0 \delta t. \tag{4.2}$$

In our case it is convenient to choose the unit as $I = [\mathrm{mJ/cm^2}]$, $\delta t = [\mathrm{ns}]$ and $P_0 = [\mathrm{MW/cm^2}]$. The maximum laser power is 10mJ. We expand the laser beam so that $I(x,y,z)$ becomes uniform over the $\overline{p}$ stopping region. Then the laser electric field E_z at the target point has a form $E_z = E_0(t)\cos(\omega t)$, independent of the position. Here the amplitude $E_0(t)$ is governed by the laser power profile of nanosecond timescale,

and $\cos(\omega t)$ is an oscillating part of femtosecond timescale, depending on the angular frequency $\omega/2\pi \sim f^+ = 0.4\text{PHz}$. The wavelength of 726nm allows us to ignore spatial variation of the field from the point of the atomcule. The amplitude $E_0(t)$ is dependent on $\sqrt{P(t)}$ and given by

$$E_0(t) = E_0 e^{-\frac{1}{2}\ln 2\left(\frac{t-t_0}{\delta t/2}\right)^2}, \tag{4.3}$$

where

$$E_0 = 2.745 \times 10^6 \sqrt{P_0/[\text{MW/cm}^2]}[\text{NC}^{-1}]. \tag{4.4}$$

According to the gate signal generated by the pulse generator, the TWTA fills the cavity with resonant microwave during the gate period. The maximum output power of the TWTA is specified to 3kW, and unloaded Q factor of the cavity is 2700. Then the resonated microwave energy inside the cavity is given by

$$P_{\text{M}} = QP_{\text{loss}}\frac{1}{\omega}, \tag{4.5}$$

where P_{loss} is the microwave energy loss inside the cavity (or, in this case, energy supply from outside) and ω is the microwave angular frequency (see **Appendix A**). The cavity resonance mode of our interest is TM_{110} mode. The field of the mode at the centre of the cavity is described as $H_z = H_0 \sin(\omega t)$, and H_0 is given by the microwave power P_{M} as

$$H_0 = \sqrt{\frac{P_{\text{M}}}{\pi\mu_0 a^2 d J_1'^2(\text{P}_{11})}}. \tag{4.6}$$

Now the cavity radius $a = 14.15\text{mm}$ and the cavity length $d = 24.6\text{mm}$, and P_{11} is a first root of Bessel function $J_1(x)$, and J_1' gives -0.403 at $x = \text{P}_{11}$. The microwave frequency is around 12.9GHz, to which the resonance frequency of TM_{110} mode is adjusted by the dimensions. So with microwave power P we get magnetic field

$$B_0 = \sqrt{\frac{\mu_0 QP}{\pi a^2 d\omega J_1'^2(\text{p}_{11})}} = 4.08 \times 10^{-3}\sqrt{P/[\text{kW}]}[\text{T}] = 40.8\sqrt{P/[\text{kW}]}[\text{gauss}] \tag{4.7}$$

The field strength distribution of the TM_{110} mode is illustrated in **Figure A.2**. It is uniform around the centre of the cavity. Calculations show that the strength of the magnetic field is reduced to half with 8mm lateral dislocation or 4.5mm vertical dislocation from the centre, so the $\overline{p}$ stopping region of $\pm 5.0\text{mm}$ is almost covered.

4.2 Transition dipole moments

The next step is to calculate the E1 transition dipole moments $\mu_m \equiv \langle f \mid \mu_z \mid i \rangle$. For matrix elements of any tensor operator, Wigner-Eckart theorem asserts that they are divided into two parts. One is orientational, and another is physical. In this case,

$$\begin{aligned}
&\langle n', l', F', J', m' \mid \mu_z \mid n, l, F, J, m \rangle \\
&\quad = (-1)^{J'+m'} \begin{pmatrix} J & 1 & J' \\ m & 0 & -m' \end{pmatrix} \langle n', l', F', J' || \mu || n, l, F, J \rangle \\
&\quad = C^{Jm10}{}_{J'm'} (n', l', F', J' || \mu || n, l, F, J). \qquad (4.8)
\end{aligned}$$

Here $\begin{pmatrix} J & 1 & J' \\ m & 0 & -m' \end{pmatrix}$ is Wigner's 3-j coefficient and $C^{Jm10}{}_{J'm'}$ is a Clebsch-Gordan coefficient, and $\langle f||\mu||i\rangle$ and $(f||\mu||i)$ mean reduced matrix element with respect to each coefficient. The reduced matrix element $\langle n', l', F', J'||\mu||n, l, F, J\rangle$ is not yet purely physical, because it contains information on the angular momentum combinations. What is purely physical is a reduced matrix element $\langle n', l'||\mu||n, l\rangle$, which we can calculate from $\overline{p}$-He^+ orbital wavefunctions. To associate $\langle n', l', F', J'||\mu||n, l, F, J\rangle$ with $\langle n', l'||\mu||n, l\rangle$ we use Racah's 6-j coefficient.

$$|\langle n', l', F', J'||\mu||n, l, F, J\rangle| = \sqrt{(2J+1)(2J'+1)} \left| \begin{Bmatrix} F' & J' & \frac{1}{2} \\ J & F & 1 \end{Bmatrix} \right| |\langle n', l', F'||\mu||n, l, F\rangle| \qquad (4.9)$$

$$|\langle n', l', F'||\mu||n, l, F\rangle| = \sqrt{(2F+1)(2F'+1)} \left| \begin{Bmatrix} l' & F' & \frac{1}{2} \\ F & l & 1 \end{Bmatrix} \right| \langle n', l'||\mu||n, l\rangle \qquad (4.10)$$

Then the results are

$$\begin{cases} |\langle 38, 34, 34+\frac{1}{2}||\mu||37, 35, 35+\frac{1}{2}\rangle| = 1.01\ \mu_\ell \\ |\langle 38, 34, 34-\frac{1}{2}||\mu||37, 35, 35-\frac{1}{2}\rangle| = 0.99\ \mu_\ell \\ |\langle 38, 34, 34+\frac{1}{2}||\mu||37, 35, 35-\frac{1}{2}\rangle| = 0.02\ \mu_\ell \end{cases} \qquad (4.11)$$

$$\begin{cases} |\langle 38, 34, 34+\frac{1}{2}, 35||\mu||37, 35, 35+\frac{1}{2}, 36\rangle| = 1.0140\ \mu_\ell \\ |\langle 38, 34, 34+\frac{1}{2}, 34||\mu||37, 35, 35+\frac{1}{2}, 35\rangle| = 0.9998\ \mu_\ell \\ |\langle 38, 34, 34-\frac{1}{2}, 34||\mu||37, 35, 35-\frac{1}{2}, 35\rangle| = 0.9998\ \mu_\ell \\ |\langle 38, 34, 34-\frac{1}{2}, 33||\mu||37, 35, 35-\frac{1}{2}, 34\rangle| = 0.9854\ \mu_\ell \\ |\langle 38, 34, 34+\frac{1}{2}, 35||\mu||37, 35, 35+\frac{1}{2}, 35\rangle| = 0.0201\ \mu_\ell \\ |\langle 38, 34, 34-\frac{1}{2}, 34||\mu||37, 35, 35-\frac{1}{2}, 34\rangle| = 0.0203\ \mu_\ell \\ |\langle 38, 34, 34+\frac{1}{2}, 34||\mu||37, 35, 35-\frac{1}{2}, 34\rangle| = 0.0200\ \mu_\ell \\ |\langle 38, 34, 34+\frac{1}{2}, 35||\mu||37, 35, 35-\frac{1}{2}, 35\rangle| = 0.0203\ \mu_\ell \\ |\langle 38, 34, 34+\frac{1}{2}, 35||\mu||37, 35, 35-\frac{1}{2}, 34\rangle| = 0.0004\ \mu_\ell \\ |\langle 38, 34, 34+\frac{1}{2}, 34||\mu||37, 35, 35-\frac{1}{2}, 35\rangle| = 0.0004\ \mu_\ell \end{cases} \qquad (4.12)$$

where $\mu_\ell \equiv \langle 38,34||\mu||37,35\rangle = 0.440$debye[31]*). These calculations assert the selection rule $\Delta l = \Delta F = \Delta J = -1$ mentioned in Chapter 2. To make transitions from F^- to F^+ we need thousand times stronger laser power, which is impossible at now. The transition moment also depends on the orientation of the $\overline{p}$ angular momentum against the electric field. That is described by the m dependence of the 3-j coefficient or the Clebsch-Gordan coefficient. The final result of the transition moments for all possible m values is shown in **Figure 4.1** for the case of $J^{+-} \rightarrow J'^{+-}$ transition. The root mean square value is 0.03debye. This value is relatively small,

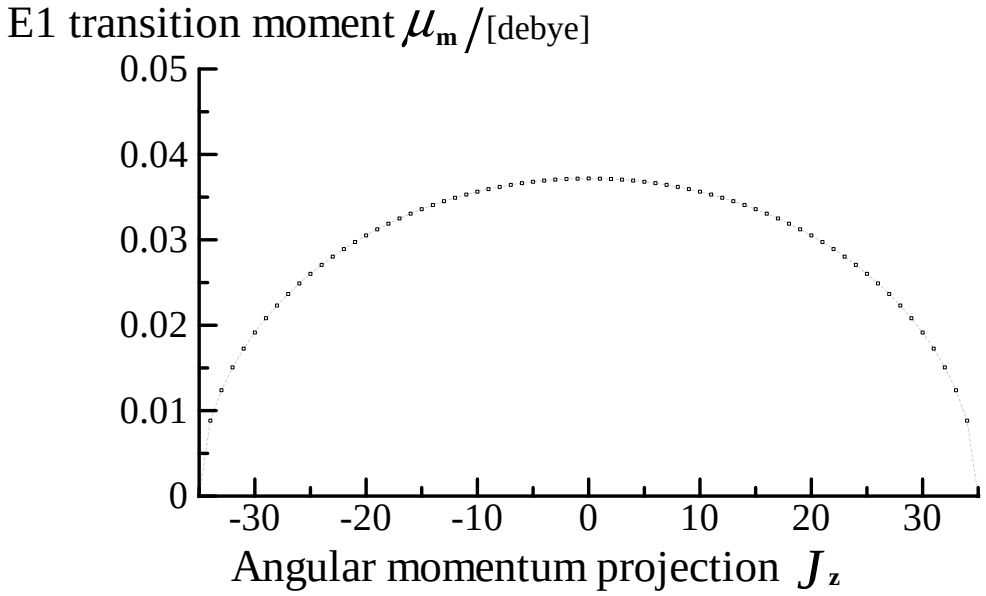

Figure 4.1: The E1 transition dipole moments μ_m for $J^{+-} \rightarrow J'^{+-}$ transition, which depend on the orientation of the total angular momentum $\vec{J}$. The more $\overline{p}$ orbital motion goes close to the xy plane, the less it is affected by the electric field perpendicular to that plane.

compared to that of a "favoured" transition, $\Delta v = \Delta(n-l-1) = 0$, which is one order larger than this[33]. It is small due to the large change of the radial form of the $\overline{p}$ wavefunction determined by the vibrational quantum number v. Despite this demerit we have no choice other than this (or other unfavoured) transition because we expect larger difference in the transition frequencies f^+ and f^-. The calculated difference[36] between f^+ and f^- is 1.767GHz, and experimentally it is determined to

*) The radiative E1 transition rate $\Gamma_{(38,34)\rightarrow(37,35)}$ is determined by μ_ℓ as

$$\Gamma_{(38,34)\rightarrow(37,35)} = \frac{4}{3}\frac{\omega_{i\rightarrow f}^3}{4\pi\epsilon_0\hbar c^3}\left[|\langle 37,35,\mathrm{m}|\mu_z|38,34,\mathrm{m}\rangle|^2 + |\langle 37,35,\mathrm{m}+1|\mu_+|38,34,\mathrm{m}\rangle|^2 + |\langle 37,35,\mathrm{m}-1|\mu_-|38,34,\mathrm{m}\rangle|^2\right]$$
$$= \frac{4}{3}\frac{\omega_{i\rightarrow f}^3}{4\pi\epsilon_0\hbar c^3}(38,34||\mu||37,35)^2 = \frac{4}{3}\frac{\omega_{i\rightarrow f}^3}{4\pi\epsilon_0\hbar c^3}\frac{1}{2l_i+1}\mu_\ell^2 \qquad (\mu_\pm \equiv \mu_x \pm i\mu_y)$$

and $\mu_\ell = 0.440$[debye] $= 1.47\times10^{-30}$[Cm] gives $\Gamma = 2.3$kHz[31], which is negligibly smaller than the Auger transition rate $\Gamma_{\mathrm{Auger}} = 84.5$MHz.[33]

be 1.70 ± 0.05GHz[16]. On the other hand, favoured transitions have smaller values, as 0.5GHz of $(n, l) = (39, 35) \rightarrow (38, 34)$ transition. Our current laser system has the larger bandwidth of $600 \sim 800$MHz, and is not capable of resolving these small differences. To cause the unfavoured transition of the one tenth E1 moment we need hundred times larger laser power than the favoured transition spectroscopies.

4.3 Laser transition process

Now we will discuss about the laser transition process from the metastable states to the short-lived states. To describe a nonconservative system where total population is not conserved, the method of density matrix is more suitable than the simple wavefunction representation. Though the behaviour of a single $\overline{p}$-He^+ is unpredictable, the density matrix $\hat{\rho} = \sum_{m,n} |m\rangle \rho_{mn} \langle n|$ represents the averaged property (e.g. population) of the ensemble.

First we should limit our discussion to one particular transition. Applying a typical result of the two-state model, we obtain the following time-evolution equation:

$$\frac{d}{dt} \begin{pmatrix} \rho_1 \\ \rho_2 \\ \rho_x \\ \rho_y \end{pmatrix} = \begin{pmatrix} -\gamma_{\rm rad} & 0 & 0 & \frac{1}{2}\Omega(t) \\ 0 & -\gamma_{\rm Auger} & 0 & -\frac{1}{2}\Omega(t) \\ 0 & 0 & -\gamma_{\rm T} & -\Delta\omega \\ -\Omega(t) & \Omega(t) & \Delta\omega & -\gamma_{\rm T} \end{pmatrix} \begin{pmatrix} \rho_1 \\ \rho_2 \\ \rho_x \\ \rho_y \end{pmatrix} \tag{4.13}$$

Here ρ_1 stands for the population of the initial state (i.e. one of the state in the J^{++}, J^{+-}, J^{-+} or J^{--} with a particular J_z) and ρ_2 is the population of the corresponding (i.e. $\Delta J_z = 0, \Delta l = \Delta F = \Delta J = -1$) final state. The nondiagonal part of the density matrix is divided to the real part ρ_x and the imaginary part ρ_y. The transition (or oscillation) from ρ_1 to ρ_2 is induced by the Rabi frequency Ω, which is determined by the transition moment μ_m of the states as

$$\Omega(t) = \frac{\mu_m E_0(t)}{\hbar}, \ \Omega(t)/2\pi = 13.82 \times \mu_m/[\text{debye}] \times \sqrt{P(t)/[\text{MW/cm}^2]}[\text{GHz}] \tag{4.14}$$

in this case. The population escape from the states is implemented by the radiative decay rate $\gamma_{\rm rad}$ and the Auger decay rate $\gamma_{\rm Auger}$[†)], and the term $\Delta\omega = \omega_{\rm laser} - \omega_{\rm f \rightarrow i}$ is the detuning of the laser. The last term $\gamma_{\rm T}$ has two physical meanings. First, it relaxes the correlation of the oscillations among the atomcules. This is similar to what is called a transverse relaxation in the field of magnetic resonance. The relaxation rate $\gamma_{\rm T}$ is given as

$$\gamma_{\rm T} = \frac{\gamma_{\rm rad} + \gamma_{\rm Auger}}{2} + \gamma_{\rm p}. \tag{4.15}$$

The former part comes from the loss of the total population, while the latter, called "collisional width", is given in a collision theory by weak and frequent collisions with

[†)] The names of the rates are given by the main sources of depopulation, though other effects can be included.

other helium atoms (see **Appendix B**). So $\gamma_{\rm p}$ is a function of the target helium gas density. Another meaning of $\gamma_{\rm T}$ is that it increases the bandwidth of the transition spectrum, as shown later. The former part is understood as the natural width of the transition, and $\gamma_{\rm p}$ is the source of the collisional broadening.

Before going ahead, it will be informative to discuss the behaviour of solutions of the equation (4.13). This differential equation has an explicit form, and we can easily solve it numerically. Assuming initial populations of $(\rho_1 = 1, \rho_2 = 0, \rho_x = \rho_y = 0)$ and typical values of parameters, we got temporal profile of the transition as shown in **Figure 4.2**[‡]. The numerical error is estimated to be less than 10^{-7}, which is negligible compared to other ambiguities.

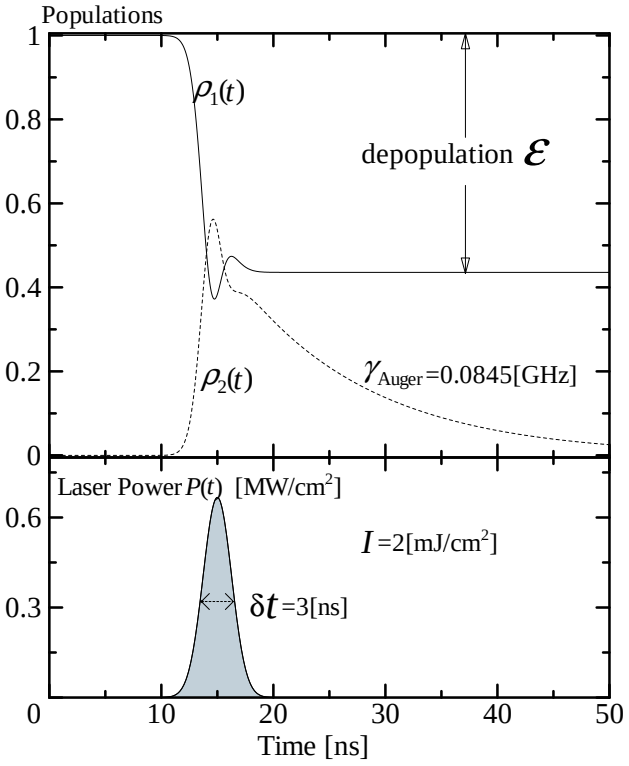

Figure 4.2: An example solution of the equation (4.13). Parameters are chosen to be $\mu_m = 0.03$debye, $\gamma_{\rm p}/2\pi = 0.20$GHz, $\Delta\omega/2\pi = 0$. Part of the population ρ_1 in the metastable state is transfered by the laser into the short-lived state and decays with the rate $\gamma_{\rm Auger}$. The fraction of depopulation is given by $\epsilon = 1 - \rho_1(\infty) = \int_{-\infty}^{\infty}(\gamma_{\rm Auger}\rho_2(t))dt$. The effect of the radiative loss of ρ_1 is not included now.

[‡]Equations are solved by 4-th order Runge Kutta method.

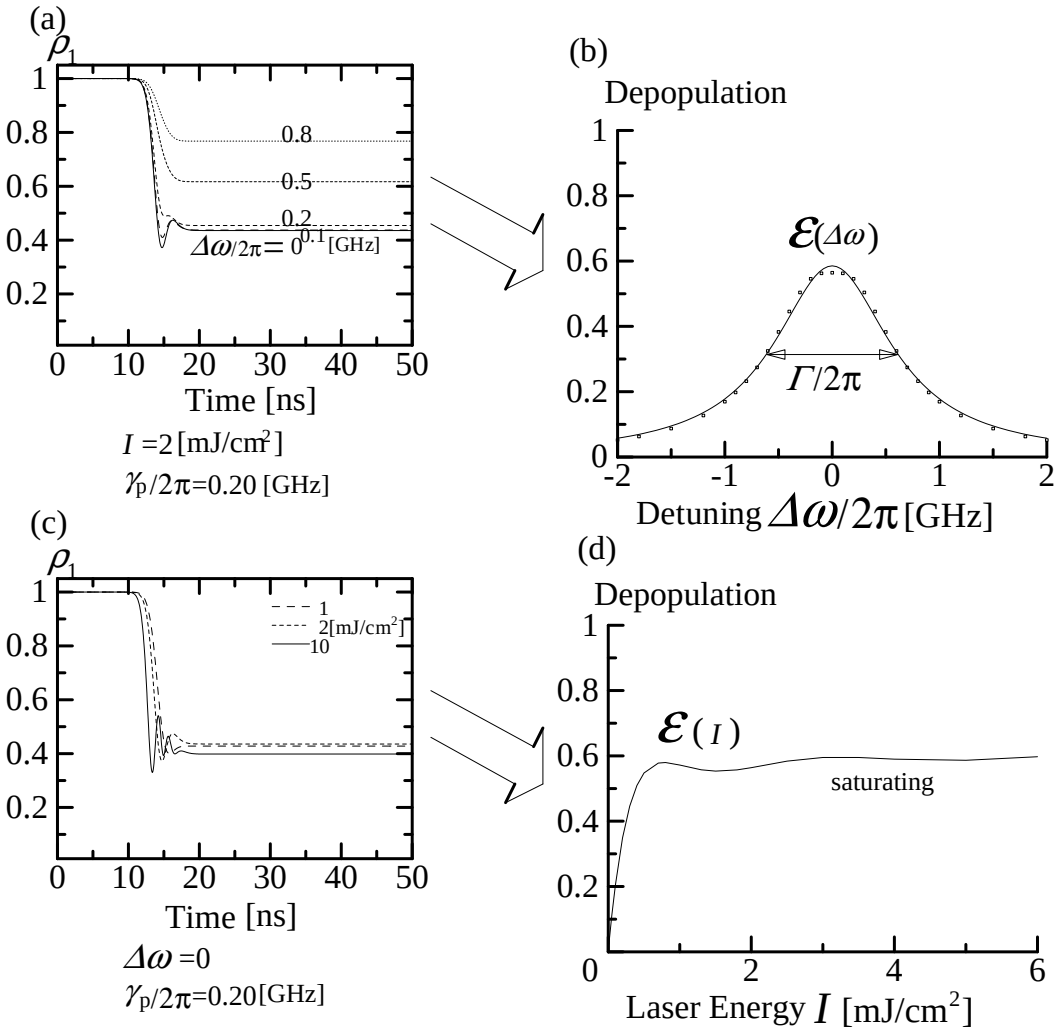

Figure 4.3: Examples. (a),(b): Frequency response of the depopulation (squares). The shape of the resonance is similar to Lorentz curve (line). (c),(d): Energy dependence of the depopulation. It shows a saturation according to the laser intensity.

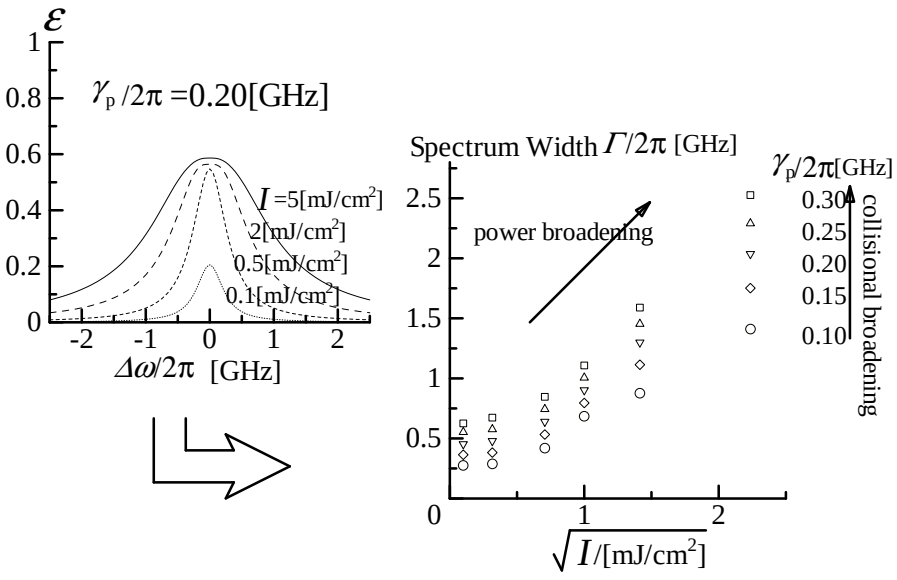

Figure 4.4: Widths of the depopulation spectra. Higher laser intensity causes a power broadening, and larger collisional width causes a collisional broadening.

The short but intense laser pulse induces almost instantaneous population transfer from the parent state to the daughter state, and makes an exponential-like annihilation spike which is proportional to the daughter state population. The total number of the annihilation from the daughter state is equal to the population loss of the parent state, and ϵ, the excitation efficiency or the fraction of the depopulation, is about half if the laser parameters are adequately tuned. Even with a far more strong laser power, we cannot get much higher depopulation. This phenomenon is called a saturation (see **Figure 4.3(d)**). The increase of the laser power only activates the oscillative behaviour of the population, called Rabi oscillation, during the laser period and hardly affects the excitation efficiency. In contrast, if the laser frequency goes away from the resonance, the annihilation will become smaller. By plotting ϵ against $\Delta\omega$, we get spectra of depopulation efficiencies as shown in **Figure 4.3(b)**, which are quite similar to Lorentz functions. The FWHM Γ is a function of the relaxation rate γ_T and the laser intensity I, and **Figure 4.4** shows their relations. We find that Γ increases with the laser intensity I. This is called power broadening. It also increase with γ_p, the collisional width. Thus the relaxation of the correlation is related with the broadening of the spectrum. Note that as the laser intensity decreases, $\Gamma/2$ approaches to γ_T.

Now we return to the $\overline{p}$-He$^+$ case. As discussed before, there are many states and many transitions with different angular momenta. Considering the short laser period of 3ns, we assume that there is no disturbance of the $\overline{p}$-He$^+$ angular momen-

tum during the transition, and all the transitions are reduced to many two-state transitions as we have already seen. They are independent of each other, and yet they have different Rabi frequencies Ω and obey different equations. To solve the problem we can calculate all these equations independently.

To make the argument realistic, one more complexity has to be overcome. The equation (4.13) is derived with the assumption that the incident laser is ideally monochromatic. However, this assumption is not satisfied enough. Actually our laser has a finite bandwidth, and there is also Doppler broadening as we discussed in **Section 3.5**. So different atomcule would suffer the electric field of slightly different frequency, and the width of the spectrum would become broadened. One way to take this effect into consideration is to regard the laser frequency ω' as a stochastic variable which subjects to a distribution function $W(\omega')$. Then we must convolute the result from former equations with $W(\omega')$. For the moment we assume the form of the $W(\omega')$ as

$$W(\omega' - \omega) = \frac{1}{\sqrt{\pi(\delta\omega/2)^2/\ln 2}} \exp\left(-\ln 2 \frac{(\omega' - \omega)^2}{(\delta\omega/2)^2}\right) \tag{4.16}$$

where ω is the central frequency. Our laser has a bandwidth of $600 \sim 800$MHz in itself, and the Doppler broadening is 320MHz (see **section 3.5**). So the total compound laser broadening $\delta\omega$ calculated by root sum square of the two widths is at most 860MHz.

The temporal profile which includes all these effects is shown in **Figure 4.5**. It is not easy to calculate nor measure the collisional width with satisfactory accuracy. So we assumed $\gamma_p/2\pi = 0.20$GHz in accordance with that of the transition $(n, l) = (39, 53) \rightarrow (38, 34)$ at the same conditions[20], the most accurate one studied in the former experiment.

We soon notice that the Rabi oscillations for each angular momentum components are averaged out and less apparent. About 45 % of the $\overline{p}$ in the J^{+-} level are excited almost immediately after the laser application. **Figure 4.6** shows the survived fraction for each angular momentum projection. From this we may assert that the result of the transition is fairly isotropic.

The spectrum against the laser frequency is shown in **Figure 4.7**, and that against laser intensity is shown in **Figure 4.8**. Now the frequency spectra are a bit different from Lorentz curves because of the Gaussian laser broadenings. The depopulation efficiency ϵ increases almost monotonously with the laser intensity I.

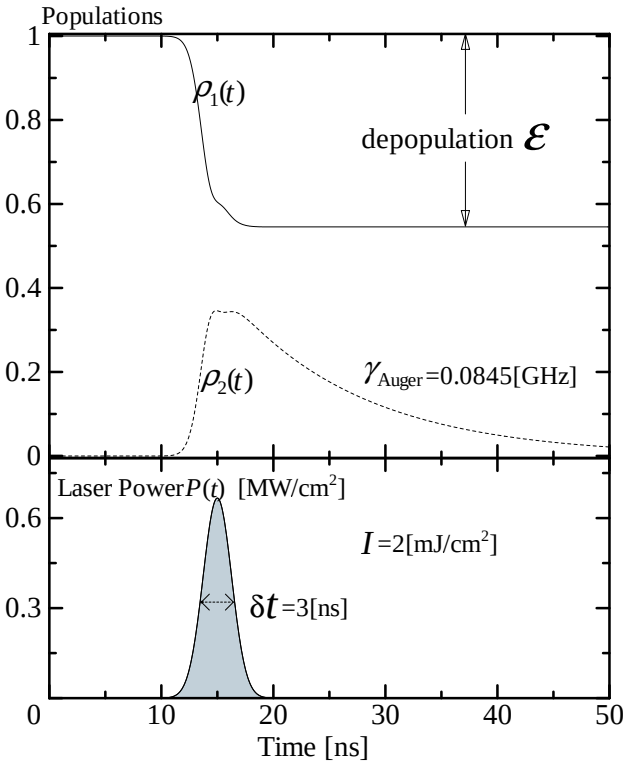

Figure 4.5: Temporal profile of the resonant transition ($J^{+-} \rightarrow J'^{+-}$). Populations of the degenerated states are averaged from $J_z = -35$ to $J_z = 35$. The collisional width $\gamma_p/2\pi$ is chosen to 0.20GHz from a former experimental study on the collisional effect[20].

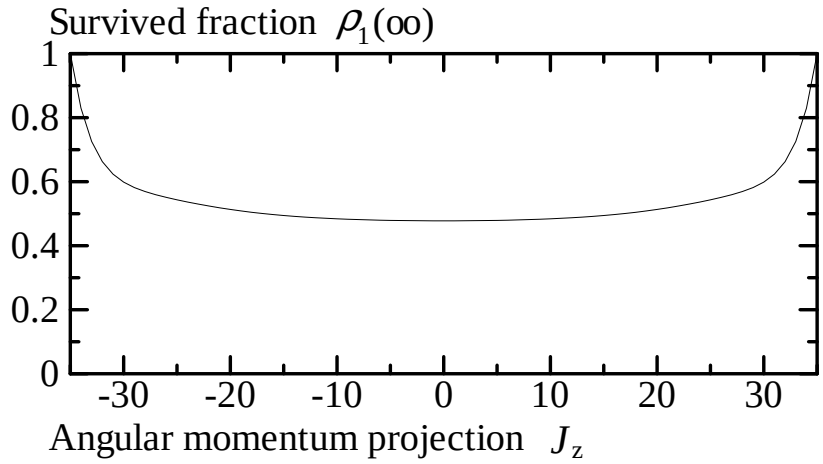

Figure 4.6: The final population of each J_z state in the transition of **Figure 4.5**. Except for the edge region the populations are almost the same.

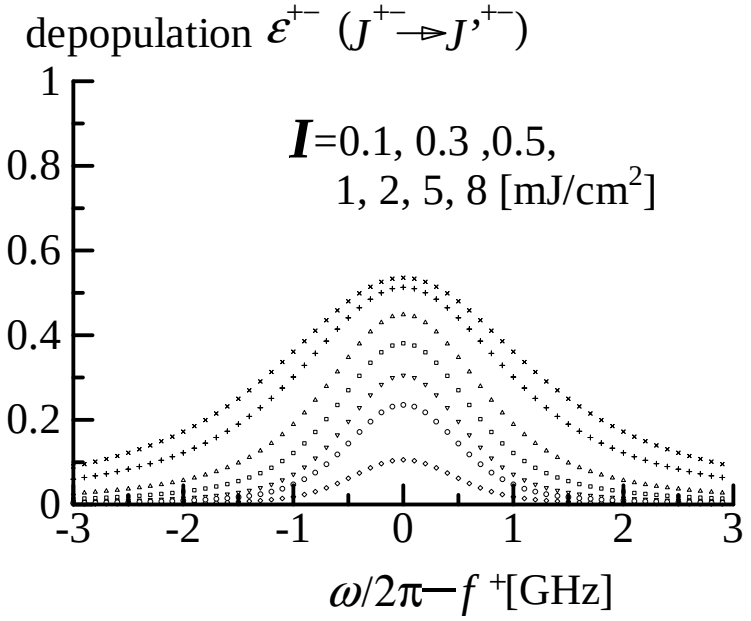

Figure 4.7: Frequency response of the depopulation for $J^{+-} \rightarrow J'^{+-}$ transition with many laser intensities. Higher intensity leads to higher depopulation and wider spectrum. The centre of the spectra means the resonance frequency F^+. The collisional width $\gamma_p/2\pi = 0.20$GHz.

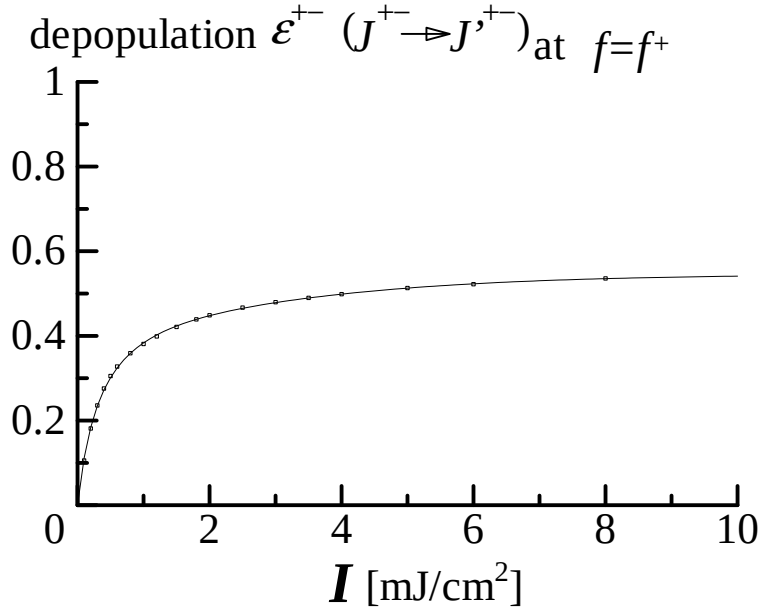

Figure 4.8: Energy dependence of the depopulation for $J^{+-} \rightarrow J'^{+-}$ transition (squares). They are fit with a rational function $a\frac{b_1 I + b_2 I^2 + b_3 I^3}{c + b_1 I + b_2 I^2 + b_3 I^3}$, to $a = 0.549$, $b_1 = 21.6$, $b_2 = -2.88$, $b_3 = 0.67$, $c = 8.37$.

There are some subjects we must examine.

1. Differences between the SHFS levels

   The level J^{++} consists of 36 degenerate states, and J^{--} is composed of 34 states. Therefore the transition efficiency $\epsilon^{\pm\pm}$ for these levels may be different from that of J^{+-}. The calculated results are in **Figure 4.9**. The results assert that there are no significant differences between J^{+-} and J^{++}, and J^{-+} and J^{--}. Though the degeneracy of J^{-+} is equal to that of J^{+-}, its frequency spectrum is shifted because of the different resonance frequency f^-. So for the fixed laser frequency f^+, $\overline{p}$-He^+ in J^{-+} or J^{--} has smaller depopulation efficiency (name "ϵ^-") than that in J^{+-} or J^{++} (name "ϵ^+"), and population asymmetry is induced after the irradiation.

2. Laser pulse length dependence

   Once there was a suspicion (within our collaboration) that the fluctuation of the laser pulse length might be critical to the experiment, because of its shortness against the Rabi frequency. In the former experiment we used long pulses of excimer lasers, and the pulse duration was considerably longer than the Rabi oscillation cycle. In the present case, however, the Rabi oscillation cycle is almost the same length of 3ns as the pulselength. So calculations with some pulselengths were performed to demonstrate whether it is a problem or not. The result is shown in **Figure 4.10**. Concludingly for fairly large fluctuations they are not affected so much.

3. Ambiguity associated with the collisional width

   As mentioned earlier, the adopted value of the collisional width has some ambiguity. Even for the best measured width of the $(n, l) = (39, 35) \rightarrow (38, 34)$ transition there remains about 0.10GHz systematic error[20]. So calculations with some collisional widths are performed. The results in **Figure 4.11** show that ϵ^-, which is understood as the depopulation efficiency at $\Delta f = 1.77$GHz off resonance, is more affected by the change of the width than ϵ^+, that the effect is large at high laser intensity, and that around $I \sim 2.0\text{mJ/cm}^2$ the ambiguities of ϵ^+ and ϵ^- cancel each other and $\epsilon^+ - \epsilon^-$ does not change so much. We also notice that $I = 2.0 \sim 2.5\text{mJ/cm}^2$ gives the maximum of $\epsilon^+ - \epsilon^-$, which determines the asymmetry and microwave resonance signal. Therefore the best laser intensity I we choose from now is 2.0mJ/cm^2. Then the depopulation efficiency ϵ^+ is 0.45 ± 0.04, ϵ^- is 0.07 ± 0.03 and $\epsilon^+ - \epsilon^-$ is 0.38 ± 0.02.

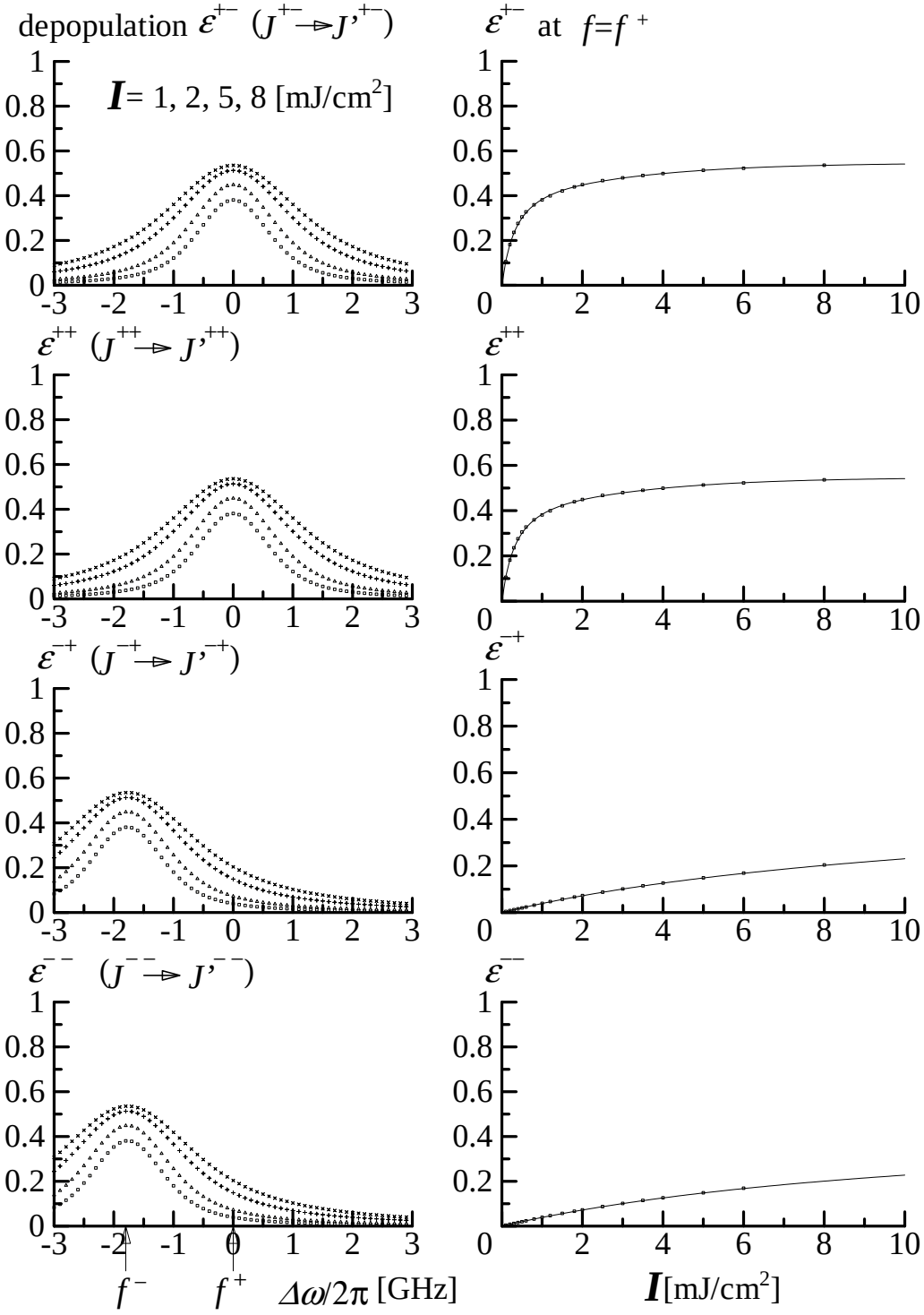

Figure 4.9: The frequency and intensity spectra of the depopulation for each J.

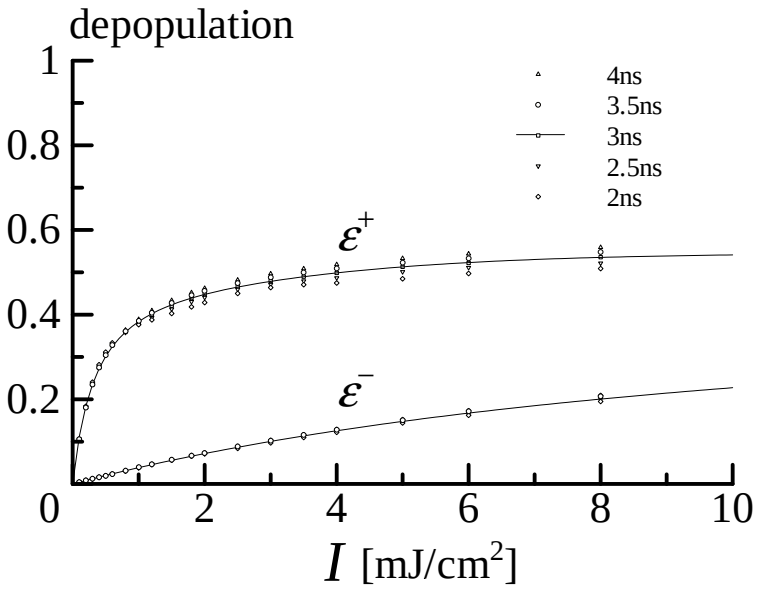

Figure 4.10: Depopulation spectra against intensity, with some laser pulse lengths.

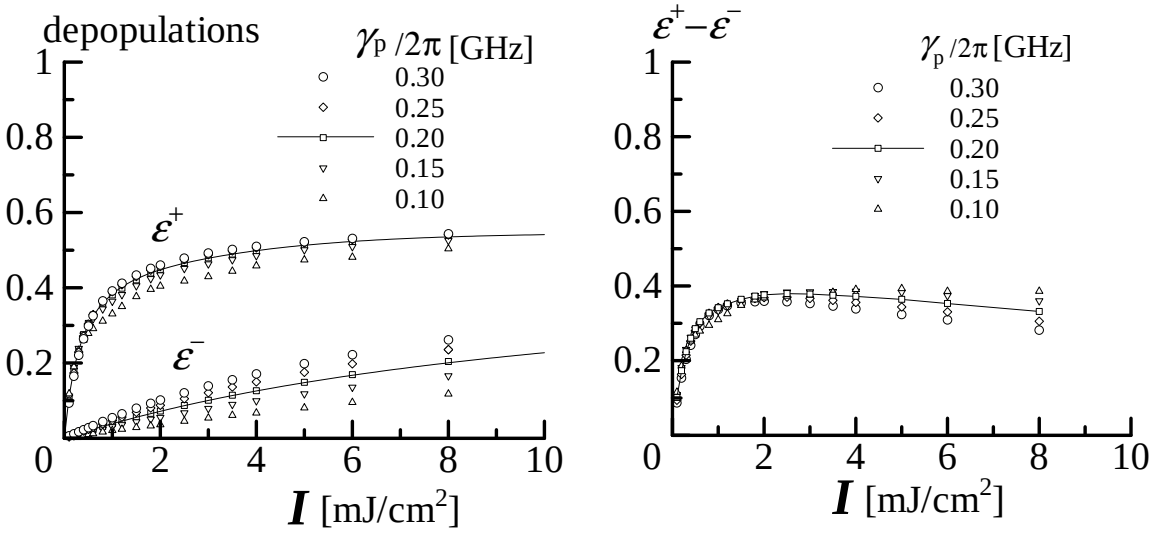

Figure 4.11: Depopulation spectra against intensity, with some collisional widths. From the right figure we conclude that the best laser intensity is 2.0mJ/cm^2.

4.4 Microwave transition

Now we are able to discuss the whole process including microwave transition. The microwave transition occurs between the states with $\Delta l = 0$, $\Delta F = \pm 1$, $\Delta J = \pm 1$ (0), and $\Delta J_z = 0$. The transition dipole moments are given just as that of the laser. Considering that $\overrightarrow{\mu_{\rm M}}$, the magnetic dipole moment of the $\overline{p}$-He^+, is well described by the electron spin magnetic moment $g_{(e)s}\mu_{\rm B}\vec{s}_{\rm e}$ because of its light mass and null orbital angular momentum, we get

$$\begin{aligned}(\mu_{\rm M})_m &= \langle 37,35,35-\frac{1}{2},J',m' \mid (\mu_{\rm M})_z \mid 37,35,35+\frac{1}{2},J,m\rangle \\ &= (-1)^{J'+m'}\begin{pmatrix} J & 1 & J' \\ m & 0 & -m' \end{pmatrix}\langle 37,35,35-\frac{1}{2},J'||\mu_{\rm M}||37,35,35+\frac{1}{2},J\rangle\end{aligned} \tag{4.17}$$

$$\begin{aligned}&|\langle 37,35,35-\frac{1}{2},J'||\mu_{\rm M}||37,35,35+\frac{1}{2},J\rangle| \\ &= \sqrt{(2J+1)(2J'+1)}\left|\begin{Bmatrix} 35-\frac{1}{2} & J' & \frac{1}{2} \\ J & 35+\frac{1}{2} & 1 \end{Bmatrix}\right| |\langle 37,35,35-\frac{1}{2}||\mu_{\rm M}||37,35,35+\frac{1}{2}\rangle|\end{aligned} \tag{4.18}$$

$$\begin{aligned}&|\langle 37,35,35-\frac{1}{2}||\mu_{\rm M}||37,35,35+\frac{1}{2}\rangle| \\ &= \sqrt{5040}\left|\begin{Bmatrix} \frac{1}{2} & 35-\frac{1}{2} & 35 \\ 35+\frac{1}{2} & \frac{1}{2} & 1 \end{Bmatrix}\right| \langle s_{\rm e}=\frac{1}{2}||\mu_{\rm M}||s_{\rm e}=\frac{1}{2}\rangle \\ &= \sqrt{\frac{5040}{213}}\langle s_{\rm e}=\frac{1}{2}||\mu_{\rm M}||s_{\rm e}=\frac{1}{2}\rangle\end{aligned} \tag{4.19}$$

The reduced matrix element $\langle s_{\rm e}=\frac{1}{2}||s_{\rm e}||s_{\rm e}=\frac{1}{2}\rangle = \frac{\sqrt{6}}{2}$ is directly calculable, so

$$|\langle 37,35,35-\frac{1}{2}||\mu_{\rm M}||37,35,35+\frac{1}{2}\rangle| = 11.9\mu_{\rm B} \tag{4.20}$$

and

$$\begin{aligned}|\langle 37,35,35-\frac{1}{2},35||\mu_{\rm M}||37,35,35+\frac{1}{2},36\rangle| &= 12.0\mu_{\rm B} \\ |\langle 37,35,35-\frac{1}{2},34||\mu_{\rm M}||37,35,35+\frac{1}{2},35\rangle| &= 11.8\mu_{\rm B} \\ |\langle 37,35,35-\frac{1}{2},35||\mu_{\rm M}||37,35,35+\frac{1}{2},35\rangle| &= 0.238\mu_{\rm B}.\end{aligned} \tag{4.21}$$

The Rabi frequency for the magnetic transition is given by $\Omega_{\rm M} = \frac{(\mu_{\rm M})_m B_0}{\hbar}$, or,

$$\Omega_{\rm M}/2\pi = 1.40 \times ((\mu_{\rm M})_m/\mu_{\rm B}) \times (B_0/[\text{gauss}])\ [\text{MHz}] \tag{4.22}$$

For the moment let us ignore the $\Delta J = 0$ transitions, for their different resonance frequency and small transition moments. There are two independent two-state transitions, $(J^{++}\ J^{-+})$ and $(J^{+-}\ J^{--})$. For the population components of $J_z = m$ we have these equations.

$$\frac{d}{dt}\begin{pmatrix}\rho_{-+}\\ \rho_{++}\\ \rho_{x+}\\ \rho_{y+}\end{pmatrix}_{(m)} = \begin{pmatrix} -\gamma_{37} & 0 & 0 & \frac{1}{2}\Omega_{\mathrm{M}_+(m)} \\ 0 & -\gamma_{37} & 0 & -\frac{1}{2}\Omega_{\mathrm{M}_+(m)} \\ 0 & 0 & -(\gamma_{37}+\gamma_{\mathrm{Mp}}) & -(\omega_{\mathrm{M}}-\omega_{\mathrm{HF}_+}) \\ -\Omega_{\mathrm{M}_+(m)} & \Omega_{\mathrm{M}_+(m)} & (\omega_{\mathrm{M}}-\omega_{\mathrm{HF}_+}) & -(\gamma_{37}+\gamma_{\mathrm{Mp}}) \end{pmatrix} \begin{pmatrix}\rho_{-+}\\ \rho_{++}\\ \rho_{x+}\\ \rho_{y+}\end{pmatrix}_{(m)} \quad (m = -36 \sim 36)$$

$$\frac{d}{dt}\begin{pmatrix}\rho_{--}\\ \rho_{+-}\\ \rho_{x-}\\ \rho_{y-}\end{pmatrix}_{(m)} = \begin{pmatrix} -\gamma_{37} & 0 & 0 & \frac{1}{2}\Omega_{\mathrm{M}_-(m)} \\ 0 & -\gamma_{37} & 0 & -\frac{1}{2}\Omega_{\mathrm{M}_-(m)} \\ 0 & 0 & -(\gamma_{37}+\gamma_{\mathrm{Mp}}) & -(\omega_{\mathrm{M}}-\omega_{\mathrm{HF}_-}) \\ -\Omega_{\mathrm{M}_-(m)} & \Omega_{\mathrm{M}_-(m)} & (\omega_{\mathrm{M}}-\omega_{\mathrm{HF}_-}) & -(\gamma_{37}+\gamma_{\mathrm{Mp}}) \end{pmatrix} \begin{pmatrix}\rho_{--}\\ \rho_{+-}\\ \rho_{x-}\\ \rho_{y-}\end{pmatrix}_{(m)} \quad (m = -35 \sim 35) \tag{4.23}$$

where $\gamma_{37} = 0.718$MHz[33] is the rate of the radiative transition from $(37, 35)$ to $(36, 34)$, and γ_{Mp} is the collisional width of the microwave transition. The width γ_{Mp} is considered to be significantly small compared to the laser collisional width γ_{p}, because in this case the spatial structures of the initial and final states are almost the same and the perturber atoms do not induce different effects on both the states. Because the main source of the width is not a scalar but a tensorial interaction, however, the calculation of γ_{Mp} is far more difficult than that of γ_{p}. The most elaborate estimation[43] is performed by regarding it as a perturbation of the scalar interaction, and their conversion ratio has a large ambiguity. The estimated width at our He density amounts to $\gamma_{\mathrm{Mp}}/2\pi = 0.5 \sim 5$MHz.

Figure 4.12 demonstrates the scheme of the microwave transition. At the time $t = 0$ a $\overline{p}$ pulse comes from AD with a duration of $200 \sim 500$ns[24, 25]. About 3% of the $\overline{p}$ form $\overline{p}$-He^+, and initially 10% of them fall in the $(37, 35)$ level[34]. This and other initial populations are determined from the former laser spectroscopy with the digital counting method. For simplicity we assume constant arrival of the $\overline{p}$ during that period. After the duration of the $\overline{p}$ pulse the population of each $J^{\pm\pm}$ level decreases slowly by radiative transition. There are also feedings by radiative transition from the upper level $(n, l) = (38, 36)$ (see **Figure 2.1**), therefore the level $(38, 36)$ and its parent level $(39, 37)$ which have initial populations are taken into account.

At a time $t = t_1$ we irradiate a laser beam of a frequency f^+, then the populations in J^{++} and J^{+-} are depopulated into short-lived states by the efficiency $\epsilon^+ = 0.45$. From the former result of the laser transition calculation (**Figure 4.6**) we assumed isotropic depopulation (i.e. no difference in ϵ for different J_z states). The populations in J^{-+} and J^{--} are depopulated by the smaller efficiency $\epsilon^- = 0.07$,

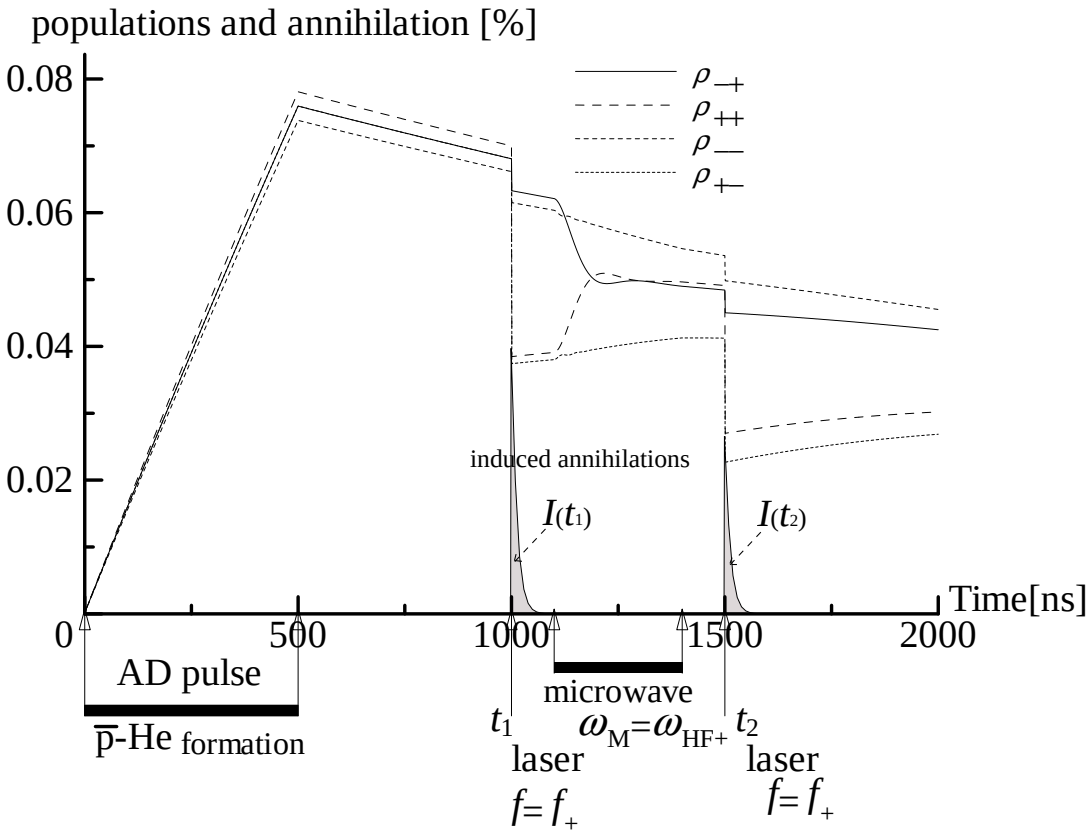

Figure 4.12: Example diagram of the microwave resonant transition between J^{-+} and J^{++} levels. The laser depopulates J^{++} and J^{+-}, then the microwave mixes the populations of J^{++} and J^{-+}, and ρ_{++} is regained. The microwave power is set to 10W, then $B_0 \sim 4$gauss and $\Omega_M/2\pi \sim 4.5$MHz. The percents of the populations are taken against the total number of the incident antiprotons. The collisional width $\gamma_{Mp}/2\pi$ is temporally assumed to be 5MHz.

thus there occurs population asymmetry. The depopulated $\overline{p}$ give rise to an induced annihilation spike. For one incident $\overline{p}$ the number of the induced annihilation will be $I(t_1) = 7.1 \times 10^{-4}$.

Then we begin to send microwave field of the frequency ν_{HF_+}. The microwave transitions occur between J^{--} and J^{+-}, and ρ_{++} and ρ_{-+} are equalized. Comparing with the case of **Figure 4.13**, where no microwave field is supplied, we find that ρ_{++} is increased by the microwave at a time $t = t_2$, after the transition. Again we

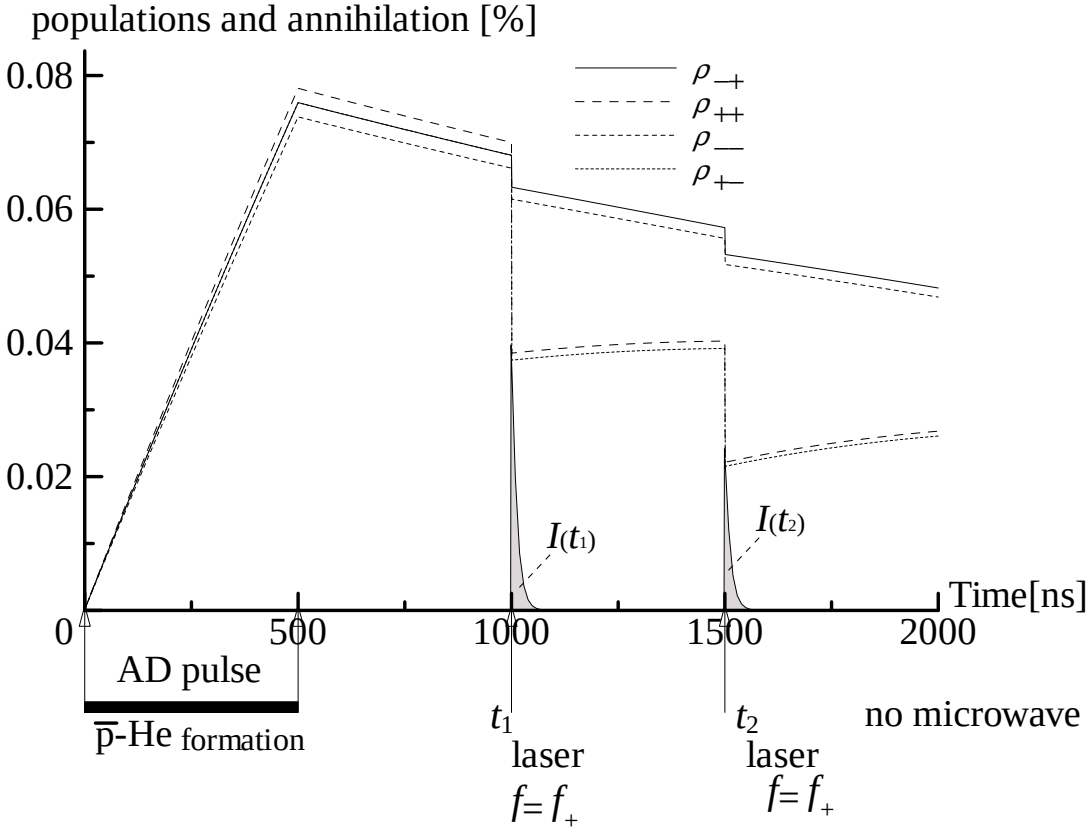

Figure 4.13: Example diagram of the population of the each level, where no microwave field is supplied.

irradiate the laser beam at $t = t_2$, and it is found that the induced annihilation intensity $I(t_2)$ becomes larger than that of the no-microwave case. Then we are able to know the occurrence of the microwave resonance by counting $I(t_2)$. We will find some gain of the $I(t_2)$ when it takes place.

However, we must say that the signal of the microwave transition (or the gain of $I(t_2)$) is quite small and it is difficult to find it. To the successful experiment it is better to know the behaviour of the signal which we will get. In the experiment we can choose the power, frequency and duration of the microwave. It is natural that to observe the microwave transition between the HFS sublevels higher microwave

power is preferable. The population asymmetry induced by the first laser decreases with time (even faster than the populations) by the radiative transition rate γ_{37}, thus the microwave duration T should be as short as possible. In short,

$$\gamma_{37} T \ll 1 \tag{4.24}$$

is required. On the other hand

$$\Omega_{\mathrm{M}}/2\pi \times T \geq \frac{1}{2} \tag{4.25}$$

is necessary for the sufficient microwave transition to occur. If we try to resolve the SHFS, however, higher power becomes a defect because of the power broadening. The half-width of the spectrum is roughly given by $\Gamma/2 \approx \gamma_{\mathrm{Mp}} + \Omega_{\mathrm{M}}$, and in order to resolve the SHFS,

$$\frac{\Delta\nu_{\mathrm{HF}\pm}}{2} \gg \frac{\Gamma}{2}/2\pi \sim \gamma_{\mathrm{Mp}}/2\pi + \Omega_{\mathrm{M}}/2\pi \tag{4.26}$$

must be satisfied. Considering $\Delta\nu_{\mathrm{HF}\pm} \approx 28\mathrm{MHz}$ and $\gamma_{37} \sim 0.7\mathrm{MHz}$, initially we estimate the suitable parameters as $T = 300\mathrm{ns}$ and $\Omega_{\mathrm{M}}/2\pi \sim 1.5\mathrm{MHz}$ (which corresponds to the microwave power of about 1W).

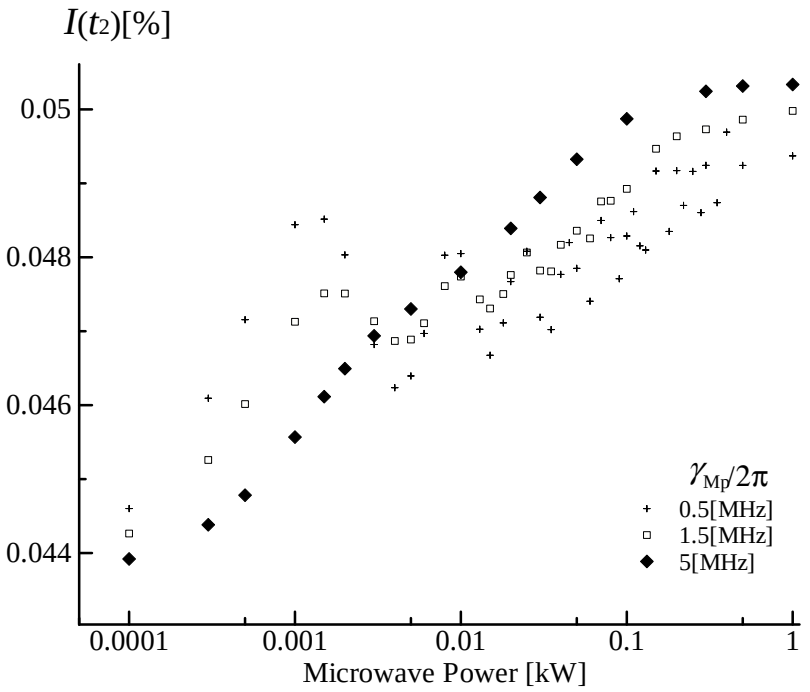

Figure 4.14: $I(t_2)$ plotted against the microwave power.

Figure 4.14 shows the intensity of the second annihilation spike $I(t_2)$ with some microwave powers. Calculations were performed with three values of γ_{Mp},

but with same microwave duration of 300ns and frequency $\nu_{\mathrm{HF}+}$. It shows that we will get a large gain of the intensity with microwave power of higher than 1kW. With this power we get the spectra of microwave transition signal as shown in **Figure4.15**. Though the gain of the signal is large, we cannot determine the centre

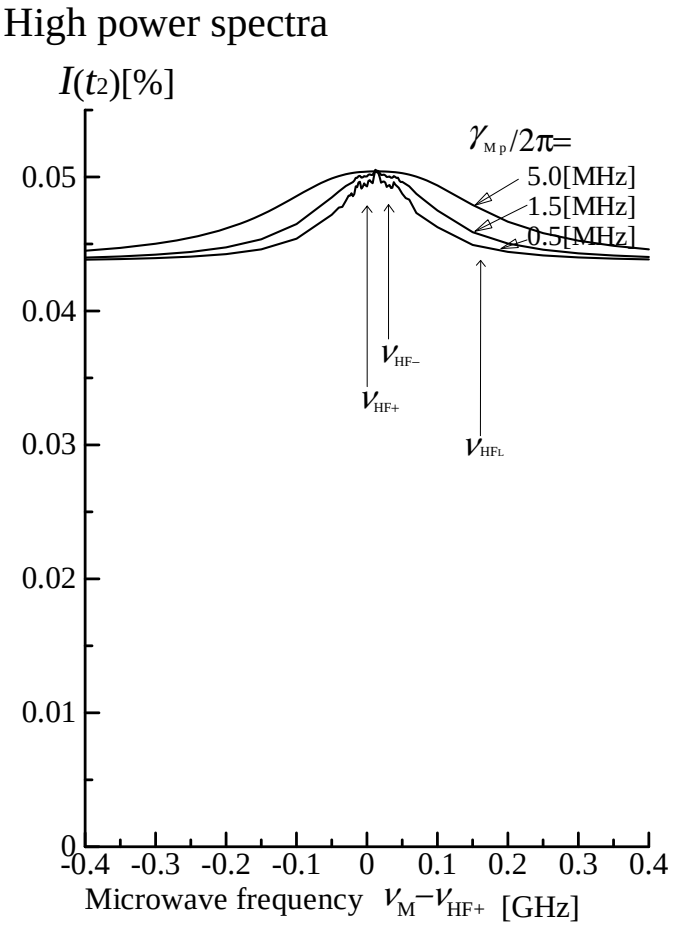

Figure 4.15: The microwave transition signal spectrum at microwave power of 1kW, or $B_0 \sim 40$gauss. The signal is expressed by the number of the induced annihilation $I(t_2)$ against the total incident $\overline{p}$ number. Calculations are performed for three values of γ_{Mp}. With this high power we cannot resolve the SHFS. The FWHM of the spectra are 350MHz, 230MHz and 125MHz for each γ_{Mp}.

of the resonance with better precision than 10^{-3}. Nevertheless operations on this microwave power will be helpful to know whether there are microwave transitions at all.

To determine the resonance frequency precisely we must reduce the microwave power. From **Figure 4.14** we choose the microwave power of 1.5W. This power gives

a fairly large gain in case of small γ_{Mp}, because in such case population inversion (not equalization) between the J^{++} and J^{-+} occurs at $T = 300$ns (see **Figure 4.16**). **Figure 4.17** shows the final result of the spectra. With this power the SHFS is

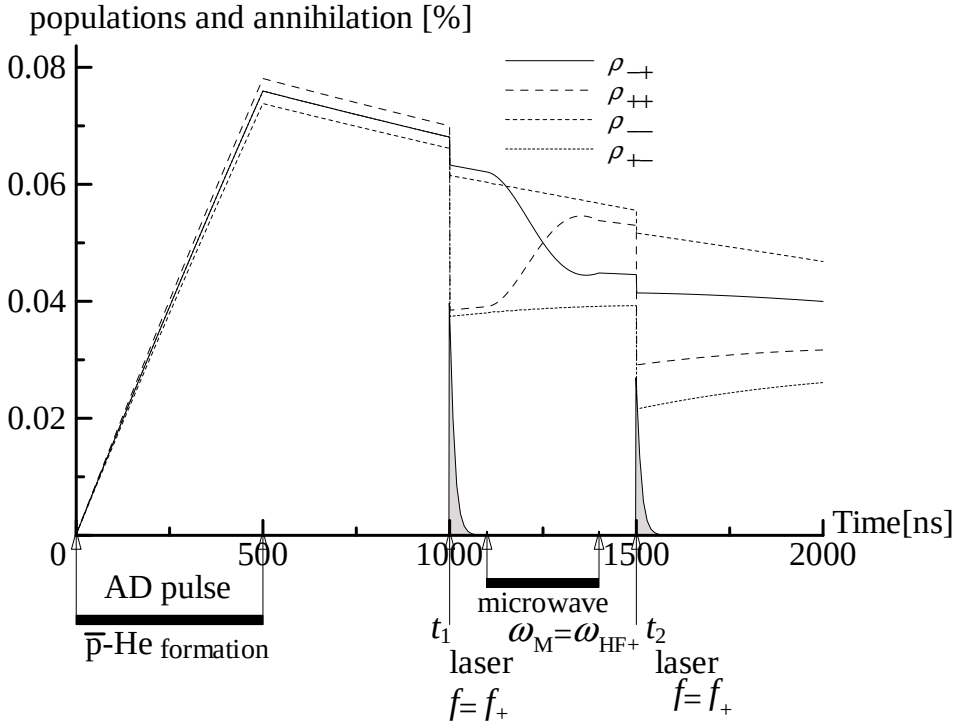

Figure 4.16: Example diagram of the microwave transition, with microwave power of 1.5W. Due to the average Rabi frequency of about 1.5MHz and small relaxation rate of $\gamma_{\mathrm{Mp}}/2\pi = 0.5$MHz population inversion of the J^{++} level and J^{-+} occurs at the end of $T = 300$ns microwave duration.

resolved at any collisional width. The gain of the second induced annihilation is summarized in **Table 4.1**.

To end with this section, let us discuss the observation of the microwave transition $\mathrm{HF_L}$. The equations (4.21) show that the $\mathrm{HF_L}$ transitions have a fifty times smaller transition matrix elements, and require 2500 times higher field energy than the $\mathrm{HF_\pm}$ transitions. It means a field power P of at least 2.5kW. However, the power broadening of the $\mathrm{HF_\pm}$ transitions will begin to overwhelm the spectrum of the $\mathrm{HF_L}$ transition at $P = 1$kW, as shown in **Figure 4.15**. With $P \sim 2.5$kW, populations of the four levels are equalized by the strong microwave, and there will be no room

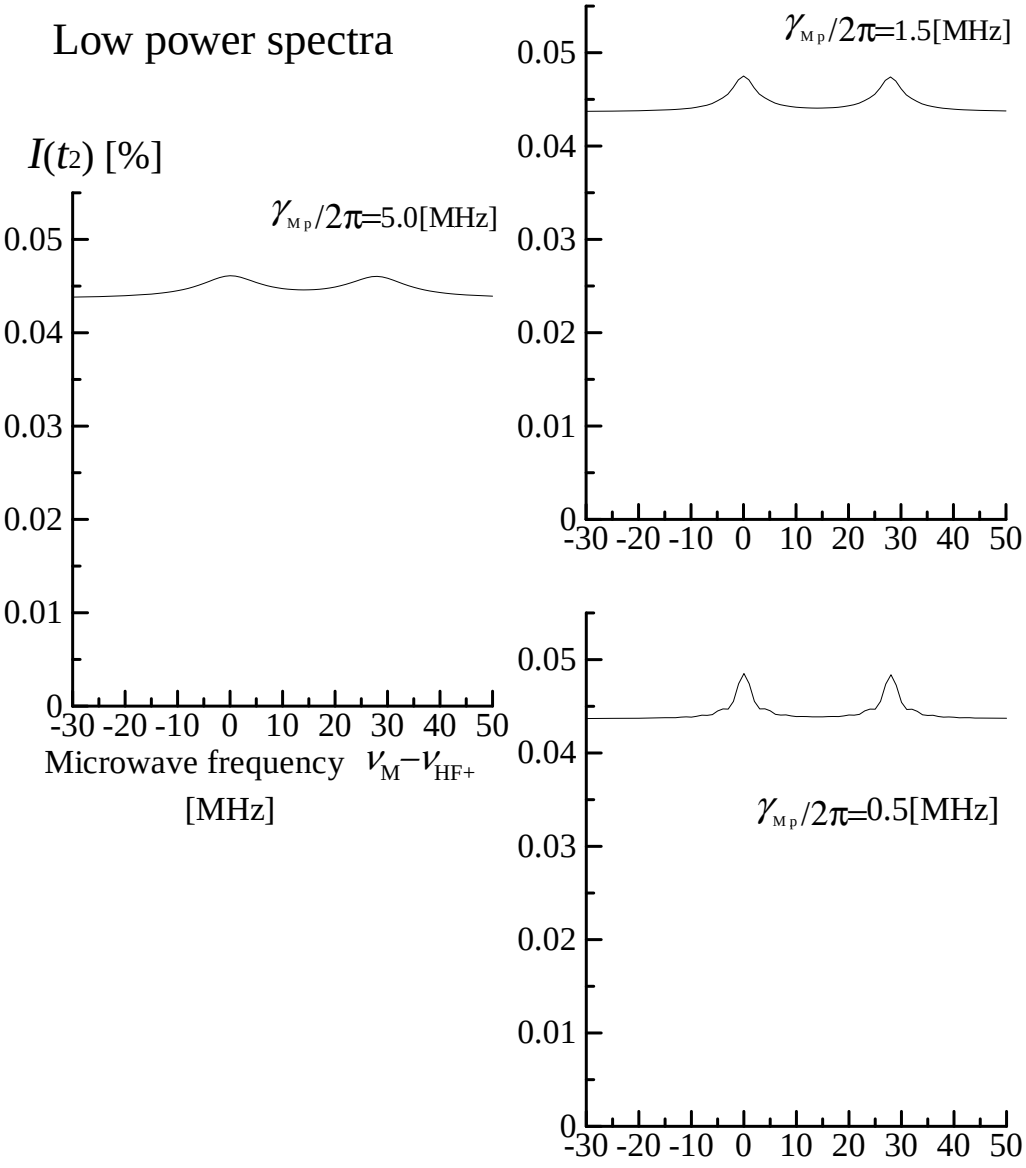

Figure 4.17: The microwave transition spectra at lower microwave power of 1.5W, or $B_0 \sim 1.6$gauss, for some supposed values of the collisional width γ_{Mp}. The induced annihilation increases slightly at the microwave frequency of ν_{HF_+} and ν_{HF_-}. The annihilation signal $I(t_2)$ is normalized by the total incident $\overline{p}$ number, and the signal gains of the microwave transitions are about $2 \sim 5 \times 10^{-5}$. The FWHM are 15MHz, 6MHz and 3MHz for each γ_{Mp}.

Microwave power P	Field strength B_0[gauss]	Collisional width $\gamma_{\mathrm{Mp}}/2\pi$[MHz]	gain/incident $\overline{p}$	gain/ signal at off-resonance
1.5[W]	1.6	0.5	4.9×10^{-5}	0.11
		1.5	3.8×10^{-5}	0.088
		5.0	2.5×10^{-5}	0.056
1.0[kW]	40	0.5	6.8×10^{-5}	0.16
		1.5	6.8×10^{-5}	0.16
		5.0	6.8×10^{-5}	0.16

Table 4.1: Summary of the microwave resonance gain simulation. Simulations were performed with three values of the collisional width and two microwave powers, one is for the HFS search and another is for the SHFS search.

for the $\mathrm{HF_L}$ transition to cause the population transfer. Therefore it will be quite difficult to observe this transition.

Chapter 5

Discussion and conclusion

As calculated in the **Chapter 4**, the signal of the microwave transition is quite small, and amounts to only $2.5 \sim 7 \times 10^{-5}$ fraction of the incident $\overline{p}$. To observe this small signal we must acquire a large number of $\overline{p}$ from AD. From the latest result of the laser spectroscopy shown in **Figure 3.1**, we can roughly estimate how many AD shots (and time) we need to distinguish the signal from noise.

First let us estimate the noise of the delayed annihilation. The delayed annihilation spectrum in **Figure 3.1** shows that there are large fluctuations on the output voltage of the Cherenkov counter photomultiplier.*) The deviations of the output from the exponential curve followed a distribution as shown in **Figure 5.1**. The number of the accumulated AD shot was 56, and one AD shot contained only 10^5 $\overline{p}$ at the moment due to the bad beam condition. So this noise histogram may be comparable to one "real" AD shot of 10^7 $\overline{p}$. For one real AD shot the noise of the DATS is about one volt, and for N AD shot it will be about $\sqrt{N}$ volt.

To evaluate the signal, we should get a relation between the number of induced $\overline{p}$ annihilation and the spike voltage appeared in the DATS in **Figure 3.1**. The number of the total incident $\overline{p}$ was about 5.6×10^6. Only 40% of the incident $\overline{p}$ would stop in the helium target region, because the $\overline{p}$ beam from AD had a wide

*) They are mainly due to the "direct hit" of the charged particle to the photomultiplier (PMT). The light collection efficiency of the Cherenkov counter depends on the particle incident point. If it is close to the PMT the Cherenkov photons will go into the PMT directly (without reflections) , and the light collection efficiency becomes quite large. Therefore everytime the incident particle passes near the PMT, the output voltage increases excessively and a spurious spike appears. This effect might be improved by arranging the counter geometry.

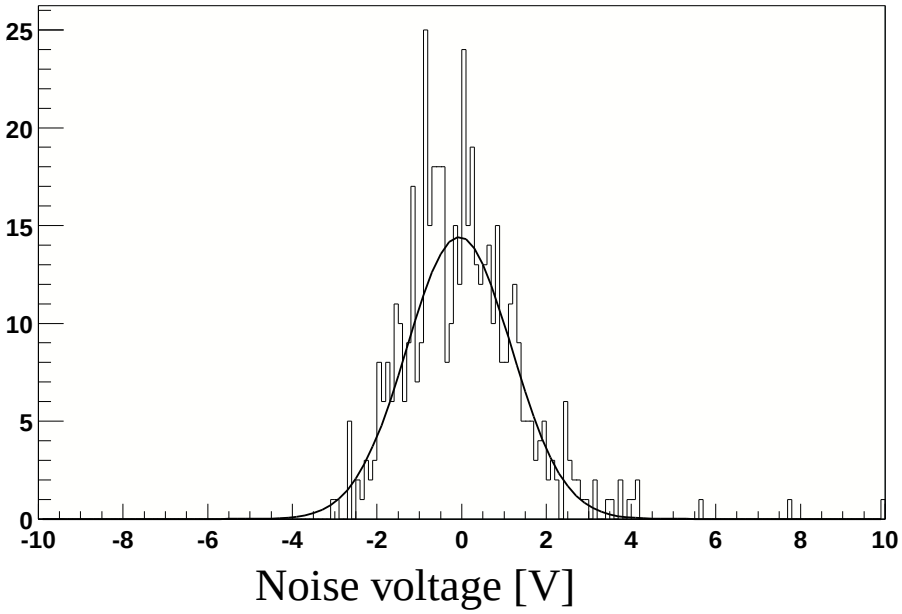

Figure 5.1: Histogram of the noise of the first 2.5μs part of the analog DATS **Figure 3.1** in 5ns bin. The total number of the incident $\overline{p}$ is about 5.6×10^6. The solid curve shows the result of Gaussian fit. The standard deviation of the noise voltage is 1.2V.

vertical width of 30mm[†)][24] while the diameter of the beam entrance window was only 15mm. The $\overline{p}$-He^+ population of the states $(n, l) = (39, 35)$ is about 2×10^{-3}[34] for one incident $\overline{p}$. So the number of the $\overline{p}$-He^+ in $(39, 35)$ level was about 4500. Also we must consider the laser depopulation efficiency of 60% [‡)]. Consequently the number of the $\overline{p}$ annihilations induced by the laser was about 2700. The peak voltage of the induced annihilation spike in **Figure 3.1** was about 13V, so one $\overline{p}$ annihilation has 4.8×10^{-3}V contribution to the DATS. Then we can estimate the microwave transition signal. For one real AD shot the microwave transition induces about $250 \sim 700$ annihilation, which correspond to $1 \sim 3$V signal. For N shots, it will be about N volt.

Concludingly, to get a signal-to-noise ratio better than ten, we may need hundred real AD shots for each microwave frequency. In 2000 we intend to spend 33 days and 4000 shots to the microwave experiment, thus maximum forty microwave frequencies can be searched. To find the resonance we must scan the microwave frequency with a smaller step than the spectrum width. So the HFS search by high power field can

[†)] The horizontal width was 9mm and narrow enough compared to the window diameter.

[‡)] The transition $(39, 35) \rightarrow (38, 34)$ is different from the simulated transition $(37, 35) \rightarrow (38, 34)$ in almost only one sense, that it is a favoured transition and far less laser power is required. So the used laser energy of 2mJ was large enough to cause saturation. From **Figure 4.8** we suppose the saturated efficiency to be 60%.

be done with, say, ten sample frequencies with a 30MHz frequency step within the $\pm$150MHz tuning range. After that the SHFS search will be possible with a finer frequency step of $2 \sim 3$MHz, within a scanning range of $60 \sim 80$MHz around the ν_{HF}. More precise determination of the SHFS will be a future subject.

Thus the conclusion is that we can expect a positive outcome from the AD experiment, provided that the beam has as high intensity and quality as designed. The optimum laser intensity is 2.0mJ/cm^2, and the microwave power can be as large as possible when we search the HFS resonance. The duration of the microwave should be as short as 300ns for example, and the optimum microwave power for SHFS search is determined from this to be 1.5W. From the assigned number of AD shots we will find the hyperfine, and possibly superhyperfine, structures.

Appendix A
Microwave field inside the cavity

A.1 The equation of the electromagnetic field of the cavity

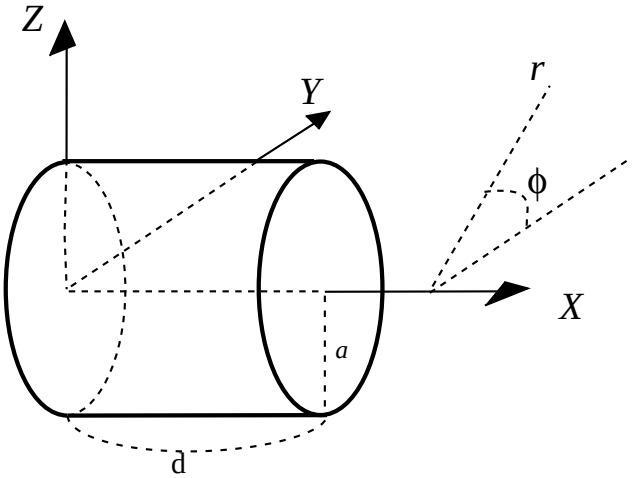

Figure A.1: Definition of the Cartesian and cylindrical coordinates. $r \equiv y^2 + z^2$, and $\phi \equiv \tan^{-1}(z/y)$.

Let us take cylindrical coordinates (r, ϕ, x) as **Figure A.1**. The Maxwell

equations inside the cavity (not including its surface) are

$$\mathrm{div}\boldsymbol{E} = \epsilon_0^{-1}\rho = 0 \tag{A.1}$$

$$\mathrm{rot}\boldsymbol{E} = -\mu_0\frac{\partial \boldsymbol{H}}{\partial t} \tag{A.2}$$

$$\mathrm{div}\boldsymbol{H} = \quad 0 \tag{A.3}$$

$$\mathrm{rot}\boldsymbol{H} = \boldsymbol{j} + \epsilon_0\frac{\partial \boldsymbol{E}}{\partial t} = \epsilon_0\frac{\partial \boldsymbol{E}}{\partial t}. \tag{A.4}$$

Using a familiar vector operator formula

$$\mathrm{rot\ rot} = \mathrm{grad\ div} - \Delta$$

and substituting $\frac{1}{\sqrt{\epsilon_0\mu_0}} = c$, we get $\Delta\boldsymbol{E} = \epsilon_0\mu_0\frac{\partial^2}{\partial t^2} = \frac{1}{c^2}\frac{\partial^2}{\partial t^2}$. The same goes for $\boldsymbol{H}$, so

$$\Delta\boldsymbol{E} - \frac{1}{c^2}\frac{\partial^2 \boldsymbol{E}}{\partial t^2} = 0, \tag{A.5}$$

$$\Delta\boldsymbol{H} - \frac{1}{c^2}\frac{\partial^2 \boldsymbol{H}}{\partial t^2} = 0. \tag{A.6}$$

Now we assume a time dependence factor $e^{i\omega t}$ and change to complex phasor expression.

$$\boldsymbol{E} = \Re(\boldsymbol{e}e^{i\omega t}) \tag{A.7}$$

$$\boldsymbol{H} = \Re(\boldsymbol{h}e^{i\omega t}) \tag{A.8}$$

Here $\boldsymbol{e}$ and $\boldsymbol{h}$ are 3-dimensional complex vector field functions of (r, ϕ, x). Then the equations from (A.1) to (A.6) are reduced to

$$\mathrm{div}\boldsymbol{e} = 0 \tag{A.9}$$

$$\mathrm{rot}\boldsymbol{e} = -i\mu_0\omega\boldsymbol{h} \tag{A.10}$$

$$\mathrm{div}\boldsymbol{h} = 0 \tag{A.11}$$

$$\mathrm{rot}\boldsymbol{h} = i\epsilon_0\omega\boldsymbol{e} \tag{A.12}$$

$$\Delta\boldsymbol{e} + k^2\boldsymbol{e} = 0 \tag{A.13}$$

$$\Delta\boldsymbol{h} + k^2\boldsymbol{h} = 0 \tag{A.14}$$

$$k \equiv \frac{\omega}{c}. \tag{A.15}$$

Next step is to divide the fields into three components.

$$\boldsymbol{e}(r,\phi,x) = e_r(r,\phi,x)\boldsymbol{a}_r(\phi) + e_\phi(r,\phi,x)\boldsymbol{a}_\phi(\phi) + e_x(r,\phi,x)\boldsymbol{a}_x \tag{A.16}$$

$$\boldsymbol{h}(r,\phi,x) = h_r(r,\phi,x)\boldsymbol{a}_r(\phi) + h_\phi(r,\phi,x)\boldsymbol{a}_\phi(\phi) + h_x(r,\phi,x)\boldsymbol{a}_x \tag{A.17}$$

Here $\boldsymbol{a}_r$,$\boldsymbol{a}_\phi$ and $\boldsymbol{a}_x$ mean a unit vector to each direction. Laplacian in cylindrical coordinates is expressed as

$$\Delta = \frac{\partial^2}{\partial r^2} + \frac{1}{r}\frac{\partial}{\partial r} + \frac{1}{r^2}\frac{\partial^2}{\partial \phi^2} + \frac{\partial^2}{\partial x^2}, \tag{A.18}$$

so, we get from (A.13), (A.16) and (A.18) following equation on e_x:

$$\frac{\partial^2 e_x}{\partial r^2} + \frac{1}{r}\frac{\partial e_x}{\partial r} + \frac{1}{r^2}\frac{\partial^2 e_x}{\partial \phi^2} + \frac{\partial^2 e_x}{\partial x^2} + k^2 e_x = 0 \tag{A.19}$$

From (A.19) it is easily found that variable x is separable. That means we can separate the x dependent factor from e_x as

$$e_x = T(r,\phi)X(x) \tag{A.20}$$

$$\frac{1}{X}\frac{d^2X}{dx^2} + k_x^2 = 0 \tag{A.21}$$

$$\frac{d^2T}{dr^2} + \frac{1}{r}\frac{dT}{dr} + \frac{1}{r^2}\frac{d^2T}{d\phi^2} + n^2 T = 0 \tag{A.22}$$

$$k^2 - k_x^2 = k_{\mathrm{T}}^2. \tag{A.23}$$

Again (A.22) asserts that variable ϕ is separable. So,

$$e_x = R(r)\Phi(\phi)X(x) \tag{A.24}$$

$$\frac{d^2X}{dx^2} + k_x^2 X = 0 \tag{A.25}$$

$$\frac{d^2\Phi}{d\phi^2} + n^2\Phi = 0 \tag{A.26}$$

$$r^2\frac{d^2R}{dr^2} + r\frac{dR}{dr} + (k_{\mathrm{T}}^2 r^2 - n^2)R = 0 \tag{A.27}$$

$$k^2 - k_x^2 = k_{\mathrm{T}}^2. \tag{A.28}$$

These equations determine the field e_x, with characteristic values of (k_x, k_{T}, n) depending on the boundary conditions. Though the same equations hold true for h_x, generally they cannot coexist at the same frequency, because h_x is subject to different boundary conditions from e_x and requires different eigenvalues. So now we assume $h_x = 0$. This kind of field mode is classed as TM mode. If we assume $e_x = 0$ instead, it is called TE mode.

A.2 Boundary constraint and resonance frequencies

Here we assume that the cavity wall is a perfect conductor and has infinite electric conductivity σ. As concerns calculation of resonance frequencies it is not critical. Later on the energy loss and Q factor will be given as a perturbational effect about $1/\sigma$.

Then from the boundary conditions of the field following are required:

$$e_\phi = 0,\ e_x = 0\ \ h_r = 0\ \ (\text{at } r = a) \tag{A.29}$$

$$e_\phi = 0,\ e_r = 0\ \ h_x = 0\ \ (\text{at } x = 0) \tag{A.30}$$

$$e_\phi = 0,\ e_r = 0\ \ h_x = 0\ \ (\text{at } x = d) \tag{A.31}$$

With (A.9), (A.30) and (A.31) we can deduce

$$\frac{\partial e_x}{\partial x} = 0 \quad (\text{at } x = 0) \tag{A.32}$$

$$\frac{\partial e_x}{\partial x} = 0 \quad (\text{at } x = d). \tag{A.33}$$

Also the fields should be single valued functions. (i.e. $\boldsymbol{e}(\phi) = \boldsymbol{e}(\phi + 2\pi)$.) Under such conditions, differential equation (A.26) has integer n as eigenvalues and the solutions are

$$\Phi(\phi) = C_1 \exp(in\phi) + C_2 \exp(-in\phi), \qquad n = 0, 1, 2 \cdots \tag{A.34}$$

and the feasible solutions of the Bessel equation (A.27) are first*) kind Bessel functions

$$R(r) = C_0 J_n(k_{\mathrm{T}} r) \tag{A.35}$$

and the boundary condition (A.29) makes allowable k_{T} discrete, as

$$k_{\mathrm{T}} = \frac{\mathrm{P}_{nm}}{a}, \qquad m = 1, 2, 3 \cdots \tag{A.36}$$

where P_{nm} means m-th zero of the function $J_n(x)$. The solutions of (A.25) are also trigonometric functions, and with (A.32) and (A.33),

$$X(x) = C_3 \cos(k_x x), \qquad k_x = \frac{l\pi}{d},\ l = 0, 1, 2 \cdots \tag{A.37}$$

is required. Therefore the final result of resonance frequencies $f(= \frac{\omega}{2\pi} = \frac{c}{2\pi}k)$ is given by

$$f_{nml} = \frac{c}{2\pi}\sqrt{\left(\frac{P_{nm}}{a}\right)^2 + \left(\frac{l\pi}{d}\right)^2}. \tag{A.38}$$

For the specified dimensions $a = 14.15$mm and $d = 24.6$mm (A.38) gives characteristic resonant frequencies as **Table A.1**.

We can derivate the resonance frequencies for TE mode in almost the same way. There are two remarkable distinctions. One is that p_{nm} in the formula should be replaced by p'_{nm} which is m-th root of an equation $\frac{\partial J_n}{\partial x}(x) = 0$. Another is that modes such as $l = 0$ is not allowed because they mean no field at all. A frequency table for TE modes is also shown in **Table A.2**.

It is found that in the frequency range of our interest around 12.9GHz only TM_{110} mode exists. So after now we will focus only on this mode.

*)The second kind of Bessel functions (or Neumann functions) go infinite at $r = 0$, so they are not allowed physically (or in other words have null amplitudes in finite total energy).

Table A.1: Resonance frequencies of TM_{nml} modes for a cylindrical cavity, calculated for specified dimensions of $a = 14.15$mm and $d = 24.6$mm.

TM_{nml}			
n	m	l	$f/$ [GHz]
0	1	0	8.10
0	1	1	10.1
0	1	2	14.6
0	2	0	18.6
1	1	0	12.9
1	1	1	14.3
1	2	0	23.6
2	1	0	17.3

TE_{nml}			
n	m	l	$f/$ [GHz]
0	1	1	14.3
1	1	1	8.69
1	1	2	13.7
1	2	1	18.0
2	1	1	12.0
2	1	2	15.9
2	2	1	23.4

Table A.2: Resonance frequencies for TE_{nml} modes

A.3 Electric and magnetic field of TM_{110} mode and field energy

The aim of this section is to calculate electromagnetic field of TM_{110} mode and draw information on the field energy. From the former argument we can deduce the field expression about e_x.

$$e_x(r,\phi,x) = e_0 J_1(kr)\cos(\phi-\phi_0), \qquad k = \frac{\omega_{110}}{c} = \frac{\mathrm{P}_{11}}{a} \tag{A.39}$$

Clearly that means $\frac{\partial e_x}{\partial x} = 0$, and since $h_x = 0$, there is no source term for e_r and e_ϕ. Thus $e_r = e_\phi = 0$. The field equations are greatly simplified as

$$\begin{aligned}\boldsymbol{h} &= \frac{i}{\mu_0\omega_{110}}\mathrm{rot}(e_x\boldsymbol{a}_x) = \frac{i}{\mu_0\omega_{110}}\left(\boldsymbol{a}_r(\frac{1}{r}\frac{\partial e_x}{\partial\phi}) - \boldsymbol{a}_\phi(\frac{\partial e_x}{\partial r})\right)\\ &= -\frac{i}{\mu_0\omega_{110}}e_0\frac{J_1(kr)}{r}\sin(\phi-\phi_0)\boldsymbol{a}_r - \frac{i}{\mu_0\omega_{110}}e_0\frac{\partial J_1(kr)}{\partial r}\cos(\phi-\phi_0)\boldsymbol{a}_\phi.\end{aligned} \tag{A.40}$$

We can use admittance of vacuum $Y_0 \equiv \sqrt{\frac{\epsilon_0}{\mu_0}}$ and then

$$e_x = e_0 J_1(kr)\cos(\phi-\phi_0) \tag{A.41}$$

$$h_r = -iY_0 e_0\frac{J_1(kr)}{kr}\sin(\phi-\phi_0) \tag{A.42}$$

$$h_\phi = -iY_0 e_0 J_1'(kr)\cos(\phi-\phi_0) \tag{A.43}$$

are the resonated fields in the cavity. If we return to normal expression instead of phasor expression, they will be

$$E_x = E_0 J_1(kr)\cos(\phi - \phi_0)\cos(\omega_{110}(t - t_0)) \tag{A.44}$$

$$H_r = Y_0 E_0 \frac{J_1(kr)}{kr}\sin(\phi - \phi_0)\sin(\omega_{110}(t - t_0)) \tag{A.45}$$

$$H_\phi = Y_0 E_0 J_1'(kr)\cos(\phi - \phi_0)\sin(\omega_{110}(t - t_0)). \tag{A.46}$$

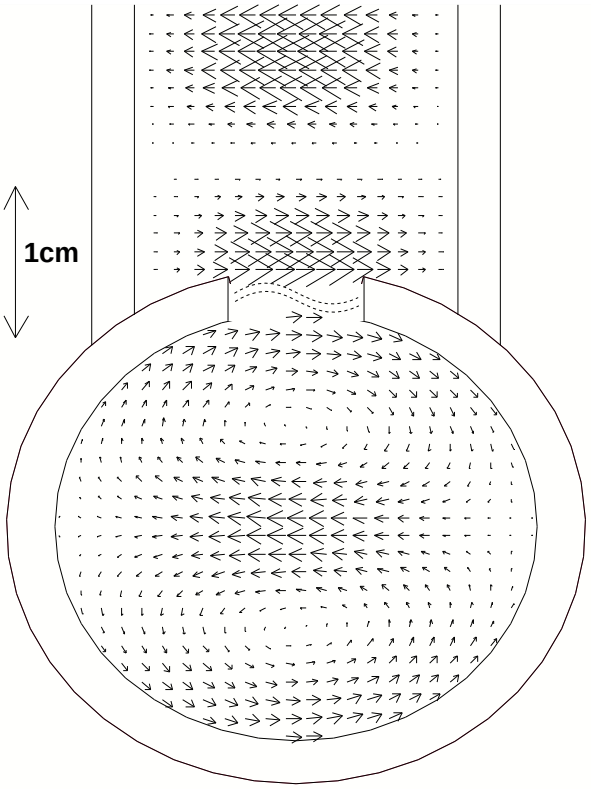

Figure A.2: The magnetic field of TM_{110} mode for our cavity. The arrows indicate the field vector at each point. The electric field is oriented to x direction, perpendicular to this section. The constant ϕ_0 is chosen to $\frac{\pi}{2}$ to couple with the travelling wave in the waveguide. The coupling factor is not taken into account.

Since Bessel function $J_n(kr)$ has a polynomial expansion of

$$J_n(kr) = \sum_{m=0}^{\infty} \frac{(-1)^m (kr/2)^{n+2m}}{m!(n+m)!}, \tag{A.47}$$

the fields around the centre of the cavity are approximately given by

$$E_x = \frac{1}{2} E_0 kr\cos(\phi - \phi_0)\cos(\omega_{110}(t - t_0)) \tag{A.48}$$

$$H_r = \frac{1}{2} Y_0 E_0 \sin(\phi - \phi_0)\sin(\omega_{110}(t - t_0)) \tag{A.49}$$

$$H_\phi = \frac{1}{2} Y_0 E_0 \cos(\phi - \phi_0)\sin(\omega_{110}(t - t_0)) \tag{A.50}$$

and so $H = \frac{1}{2} Y_0 E_0 \sin(\omega_{110}(t-t_0))$. †) Now we are able to calculate total field energy inside the cavity.

$$\begin{aligned} E_{\mathrm{E}} &= \frac{1}{2}\epsilon_0 \int_0^a dr \int_0^{2\pi} r d\phi \int_0^d dx \; E_x^2 \\ &= \frac{\epsilon_0 \pi d E_0^2}{2} \cos^2(\omega_{110}(t-t_0)) \int_0^a J_1^2(kr) r \; dr \\ &= \frac{\epsilon_0 \pi d E_0^2}{2} \cos^2(\omega_{110}(t-t_0)) \frac{1}{k^2} \left[\frac{R^2}{2} J_1'^2(R) + \frac{1}{2}\left(R^2-1\right) J_1^2(R) \right]_0^{R=ka} \\ &= \frac{1}{4}\epsilon_0 \pi a^2 d E_0^2 J_1'^2(\mathrm{P}_{11}) \cos^2(\omega_{110}(t-t_0)) \end{aligned} \tag{A.51}$$

$$\begin{aligned} E_{\mathrm{M}} &= \frac{1}{2}\mu_0 \int_0^a dr \int_0^{2\pi} r d\phi \int_0^d dx \; (H_r^2 + H_\phi^2) \\ &= \frac{\epsilon_0 \pi d E_0^2}{2} \sin^2(\omega_{110}(t-t_0)) \int_0^a \left\{ \left(\frac{J_1(kr)}{kr} \right)^2 + J_1'^2(kr) \right\} r \; dr \\ &= \frac{\epsilon_0 \pi d E_0^2}{2} \sin^2(\omega_{110}(t-t_0)) \frac{1}{k^2} \left[\frac{R^2}{2} J_1'^2(R) + \left(\frac{1}{2}R^2 - 1 \right) J_1^2(R) \right]_0^{R=ka} \\ &= \frac{1}{4}\epsilon_0 \pi a^2 d E_0^2 J_1'^2(\mathrm{P}_{11}) \sin^2(\omega_{110}(t-t_0)) \end{aligned} \tag{A.52}$$

$$E_{\mathrm{total}} = \frac{1}{4}\pi a^2 d J_1'^2(\mathrm{P}_{11}) \epsilon_0 E_0^2 = \frac{1}{4}\pi a^2 d J_1'^2(\mathrm{P}_{11}) \mu_0 (Y_0 E_0)^2 \tag{A.53}$$

So the amplitude of the magnetic field around the center is given by

$$H_0 = \frac{1}{2} Y_0 E_0 = \sqrt{\frac{E_{\mathrm{total}}}{\pi \mu_0 a^2 d J_1'^2(\mathrm{P}_{11})}}. \tag{A.54}$$

A.4 Calculation of energy loss and Q value

From this section we take the finite conductivity of the cavity wall and loss effect into account. The only field nearby the cavity side wall is H_ϕ.

$$H_\phi = 2 H_0 J_1'(\mathrm{P}_{11}) \cos\phi \sin(\omega t) \tag{A.55}$$

From the boundary condition of magnetic field, we get the current going around the wall.

$$J_x(\phi, x) = -H_\phi = -2 H_0 J_1'(\mathrm{P}_{11}) \cos\phi \sin(\omega t) \tag{A.56}$$

†)From (A.45) and (A.46) we can calculate the half maximum radius of the magnetic field. It is $r \sim \frac{2.2}{k}$ for H_r and $r \sim \frac{1.2}{k}$ for H_ϕ.

Here J_x is a surface current density element, already integrated along r direction.

The classical electrodynamics tells us that with finite electric conductivity σ there exists small electric field $E_x = \frac{1}{\sigma\delta}J_x$ in the conductor surface, within the depth of

$$\delta = \sqrt{\frac{2}{\omega\mu\sigma}}. \tag{A.57}$$

The frequency 12.9GHz gives $\delta \sim 3.8\mu$m[‡]. The surface current is not confined on the very surface but ranges from $r = a$ to $r \sim a + \delta$, thus conductor surface element has resistivity element

$$R_{\rm m} = \frac{1}{\sigma\delta} = \frac{1}{2}\omega\mu\delta \tag{A.58}$$

and gives rise to Joule heat $R_{\rm m}J_x^2$[§].

Therefore the (time-averaged) total heat loss from the side wall is

$$\begin{aligned} P_{\rm loss} &= \overline{\int_0^d dx \int_0^{2\pi} ad\phi R_{\rm m} J_x^2} \\ &= \frac{1}{2}\int_0^d dx \int_0^{2\pi} ad\phi \; R_{\rm m} 4H_0^2 J_1'^2(\mathrm{P}_{11})\cos^2\phi \\ &= 2ad\pi R_{\rm m} H_0^2 J_1'^2(\mathrm{P}_{11}) \\ &= \omega\mu\delta ad\pi H_0^2 J_1'^2(\mathrm{P}_{11}) \\ &= \frac{\mu}{\mu_0}\frac{\delta}{a}\omega E_{\rm total}. \end{aligned} \tag{A.59}$$

Usually we assume $\mu = \mu_0$, so

$$Q \equiv \frac{\omega E_{\rm total}}{P_{\rm loss}} = \frac{a}{\delta} \tag{A.60}$$

determines the quality of the cavity[¶]. With high Q, the cavity has a small loss, high excitability, and fine wavelength selectivity. In the calculation above we ignored the loss from front and back walls. If they are closed by conductor as the side wall the same way of loss calculation is applicable and the resultant Q is modified to

$$Q = \frac{a}{\delta}\frac{d}{a+d}. \tag{A.61}$$

In the actual case they are made of meshed structures and supposed to allow more energy leak than closed structures. So result of these formulae must be interpreted only as an upper limit of Q. Surveyed value of the unloaded Q of our cavity was 2700, which is in the same order of theoretical value of $2400 \sim 3800$.

[‡] The conductivity σ of the stainless steel L304 is $1.4 \times 10^6 \Omega^{-1}$m at room temperature.

[§] There is also an imaginary part in the surface resistance, and that causes a $\frac{1}{2Q}$ frequency shift. It is not so significant.

[¶] What determine Q are the geometry and the field pattern of the mode, thus not so sensitive to the frequency

A.5 Excitation of the cavity from outside

Though a perfectly isolated cavity may be ideal in terms of mathematics, it is of no practical use. Cavities we use have external excitation source somewhere. For our case it is regarded as a magnetic dipole at the window to the waveguide, oscillating parallel to the y axis. Suppose a magnetic dipole of a form $\boldsymbol{M}(x,y,z)e^{i\omega t}$ exists around $(r\sim a, \phi\sim\frac{\pi}{2}, x\sim\frac{d}{2})$. If $\omega\sim\omega_{110}$ the microwave field in the cavity is expressed in view of (A.41)$\sim$(A.43) as

$$\boldsymbol{e}\approx e_0\boldsymbol{e}_{110}(r,\phi,x),\qquad \boldsymbol{e}_{110}=\boldsymbol{a}_x J_1(k_{110}r)\sin(\phi) \tag{A.62}$$

$$\boldsymbol{h}\approx h_0\boldsymbol{h}_{110}(r,\phi,x),\qquad \boldsymbol{h}_{110}=\boldsymbol{a}_r\frac{J_1(k_{110}r)}{k_{110}r}\cos(\phi)-\boldsymbol{a}_\phi J_1'(k_{110}r)\sin(\phi). \tag{A.63}$$

Here they are normalized as $\int e_{110}^2dV=\int h_{110}^2dV=I=\frac{1}{2}\pi a^2dJ_1'^2(\mathrm{P}_{11})$. What we must know is a relation between h_0 and $\boldsymbol{M}$. Since $\boldsymbol{B}=\mu_0(\boldsymbol{H}+\boldsymbol{M})$ the maxwell equation (A.10) is modified to

$$\mathrm{rot}\boldsymbol{e}=-i\mu_0\omega\boldsymbol{h}-i\mu_0\omega\boldsymbol{M} \tag{A.64}$$

$$\mathrm{rot}\boldsymbol{h}=i\epsilon_0\omega\boldsymbol{e}. \tag{A.65}$$

From formulae of vector analysis, we get

$$\int(\mathrm{rot}\boldsymbol{e})\cdot\boldsymbol{h}_{110}dV-\int(\mathrm{rot}\boldsymbol{h}_{110})\cdot\boldsymbol{e}dV=\int\mathrm{div}(\boldsymbol{e}\times\boldsymbol{h}_{110})dV$$
$$=\oint(\boldsymbol{e}\times\boldsymbol{h}_{110})\cdot\boldsymbol{n}dS=\oint(\boldsymbol{n}\times\boldsymbol{e})\cdot\boldsymbol{h}_{110}dS \tag{A.66}$$

and considering $\boldsymbol{n}\times\boldsymbol{e}=\boldsymbol{n}\times R_\mathrm{m}\boldsymbol{J}=R_\mathrm{m}\boldsymbol{h}$ at the surface, we get

$$\int(-i\mu_0\omega\boldsymbol{h}-i\mu_0\omega\boldsymbol{M})\cdot\boldsymbol{h}_{110}dV-\int(k_{110}\boldsymbol{e}_{110})\cdot\boldsymbol{e}dV$$
$$=R_\mathrm{m}\oint\boldsymbol{h}\cdot\boldsymbol{h}_{110}dS. \tag{A.67}$$

$$-i\mu_0\omega h_0-i\mu_0\omega\frac{\int\boldsymbol{M}\cdot\boldsymbol{h}_{110}dV}{I}-k_{110}e_0$$
$$=h_0\frac{R_\mathrm{m}\oint h_{110}^2dS}{I}=h_0\mu_0\frac{P_\mathrm{loss}}{E_\mathrm{total}}=\frac{\mu_0\omega}{Q}h_0 \tag{A.68}$$

From (A.65) we get simply $i\epsilon_0\omega e_0=k_{110}h_0$. Now we can solve it as

$$h_0=\frac{\omega^2}{\omega_{110}^2-\omega^2(1-\frac{i}{Q})}\frac{\int\boldsymbol{M}\cdot\boldsymbol{h}_{110}dV}{I}$$
$$\approx-\frac{\omega_{110}}{\omega-\omega_{110}(1+\frac{1}{2Q}i)}\frac{\int\boldsymbol{M}\cdot\boldsymbol{h}_{110}dV}{I} \tag{A.69}$$

This formula describes the characteristic response of the cavity.

Appendix B
Theory of a two-state transition

B.1 Two-state Schrödinger equation and Rabi oscillation.

First we start the argument of E1 transition dynamics with the case of two stable states. Suppose here are two wave functions $\phi_1(r)$ and $\phi_2(r)$ which represent eigenstates of an atom or a molecule.

$$\hat{\mathcal{H}}_0\phi_i(r) = E_i\phi_i(r), \qquad E_1 < E_2 \tag{B.1}$$

Here r denotes the positions of the constituent particles. The functions $\phi_1(r)$ and $\phi_2(r)$ are orthogonal to each other. With these functions any state of the system at time t is expressed by the superposition as

$$\psi(r,t) = c_1(t)\phi_1(r)e^{-i\frac{E_1 t}{\hbar}} + c_2(t)\phi_2(r)e^{-i\frac{E_2 t}{\hbar}}. \tag{B.2}$$

Then we introduce polarized electric field $E_z = E_0(t)\cos(\omega t)$. The amplitude factor $E_0(t)$ changes with time adiabatically. The interaction Hamiltonian is given by

$$\hat{\mathcal{H}}' = -\hat{\mu_z}(r)E_0(t)\cos(\omega t) = -\hat{\mu_z}(r)E_0(t)\frac{e^{i\omega t} + e^{-i\omega t}}{2}. \tag{B.3}$$

Here the electric dipole operator $\hat{\vec{\mu}}(r) \equiv \sum_j e_j\vec{r_j}$ appears. Using the time-dependent Schrödinger equation $i\hbar\frac{d\psi(t)}{dt} = (\hat{\mathcal{H}} + \hat{\mathcal{H}}')\psi(t)$, we get

$$\begin{aligned} &i\hbar\frac{dc_1(t)}{dt}\phi_1(r)e^{-i\frac{E_1 t}{\hbar}} + i\hbar\frac{dc_2(t)}{dt}\phi_2(r)e^{-i\frac{E_2 t}{\hbar}} \\ &= c_1(t)\hat{\mathcal{H}}'\phi_1(r)e^{-i\frac{E_1 t}{\hbar}} + c_2(t)\hat{\mathcal{H}}'\phi_2(r)e^{-i\frac{E_2 t}{\hbar}} \end{aligned} \tag{B.4}$$

Then we operate $\int dr\phi_1^*(r)e^{i\frac{E_1 t}{\hbar}}$. Because $\vec{\mu}$ is a polar vector operator and is an odd function of r, $\int dr\phi_1^*(r)\hat{\mu_z}\phi_1(r)$ should be zero. So we get

$$i\hbar\frac{dc_1(t)}{dt} = c_2(t)\int dr\phi_1^*(r)\hat{H'}\phi_2(r)e^{-i\frac{(E_2-E_1)t}{\hbar}} \tag{B.5}$$

Now we define $\mu_m = \mid \int dr\phi_1^*(r)\hat{\mu_z}\phi_2(r) \mid$ and $\omega_{12} = \frac{E_2-E_1}{\hbar}$, and rewrite the equation.

$$i\hbar\frac{dc_1(t)}{dt} = c_2(t)\mu_m E(t)\frac{e^{i\omega t}+e^{-i\omega t}}{2}e^{-i\omega_{12}t} \tag{B.6}$$

Making a rotational wave approximation and introducing $\Omega(t) \equiv \frac{\mu_m E(t)}{\hbar}$ and $\mathit{\Delta}\omega \equiv \omega - \omega_{12}$, we get

$$\frac{dc_1(t)}{dt} = -ic_2(t)\frac{\Omega(t)}{2}e^{i\omega t} \quad . \tag{B.7}$$

The equation for $\frac{dc_2(t)}{dt}$ is obtained in a similar manner.

$$\frac{dc_2(t)}{dt} = -ic_1(t)\frac{\Omega(t)}{2}e^{-i\omega t} \tag{B.8}$$

These are the equation of the transition in the case of population conserved system. The term Ω is called Rabi frequency. The solution of this equation shows oscillative behaviour. If the field strength is constant far over the period of Ω^{-1}, it is analytically solved and oscillates with a frequency $\sqrt{\Omega^2 + \mathit{\Delta}\omega^2}$.

These are the basic process of E1 transition. Almost in the same way we can obtain the equation for M1 transition. The electric field E_0 is replaced by the magnetic field M_0, and the electric dipole operator $\hat{\mu}$ is replaced by the magnetic dipole operator $\hat{\mu}_{\mathrm{M}}$. Now the diagonal matrix element does not disappear because $\hat{\mu}_{\mathrm{M}}$ is a pseudo vector operator. Nevertheless we can neglect it when the rotational wave approximation holds true, and the results are the same as what we already have.

B.2 Density matrix formulation

While the wave function formulation describes an atom, the density matrix $\hat{\rho} \equiv \sum_{n,m}\phi_n\rho_{nm}\phi_m^*$ represents the statistic property of the whole system. When there is only one atom, or when all the atoms oscillate with perfect correlation and have the same wavefunction $\psi(r,t)$, the density matrix is given by $\rho = \psi\psi^*$, so

$$\rho_{11} \equiv c_1^*(t)c_1(t) \tag{B.9}$$

$$\rho_{22} \equiv c_2^*(t)c_2(t) \tag{B.10}$$

$$\rho_{12} \equiv c_1(t)c_2^*(t)e^{i\omega_{12}t} \tag{B.11}$$

$$\rho_{21} \equiv c_2(t)c_1^*(t)e^{-i\omega_{12}t} = \rho_{12}^* \tag{B.12}$$

The terms ρ_{11} and ρ_{22} can be understood as the populations of the states. The nondiagonal terms express correlations of the atoms, because this term disappears when it is summed over many uncorrelated atoms with arbitrary phases. Modified forms of them are more convenient.

$$\tilde{\rho_{12}} \equiv \rho_{12} e^{-i\omega t} = c_1(t) c_2^*(t) e^{-i\omega t} \tag{B.13}$$

$$\tilde{\rho_{21}} \equiv c_2(t) c_1^*(t) e^{i\omega t} \tag{B.14}$$

The time evolution equations of them can be obtained using the results of the former section.

$$\frac{d\rho_{11}}{dt} = -c_1^*(t) i c_2(t) \frac{\Omega(t)}{2} e^{i\omega t} + c_1(t) i c_2^*(t) \frac{\Omega(t)}{2} e^{-i\omega t} = \frac{1}{2}\Omega(t)(-i\tilde{\rho_{21}} + i\tilde{\rho_{12}}) \tag{B.15}$$

$$\frac{d\rho_{22}}{dt} = -c_2^*(t) i c_1(t) \frac{\Omega(t)}{2} e^{-i\omega t} + c_2(t) i c_1^*(t) \frac{\Omega(t)}{2} e^{i\omega t} = \frac{1}{2}\Omega(t)(i\tilde{\rho_{21}} - i\tilde{\rho_{12}}) \tag{B.16}$$

$$\begin{aligned} \frac{d\tilde{\rho_{12}}}{dt} &= -i c_2(t) \frac{\Omega(t)}{2} e^{i\omega t} \; c_2^*(t) e^{-i\omega t} + i c_1^*(t) \frac{\Omega(t)}{2} e^{i\omega t} \; c_1(t) e^{-i\omega t} - i\boldsymbol{\Delta}\omega\tilde{\rho_{12}} \\ &= -i c_2(t) c_2^*(t) \frac{\Omega(t)}{2} + i c_1^*(t) c_1(t) \frac{\Omega(t)}{2} - i\boldsymbol{\Delta}\omega\tilde{\rho_{12}} \\ &= i\frac{1}{2}\Omega(t)(\rho_{11} - \rho_{22}) - i\boldsymbol{\Delta}\omega\tilde{\rho_{12}} \end{aligned} \tag{B.17}$$

$$\frac{d\tilde{\rho_{21}}}{dt} = -i\frac{1}{2}\Omega(t)(\rho_{11} - \rho_{22}) + i\boldsymbol{\Delta}\omega\tilde{\rho_{21}} \tag{B.18}$$

Then we define $\rho_x \equiv (\tilde{\rho_{12}} + \tilde{\rho_{21}})$ and $\rho_y \equiv i(\tilde{\rho_{12}} - \tilde{\rho_{21}})$.

$$\frac{d\rho_{11}}{dt} = \frac{1}{2}\Omega(t)\rho_y \tag{B.19}$$

$$\frac{d\rho_{22}}{dt} = -\frac{1}{2}\Omega(t)\rho_y \tag{B.20}$$

$$\frac{d\rho_x}{dt} = -\boldsymbol{\Delta}\omega\rho_y \tag{B.21}$$

$$\frac{d\rho_y}{dt} = -\Omega(t)(\rho_{11} - \rho_{22}) + \boldsymbol{\Delta}\omega\rho_x \tag{B.22}$$

These equations of the density matrix are applicable to a single isolated atom. The density matrix of the whole system is an average of that for each atom, but follows a little more complex equations.

B.3 Population losses and relaxation

Then we introduce annihilation (or other) decay processes to the system. The populations ρ_{11} and ρ_{22} should decay exponentially according to decay rates γ_1 and

γ_2 respectively. The amplitudes we wrote as $c_1(t)$ and $c_2(t)$ come to include damping factors $e^{-\frac{\gamma_1}{2}t}$ and $e^{-\frac{\gamma_2}{2}t}$, so the nondiagonal term ρ_{12} also has to decrease with a rate $\gamma_{12} \equiv \frac{1}{2}(\gamma_1 + \gamma_2)$. It is natural because the correlation among all the atoms must diminish as the total population of the atom gets small.

We must somehow include effects of collisions with other atoms. The simplest explanation goes as follows. Suppose some atom approaches to the atom which is in a cycle of the transition. Due to the interatomic interaction (such as van der Waals interaction) there occurs a small instantaneous shift $\delta\omega(t)$ in the transition frequency*), or, $\Delta\omega$. Thus the equation (B.17) for a certain atom is modified as

$$\frac{d\tilde{\rho_{12}}}{dt} = i\frac{1}{2}\Omega(t)(\rho_{11} - \rho_{22}) - (i(\Delta\omega + \delta\omega(t)) + \gamma_{12})\tilde{\rho_{12}} \tag{B.23}$$

After the laser irradiation we get a formal solution of

$$\tilde{\rho_{12}}(t) = \tilde{\rho_{12}}(t_0)\exp(-i\Delta\omega(t-t_0) - \gamma_{12}(t-t_0) - i\int_{t_0}^{t}\delta\omega(t')dt') \tag{B.24}$$

To get the density matrix of the whole system we can use a statistical method.

$$\begin{aligned}
\tilde{\rho_{12}}_{(\mathrm{total})}(t) &= \tilde{\rho_{12}}(t_0)e^{-i\Delta\omega(t-t_0)-\gamma_{12}(t-t_0)}\left\langle \exp(-i\int_{t_0}^{t}\delta\omega(t')dt')\right\rangle \\
&= \cdots(1 - i\int_{t_0}^{t}\langle\delta\omega(t')\rangle dt' - \frac{1}{2}\int_{t_0}^{t}\int_{t_0}^{t}\langle\delta\omega(t')\delta\omega(t'')\rangle dt'dt'' + \cdots) \\
&= \cdots(1 - \gamma_{\mathrm{p}}(t-t_0) + \cdots) \\
&= \cdots\exp(-\gamma_{\mathrm{p}}(t-t_0))
\end{aligned} \tag{B.25}$$

Here we assumed $\langle\delta\omega(t')\delta\omega(t'')\rangle = 2\gamma_{\mathrm{p}}\delta(t'-t'')$, and a new damping rate γ_{p} was introduced. Thus we obtain equations of the total density matrix. Now we omit the subscript $_{(\mathrm{total})}$.

$$\frac{d\tilde{\rho_{12}}}{dt} = i\frac{1}{2}\Omega(t)(\rho_{11} - \rho_{22}) - (i\Delta\omega + \gamma_{\mathrm{p}} + \gamma_{12})\tilde{\rho_{12}} \tag{B.26}$$

The final result is

$$\frac{d}{dt}\begin{pmatrix}\rho_{11}\\ \rho_{22}\\ \tilde{\rho_x}\\ \tilde{\rho_y}\end{pmatrix} = \begin{pmatrix}-\gamma_1 & 0 & 0 & \frac{1}{2}\Omega(t)\\ 0 & -\gamma_2 & 0 & -\frac{1}{2}\Omega(t)\\ 0 & 0 & -\gamma_T & -\Delta\omega\\ -\Omega(t) & \Omega(t) & \Delta\omega & -\gamma_T\end{pmatrix}\begin{pmatrix}\rho_{11}\\ \rho_{22}\\ \tilde{\rho_x}\\ \tilde{\rho_y}\end{pmatrix} \tag{B.27}$$

where $\gamma_{\mathrm{T}} \equiv \gamma_{\mathrm{p}} + \frac{1}{2}(\gamma_1 + \gamma_2)$ is the total transverse relaxation rate.

*)This kind of collision which only disturbs the oscillation without energy transfer is called an optical collision. When the perturber comes close to the atom some transition of the atomic state may occur. This is called an inelastic collision, but is not so significant.

Acknowledgments

I would like to express my greatest thanks to my supervisor Prof. Dr. R.S. Hayano, who gave me the chance to work in this interesting field, and helped me with many pieces of invaluable advice and patient back-up. I could not help be struck with his intelligence, accomplishment, vitality, generousness and sense of physics.

I am also much obliged to Dr. T. Ishikawa and Dr.E. Widmann. They are the best advisers and teachers, and I have been trained from them a lot. Had it not been for the detailed advice of these three this thesis would not be accomplished.

I would also like to pay my respect to Dr. J. Eades and Dr. T. Yamazaki, for their great accomplishments and contributions to the ASACUSA project. I am proud of their graces.

I am quite delighted with having been acquainted with many competent colleagues. I owe many to Dr. H.A. Torii on the understanding of the laser calculation and the collision theory. Professional work of Mr. M. Hori always lead our experiments to successes. Also there was a contribution of Mr. K. Yamashita to the Cherenkov counter tests. Mr. H. Yamaguchi demonstrated his ability of computer manipulation a lot. Mr. B. Juhasz undertook many work about cryogenics and so on. Mr. K. Suzuki and Dr. H. Gilg also helped us in the meantime of their own work. I thank to all of them with the best appreciation. Thanks are also due to Dr. M.C. Fujiwara, Dr. H. Higaki and Mr. R. Funakoshi, the colleagues who are engaged in the ATHENA experiment. During the stay in CERN we would often encouraged each other. I also express my gratitude to my fellows, Mr. S. Sakoda and Mr. N. Imai, for their kindness, practical advice and encouragements.

I am also in a debt to Dr. K. Tanida for some advice on the discussion chapter.

I wish to express my sincere thanks to the whole member of the ASACUSA collaboration, my parents and friends, people in CERN, Dr. Miura and other workers in Nihon Koshuha, and other acquaintances.

Bibliography

[1] O. Chamberlain *et al.,* Phys. Rev. 100 (1955) 947.

[2] C.S. Wu *et al.,* Phys. Rev. 105 (1957) 1413.

[3] J.H. Christenson *et al.,* Phys. Rev. Lett. 13 (1964) 138.

[4] M. Iwasaki *et al.,* Phys. Rev. Lett. 67 (1991) 1246.

[5] S.N. Nakamura *et al.,* Phys. Rev. A 49 (1994) 4457.

[6] T. Yamazaki *et al.,* Nature 361 (1993) 238.

[7] E. Widmann *et al.,* Phys. Rev. A 51 (1995) 2870.

[8] B. Ketzer *et al.,* Phys.Rev. A 53 (1996) 2108.

[9] E. Widmann *et al.,* Phys. Rev. A 53 (1996) 3129.

[10] N. Morita *et al.,* Phys. Rev. Lett. 72 (1994) 1180.

[11] R.S. Hayano *et al.,* Phys. Rev. Lett. 73 (1994) 1485; 73(1994) 3181.

[12] F.E. Maas *et al.,* Phys. Rev. A 52 (1995) 4266.

[13] H.A. Torii *et al.,* Phys. Rev. A 53 (1996) R1931.

[14] R.S. Hayano *et al.,* Phys. Rev. A 55 (1997) 1.

[15] T. Yamazaki *et al.,* Phys. Rev. A 55 (1997) R3295.

[16] E. Widmann *et al.,* Phys. Lett. B 404 (1997) 15.

[17] T. Yamazaki *et al.,* Chem. Phys. Lett. 265 (1997) 137.

[18] B. Ketzer *et al.,* Phys. Rev. Lett. 78 (1997) 1671.

[19] B. Ketzer *et al.,* Chem. Phys. 109 (1998) 424.

[20] H.A. Torii *et al.,* Phys. Rev. A 59 (1999) 223; H.A. Torii, Doctor thesis, Dept. of Physics, Graduate School of Science, University of Tokyo, (1998).

[21] M. Hori *et al.,* Phys. Rev. A 57 (1998) 1698.

[22] H.A. Torii *et al.,* Nucl. Instrum. Methods. A 396 (1997) 257.

[23] T. Azuma *et al.,* (ASACUSA Collaboration), Proposal CERN/SPSC 97-19, CERN/SPSC P-307 (1997).

[24] T. Azuma *et al.,* (ASACUSA Collaboration), Progress report CERN/SPSC 2000-04, CERN/SPSC M642 (1999).

[25] S. Maury *et al.,* Design study of the Antiproton Decelerator, presented on the world wide web (1997).

[26] A. Kreissl *et al.,* Z. Phys. C 37 (1988) 557.

[27] G. Gabrielse *et al.,* Phys. Rev. Lett. 82 (1999) 3198.

[28] Particle data group, Review of Particle Physics, The European Physical Journal C 1998.

[29] T. Yamazaki and K. Ohtsuki, Phys. Rev. A 45 (1992) 7782.

[30] T. Yamazaki and K. Ohtsuki, Phys. Rev. A 50 (1994) 5350.

[31] I. Shimamura, Phys. Rev. A 46 (1992) 3776, and private communication (1993).

[32] K. Ohtsuki, private communication (1993).

[33] N. Morita *et al.,* Nucl. Instrum. Methods A 330 (1993) 439.

[34] M. Hori, Doctor thesis, Dept. of Physics, Graduate School of Science, University of Tokyo, (2000).

[35] V.I. Korobov, private communication (1999).

[36] D.D. Bakalov *et al.,* Phys. Lett. A 211 (1996) 223.

[37] V.I. Korobov, Phys. Rev. A 54 (1996) R1749.

[38] V.I. Korobov, D.D. Bakalov, Phys. Rev. Lett. 79 (1997) 3379.

[39] V.I. Korobov, D.D. Bakalov, Phys. Rev. A 57 (1998) 1662.

[40] N. Elander and E. Yarevsky, Phys. Rev. A 56 (1997) 1855, Errata Phys. Rev. A 57 (1998) 2256.

[41] Y. Kino, M. Kamimura, H. Kudo, Nucl. Phys. A 631 (1998) 649c.

[42] V.I. Korobov, in *Proceedings of the Asia-Pacific Few Body Conference (APFB99)*, Kashiwa, 1999, Few Body Systems Suppl., in press.

[43] G. Ya. Korenman, Density Shift and Broadening of SHFS M1-transitions: Revisited, unpublished (1999).

[44] R.E. Collin *et al.,* Foundations for microwave engineering (second edition), McGraw-Hill, 1992.

Addendum

1 Multiple induced annihilation by laser pulse train

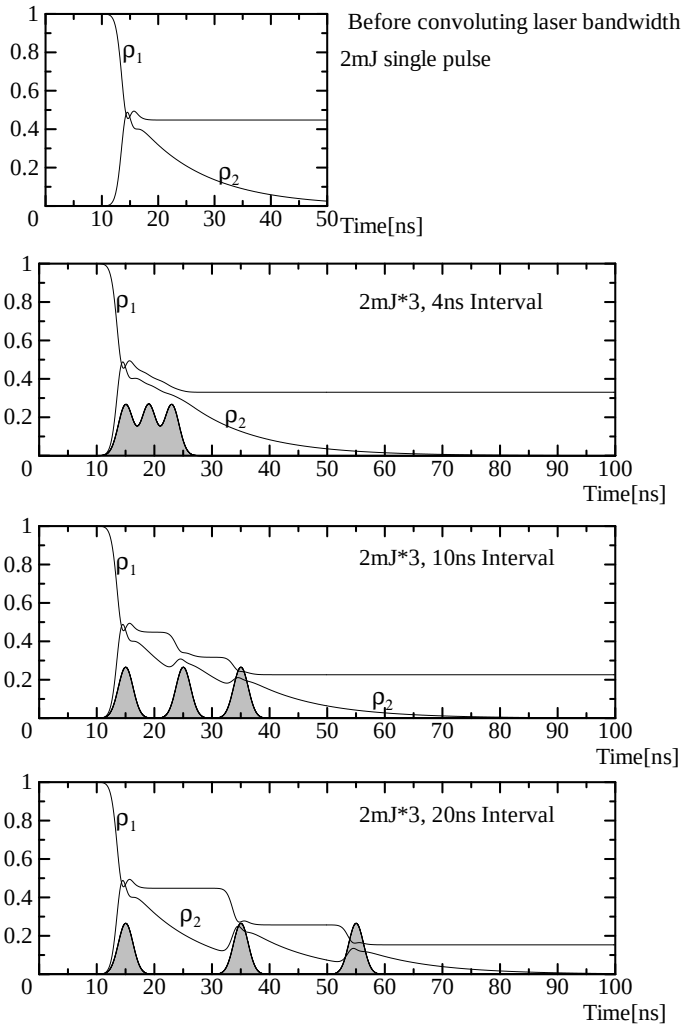

Figure 1:

Fig1 shows the time profiles of the density matrices in three 2mJ-power laser pulse situation. Convolutions for laser bandwidth have not been performed yet. The gray peaks indicates the laser powers (in arbitrary unit). The FWHM of the laser pulses is 3ns. With longer interval we get larger depletion.

Fig2 shows the depletion efficiencies against laser power. Laser bandwidth of 800MHz was included. The optimum laser power per one pulse seems to be 1mJ.

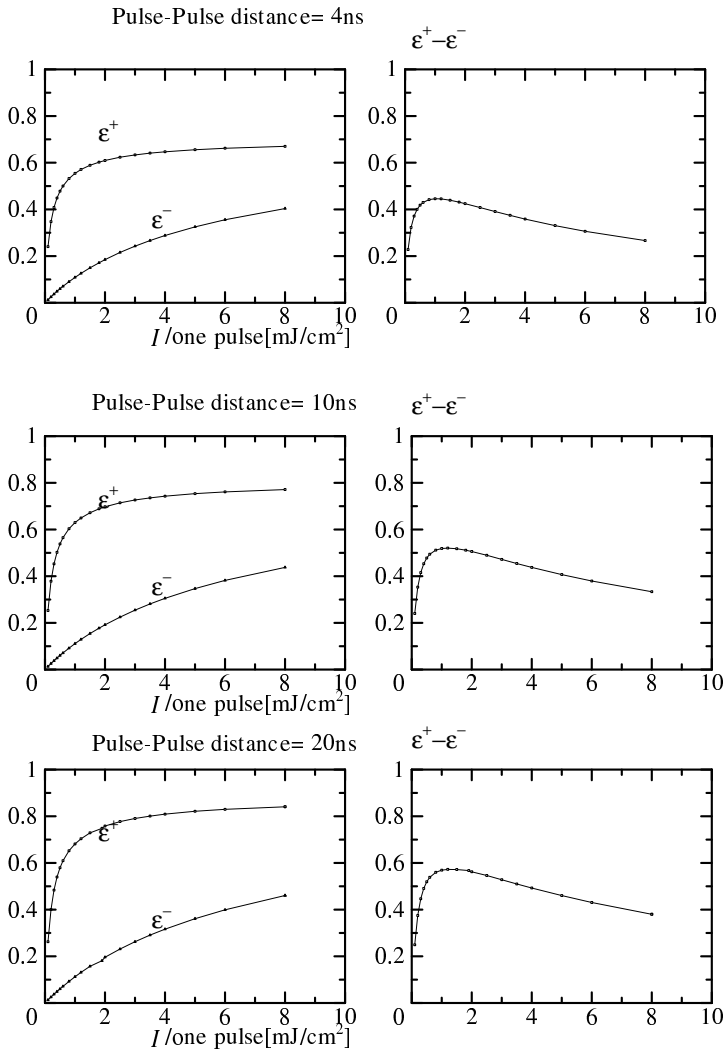
Pulse-Pulse distance= 4ns
ε+–ε−
ε+
ε−
I /one pulse[mJ/cm2]
Pulse-Pulse distance= 10ns
ε+–ε−
ε+
ε−
I /one pulse[mJ/cm2]
Pulse-Pulse distance= 20ns
ε+–ε−
ε+
ε−
I /one pulse[mJ/cm2]

Figure 2:

2 Magnetic field distribution

The microwave field of TM110 mode is not uniform in the y-z plane. Assuming that the stopping pbar has a Gaussian radial distribution of 5mm FWHM around the centre axis, the distribution of the magnetic field for one stopping pbar will be like this.

To be accurate, all the microwave calculation in the thesis should be convoluted by this distribution, and will have wider spectrum widths and lower S/N.

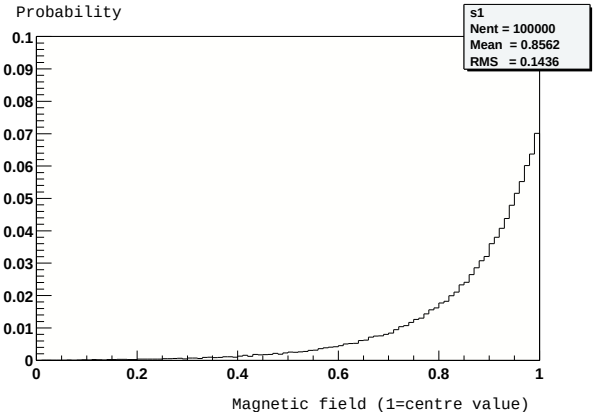

Figure 3:

3 Initial Population

The initial population of the (37,35) used in the calculation was $\sim 3 \times 10^{-}3$, while the recent value calclated by Hori in his Dr.thesis is $\sim 1.5 \times 10^{-}3$. So the annihilation signal may be half of the previous calculation.